Beam Loss Monitor Design Investigations for Particle Accelerators

Michael Hodgson

For and on behalf of,

European Organization for Nuclear Research

A dissertation submitted to the Physics Department at the University of Surrey in partial fulfillment of the degree of Masters in Physics.

Department of Physics
University of Surrey
25 April 2005

Abstract

This report documents a comprehensive investigation into the design considerations for the ionisation chambers that will be used in the LHC beam loss monitoring system. Comparisons were made between the prototype chamber designs (parallel plate, 2-Coaxial and 3-Coaxial chambers) and the proposed filling gases (Ar, Ar(93%)CO_2(7%) and N_2).

Accelerator experiments and *Geant 4* simulations were conducted to determine the chamber's beam impact properties and signal fluctuations. It was found that the parallel plate chambers produced the lowest fluctuations (40% lower than the coaxial for the simulations and 12% lower for experiments).

Further to this a comparison of the total integrated charge within the experimental and simulated chambers, marked a direct method of determining *Geant's* accuracy, which was found to be $\pm$ 35% for a proton beam.

Geant 4 simulations were carried out to establish the chamber's sensitivity to the expected LHC secondary particle showers, and so determine the signal per lost proton. The coaxial chambers were generally found to produce the largest signal per proton, however the parallel plate chamber was found to be more sensitive for low energy particles. This was due to the coaxial chamber's electrodes absorbing the lower energy particles before they could ionise the detector gas.

Accelerator experiments and *Garfield* simulations were conducted to determine the signal response of the chambers and the amount of signal which is collected in 100μs. It was established that the parallel plate chambers had, on average, 3 and 30 times quicker electron and ion signals than the coaxial chambers. All chambers were found to collect over 70% of their signal within 100μs, with the parallel collecting the most, 100%

The investigations also highlighted that the filling gases with the fastest drift velocities would provide the quickest signals, and the gasses with the largest energy deposition rates would provide the most sensitive signals. Measurements and simulations showed that the nitrogen gas produced the quickest signals (with the exception of the argon carbon-dioxide electron signal) and the argon produced the largest signals (1.77 times larger than the nitrogen).

The aging effects of SPS type ionisation chambers were examined by comparative radioactive source measurements. Low radiated ($\approx$ 1 kGy/per year) chambers show a variation in the mean signal (σ) of only 0.5%. Higher radiated

chambers (between 2 to 10 kGy/per year) show $\sigma = 5\%$. Experiments are still being conducted to determine an ageing calibration constant, but preliminary tests show a definite signal degradation in chambers with prolonged exposure to large amounts of radiation.

The cumulative result of these design investigations is the decision that the LHC beam loss monitors will be the nitrogen filled parallel plate chambers. They will be filled to 1.2 ATM.

Acknowledgements

I would like to take this opportunity to thank the people who have helped me with my year at CERN and the production of this dissertation.

Thank you Rebecca Allen, Mathew Veale and Ray Hodgson (my Dad) for revising my rather feeble understanding of the English language and making this document more readable.

I would like to thank James Ridewood and Anastasiya Radeva for being "Bonnet de Douche", and Charly for always being there for me.

I also wish to thank Ewald Effinger, Gianfranco Ferioli, Gianluca Guaglio, Roman Leitner, Laurette Ponce, Helge Refsum, Markus Stockner, R. Veenhof and Christos Zamantzas for helping me with theory, for putting up with my annoying programing questions and for, in some instances, getting irradiated with me.

I wish to extend very special thanks to my supervisors during the year, Bernd Dehning and Eva Barabara Holzer, who gave me the fantastic opportunity to work with these wonderful people. Their guidance was exceptional, their tolerance commendable, their help priceless.

Finally, Professor Tony Clough deserves genuine and wholehearted thanks. Without your patience, help and guidance I would not have come this far, thank you.

Role of Author

During my year at CERN I had the privilege of working within the AB-BDI-BL section (Accelerators & Beams, Beam Development Instrumentation, Beam Loss). For the initial half of the year I was supervised by Dr. Barbara Holzer and for the latter, by section leader Dr. Bernd Dehning. My primary role within the section was the design investigations upon the ionisation chamber beam loss monitors for the forth coming Large Hadron Collider.

These investigation required me to learn the *Garfield* and *Geant 4* computer simulation codes, as well as *Geant's* structure code, *C++*. By doing this I was able to simulate the signal response of ionisation chambers, as well as their expected signal during operation, and the signal produced within the detectors as a function of proton beam impact positions.

Several of these simulations required experimental verification within some of the CERN accelerators. I was actively involved in the preparation, installation and recording of these experiments, giving me knowledge of the operational aspects of these accelerators and how to work in high radioactive areas.

As well as these pre-ordained experiments, I proposed, designed and conducted several other design tests upon the ionisation chambers. These included 'faulty' detector inspection tests, accelerated lifetime tests and experiments into an interesting time-based, zero voltage signal phenomenon, which I had noticed during the preparation of other experiments.

Further to this I was actively involved in the testing and commissioning of both prototype and existing detectors. I was required to conduct low current measurements on the detectors, in both the laboratory and accelerator tunnels, with several forms of readout electronics (including a highly sensitive multi-meter device) and a cesium-137 radioactive source.

During my year I gained an extensive understanding into the the principles and applications of beam loss monitoring. I also gained accelerator physics knowledge, not only from CERN but also USPAS (the United States Particle Accelerator School), which I fortunate enough to be given the opportunity to attend.

The results I obtained, and the knowledge I had gained, for the workings of the detectors was pivotal in the final design decisions for the type of ionisation chambers to be used for the LHC, which were agreed upon in a meeting at the end of my tenure at CERN.

Abbreviations, Constants and Mathematical Notation

CERN	-	le Conseil Européen pour Recherche Nucléaire, or the European Centre for Particle Physics
LHC	-	Large Hadron Collider
SPS	-	Super Proton Synchrotron
PS	-	Proton Synchrotron
PSB	-	Proton Synchrotron Booster
LEP	-	Large Electron-Positron Collider
BLM	-	Beam Loss Monitoring
G4	-	Geant 4

e	=	elementary charge	=	1.60×10^{-19} C
m_e	=	electron mass	=	9.11×10^{-31} kg
c	=	speed of light	=	300×10^{6} ms^{-1}
k	=	Boltzmann constant	=	1.38×10^{-23} J/K
			=	8.62×10^{-5} eV/K
ε_0	=	permittivity of free space	=	8.85×10^{-12} C^{2}N^{-1}m^{-2}
h	=	Plank's constant	=	6.63×10^{-34} Js
N_A	=	Avogadro's constant	=	6.02×10^{23} mol^{-1}
Td	=	Townsends	=	10^{-21} Vm^2
α	=	fine structure constant	=	$e^2/4\pi\varepsilon_0\hbar c$
r_e	=	classical electron radius	=	$e^2/4\pi\varepsilon_0 m_e c$

V	=	Potential difference (V)	E_n	=	Energy
C	=	Capacitance (F)	dE_n/dx	=	Rate of energy loss (MeV cm^{2}g^{-1})
z	=	Charge magnitude	E	=	Electric field strength (Vcm^{-1})
q	=	Charge (C)	B	=	Magnetic field strength
Q	=	Total charge (C)	E_w	=	Charge pair creation energy (eV)
K	=	Ion Mobility (cm^{2}V^{-1}s^{-1})	K_0	=	$N_A e^4/4\pi m_e c^2 \varepsilon_0^2$
v_i	=	Ion drift velocity	I_e	=	Mean excitation energy (eV)
v_e	=	Electron drift velocity	Φ	=	1^{st} ionising potential (eV)
a	=	Acceleration	I	=	Current (intensity in section 3.1.4)
T	=	Absolute temperature (K)	N	=	Number
T_{eff}	=	Effective Temperature (K)	n	=	Number density (cm^{-3})

Contents

Chapter 1

CERN

CERN (le Conseil Européen pour Recherche Nucléaire or the European Centre for Particle Physics) is one of the largest and most influential research institutes in the world. The organization, funded and comprised of twenty countries, has been at the forefront of technical and scientific research for over fifty years. The development and construction of the Large Hadron Collider (or LHC) project, currently promises to carry on this tradition into the foreseeable future.

The LHC will be the latest and largest link in the substantial network of particle accelerators and colliders that currently comprises the CERN facility, as shown in figre 1.1. The Super Proton Synchrotron (SPS), Proton Synchrotron (PS) and the Proton Synchrotron Booster (PSB) are some of the currently operational machines that will be used to feed this new device.

By accelerating and colliding particles at very high, and currently unobtainable, energies the LHC will help in answering some of the most fundamental questions of our time. The theory is that collisions at these higher energies will produce new particles (often called Higg's particles) or processes, which will help in the understanding of such ideas as unified field theory or even the birth of the universe itself.

1.1 The Large Hadron Collider

The LHC promises to be not only the largest and most advanced particle accelerator at CERN, but also in the world. Over 27km of tunnels, at an average of 150m underground, spanning both parts of France and Switzerland will house the device, replacing the old Large Electron-Positron Collider (LEP), an equally important and technologically advanced machine of its time.

The design of the machine is to accelerate and collide, protons and heavy ions (such as lead) at energies of 7 TeV and 574 TeV, respectively, a goal never achieved in an accelerator before. Two concentric rings will contain up to 2835 bunches of 10^{11} particles each, crossing and colliding at experimental areas shown

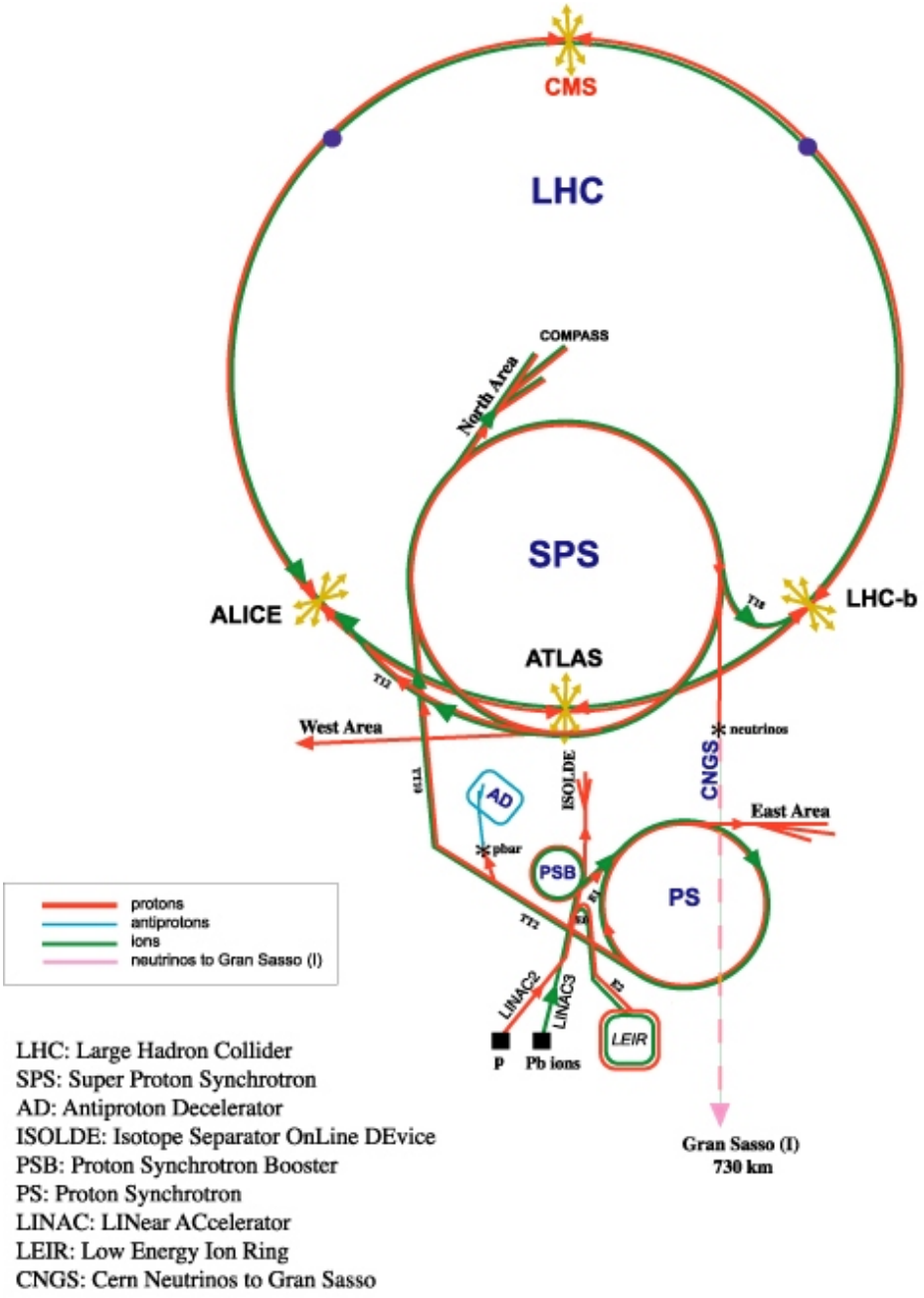

Figure 1.1: *Accelerators at CERN*

in figure 1.2. The particles will be accelerated and contained using advanced super conducting magnets which must be kept at a temperature of around 1.9K, for maximum beam energy. The commissioning of this mammoth machine is currently planned for 2007.

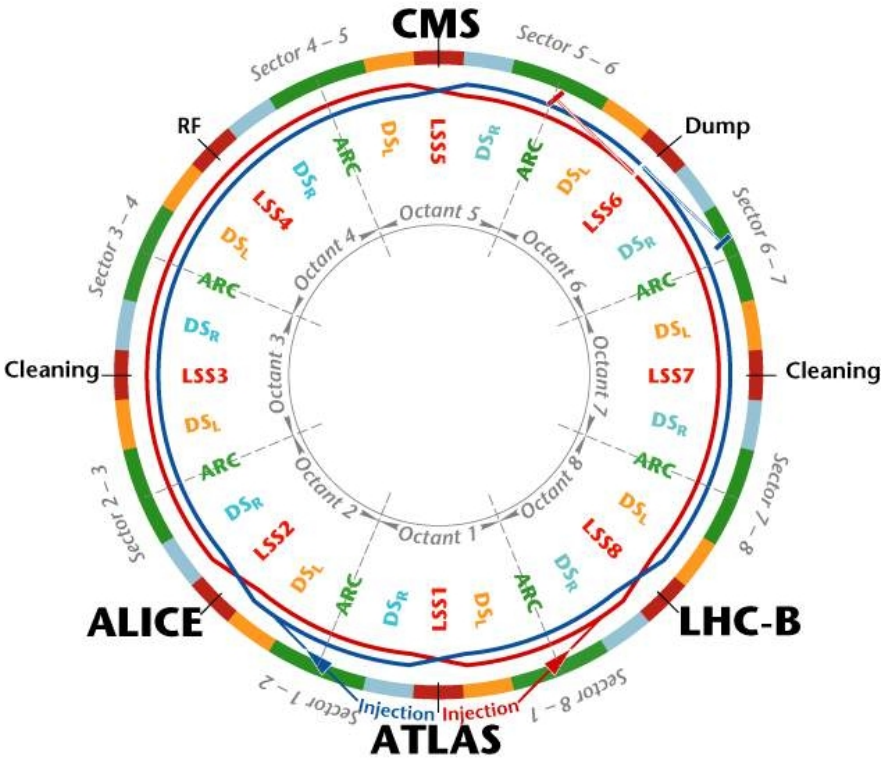

Figure 1.2: *Plan of LHC sections and experimental areas*

1.2 The Super Proton Synchrotron

The SPS is currently the largest operating accelerator at CERN, occupying 7 km of tunnels, again through France and Switzerland. Operational since 1976, the SPS is currently capable of accelerating protons and heavy ions up to 450 GeV. This historically important machine (used in the discovery of W and Z bosons, bringing the first Nobel Prize for Physics to CERN) has it's own experimental areas, but will be primarily used as the main injection accelerator to the LHC.

1.3 The Proton Synchrotron

The PS may be considered almost the backbone of the CERN accelerator complex. Being the oldest machine at CERN (built in 1959), all other accelerators have been built around it. The 200m device is currently capable of accelerating particles up to 29 GeV, for extraction to test facilities and other accelerators.

1.4 The Proton Synchrotron Booster

The PSB is a four ringed accelerator that allows, between 5×10^8 and 1×10^{10} particles to be accelerated from 0.05 GeV to 1.38 GeV. The 160m device allows protons to gain a momentum close to the minimum stopping power of most materials (shown in section 3.1.1) making it useful for matter interaction experiments.

Figure 1.3: *CERN and the LHC*

(a) *Aerial view of CERN and it's surroundings in Geneva. Dotted line is the Swiss-French border.*

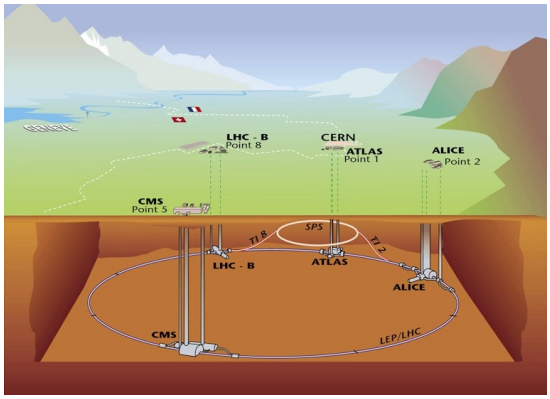

(b) *Underground plan of the LHC & SPS facilities.*

Chapter 2

LHC Protection

The LHC, like all particle accelerators, will be prone to unavoidable losses from the particle beam bunches. Electromagnetic instabilities, caused by beam-beam interactions at collision points and intra-beam scattering (caused by collisions between particles in the bunches), will liberate a small proportion of the particles, causing them to impact with the machine's walls. When these interactions occur, their energy will be converted into heat and showers of secondary energetic particles.

The LHC, however will be a 'delicate' machine, as the superconducting magnets must be kept at a very low temperature in order to operate correctly. If the temperature should increase the magnets will 'quench' and lose their superconducting properties, causing several hours of downtime. A worse case scenario is the possibility that these quenches may also damage the magnet beyond repair, causing a downtime of almost 30 days and costing in the order of £250,000 (for one magnet alone). As yet no relationship is known between the number of quenches a magnet undergoes and the damage caused (it can range from hundreds to just a couple), but it seems likely that the chance of damages occurring increases with each quench.

As would be expected, counter measures will be installed in the LHC to combat losses. Collimators will assist in minimizing the energy deposited in the magnets by concentrating losses to places where they are not harmful. However, quenches may occur from a loss of lots of high-energy particles in a short amount of time or from prolonged exposure to a few high-energy particles (something which the collimators could not protect against).

The relation of the time and magnitude of the losses may be seen within figure 2.1. The quenching levels (represented by the plotted curves) for a proton beam at energies of 450 GeV (at injection) and 7 TeV (the maximum energy) as a function of time, are shown on the graph. The drawn curves represent the dynamic range for the required operational boundaries for the beam loss monitors (BLMs).

The point A represents the stage at which the heat starts to flow from the

cable coil into the surrounding liquid coolant (Helium). A constant flow continues until, at B, the heat capacity of the liquid helium is reached. If the proton loss decreases it will become possible for a constant flow of heat into the cooling system, C.

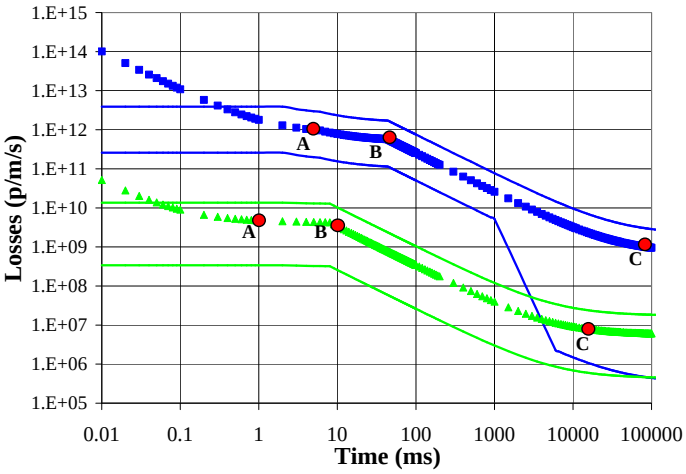

Figure 2.1: *Quench levels of the LHC bending magnets as a function of the loss duration (plotted lines). Defined monitoring range at both 450 GeV and 7 TeV energies (drawn lines).*

A further method of machine protection is beam loss monitoring, in which the loss levels, which depend on both the loss duration and beam energy, are continuously monitored. These are compared against the threshold values, which are derived from the quench levels, shown in figure 2.1. If the loss levels reach a potentially harmful amount the beam may be safely 'dumped' (or discarded) within one revolution of a bunch (100 μs), as called for in the machines specifications [3].

The beam loss monitors used for the task must be effective and reliable, while also being cost effective. Further to this they should remain this way for the entire lifetime of the LHC (approximately twenty years) in order to completely protect the device. It is therefore of the utmost importance that the operational aspects, as well as possible aging effects be both recognized and fully understood before installation. With this in mind, design investigations, discussed in later chapters, have been carried out to achieve this goal.

Chapter 3

Principles of Particle Detection

One of the most classical methods of particle detection is to separate the charges, created by the passage of energetic particles through matter, by using an electric field, and to register their induced current pulse upon electrodes. The following sections will describe the relevant physics behind these devices.

3.1 Charged Particle Creation

When energetic particles pass through matter the likelihood is that some of their energy will be lost to the matter, due to interactions. However, certain particles at certain energies interact via different processes to deposit this energy. The main considerations here are the interactions of heavy charged particles, electrons and photons, with matter (for reasons presented in section 5.3.1).

3.1.1 Heavy Charged Particle Matter Interactions

When an energetic particle traverses matter there are several methods of interaction that may occur. The preference of these interactions is dependant on how much energy the projectile has. This is shown in figure 3.1 below for muons, at a range of energies, passing through a copper target. Generally speaking the energy lost from the particle is defined by the stopping power of the material.

The most likely method to occur, for the momentum energies considered in this investigation (of the order of 0.1 to 100 GeV, see section 5.3.1), is that defined by the Bethe-Bloch equation below, derived from [5]. This describes the energy lost by a charged particle (dE_n), as it traverses matter (dx), due to electromagnetic interactions (dE_n/dx measured in MeV cm^{2}g^{-1})

$$-\frac{dE_n}{dx} = K_0 z^2 \frac{Z}{A}\frac{1}{\beta^2}\Big[\frac{1}{2}ln\frac{2m_e c^2\beta^2\gamma^2 E_{max}}{I_e^2} - \beta^2 - \frac{\delta}{2}\Big]. \tag{3.1}$$

The process of energy loss is caused by the electric field of the charged particle reacting with the atomic electrons of the material. This interaction deflects the

projectile through the matter, causing it to loose momentum. This lost energy is then transferred to the electrons which, if the energy is sufficient, will be ejected from the atoms of the material (ionisation). If there is no liberation of electrons, an excitation of the atom is likely to occur instead, which, in turn may produce a photon when the electrons return to their ground state. This field reaction method is more likely than direct collisions with the material's atoms, by many orders of magnitude [8].

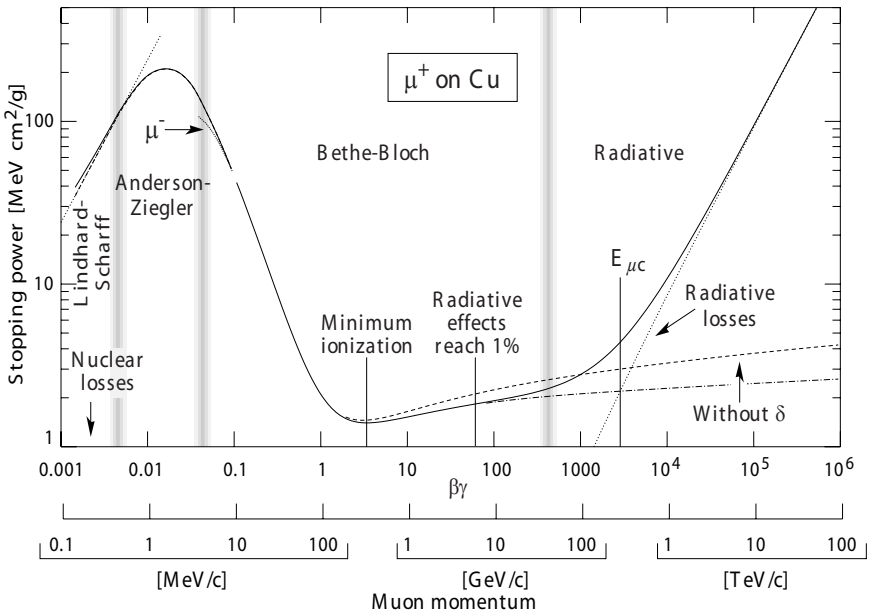

Figure 3.1: *Stopping power for positive muons in copper as a function of muon momentum, taken from [5]. Solid curves indicate the total stopping power. δ is the density affect correction factor.*

In equation (3.1) Z is the atomic number and A is the atomic mass of the medium, while z is the charge magnitude of the incident particle. γ has the usual definition $(1-\beta^2)^{-1/2}$, with β equal to the velocity of the incident particle (v) divided by the speed of light (c), $\beta = v/c$. K_0 is given by

$$K_0 = \frac{N_A e^4}{4\pi m_e c^2 \varepsilon_0^2}, \tag{3.2}$$

for which N_A is Avogadro's number and e is elementary charge. ε_0 is the permittivity of free space.

The maximum transferable kinetic energy for an electron, released due to an interaction, (E_{max}) is described by

$$E_{max} = \frac{2m_e c^2 \beta^2 \gamma^2}{1 + 2\gamma m_e/M + (m_e/M)^2}, \tag{3.3}$$

where m_e and M are the masses of an electron and the incident particle, respectively.

In equation (3.1) I_e is the mean excitation energy, which is generally a measured quantity for each material[1].

At high energies, usually when plasmas are considered, the electric field of the particle flattens and extends, contributing to equation (3.1). However, real media may become polarized and limit the field extension. This has the effect of lowering the amount of energy a particle will lose when it transverses matter. This affect is represented by the density effect correction factor, δ

$$\delta = \begin{cases} 2(ln10)x - \bar{C} & \text{if } x > x_1; \\ 2(ln10)x - \bar{C} + a(x_1 - x)^k & \text{if } x_0 < x < x_1; \\ 0 & \text{if } x < x_0 \text{ (nonconductors);} \\ \delta_0 10^{2(x-x_0)} & \text{if } x < x_0 \text{ (conductors)} \end{cases} \tag{3.4}$$

Here $x = log_{10}(p/Mc)$ and $\bar{C}$ is the high energy correction factor, derived by equating (3.4) with the assumption that at very high energies $\delta/2 \rightarrow ln(\hbar\omega_p/I) + \beta\gamma - 1/2$. However, for most gases δ is equal to 0, and therefore neglected.

Inspection of equation (3.1) shows that, the rate of energy loss is proportional to the incident particles energy. This is clearly shown in the figure 3.2, when considering the relativistic momentum (p).

As the momentum initially increases the rate of energy loss rapidly decreases to a minimum point (minimum rate of energy loss, $\{dE_n/dx\}_{min}$). After this it slowly increases, until reaching very high momenta where the energy loss rapidly will increase again (as shown in figure 3.1). The region in between the minimum ionising rate and the radiation losses provides a useful method of particle and medium identification as the specific masses give individual characteristic curves.

3.1.2 Delta-ray Production

Electrons liberated via ionisation will be ejected with an energy E_n, which may take a maximum value of E_{max}. If this energy is large enough (greater than the first ionising potential of the medium), these released electrons may also cause secondary ionisation, causing a slight fluctuation in total energy loss predicted by equation (3.1). This type of electron is generally called a δ-electron or delta-ray.

The approximate expression for the probability (P) of an electron receiving energy E_n as the ionising particle passes through matter of thickness x (as derived by Ritson [10]) is given by

$$P(E_n)dE_n = \frac{K_0}{\beta^2}\frac{Z}{A}\frac{x}{E_n^2}dE_n. \tag{3.5}$$

[1]A selection of relevant values have been included in Appendix A. Further to this Seltzer & Berger [6], has a selection of over two hundred common compounds and elements.

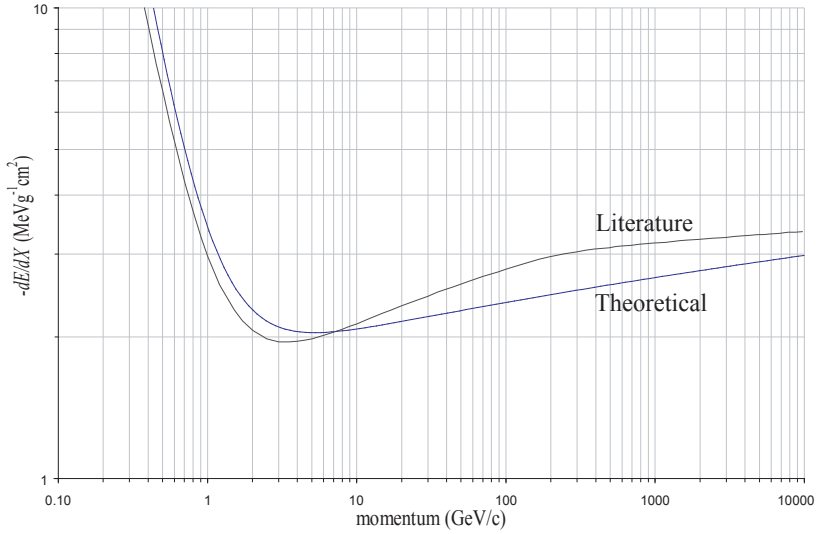

Figure 3.2: *Rate of energy loss of protons passing through helium gas. Theoretical is calculated using equation 3.1, Literature is taken from [5]. The differences between the curves is a direct consequence of density effect contributions, which is not accounted for in the theoretical curve. The error between the theoretical and published minimum values is approximately 5%, taken from [2].*

Integration of the equation therefore produces an expression for the approximate number of electrons with energies between E_0 and E_{max}.

$$N(E_n \geq \ E_0) = \int_{E_0}^{E_{max}} P(E_n)dE_n = \frac{K_o}{\beta^2}\frac{Z}{A}x\Big(\frac{1}{E_0} - \frac{1}{E_{max}}\Big). \tag{3.6}$$

Using (3.6), with the consideration of a beam of 1 GeV protons passing through 1 cm of argon, a graph showing the number of δ-electrons created, for energies from the first ionising potential[2] (15.8 eV for argon) to E_{max}, can be produced (figure 3.3).

3.1.3 Electron Interactions with Matter

When an electron (or positron) traverses matter the processes of energy loss differ from that described for heavy charged particles. The rate of energy loss still remains proportional to the impact particles energy, but at low energies (in the order of less than 10 MeV) the main process of energy loss of electrons is

[2]A selection of first ionising potentials has been provided in Appendix A. A larger selection may be obtained from [34].

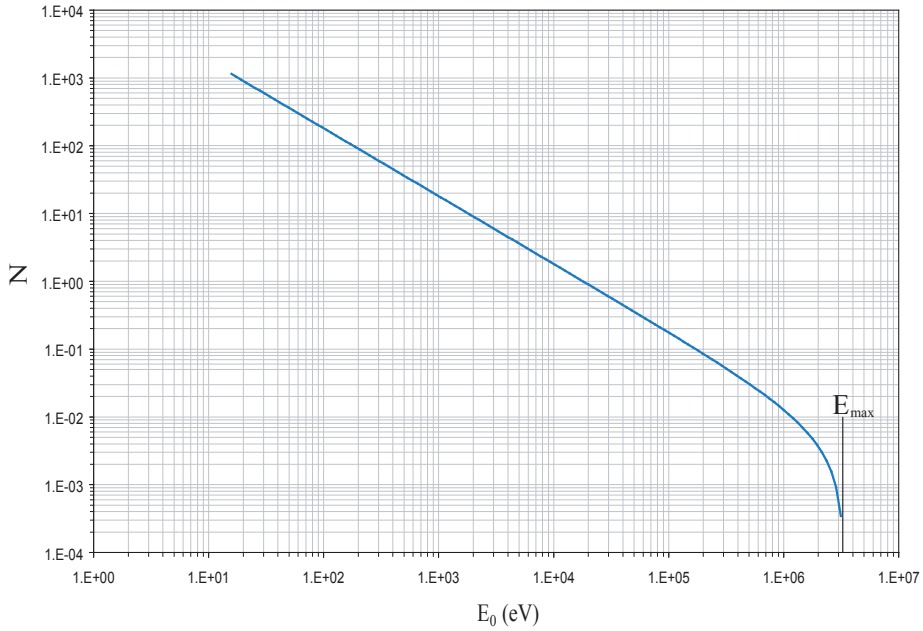

Figure 3.3: *Computed number of δ-electrons produced in 1cm of argon at standard temperature and pressure (STP)*

that of ionisation, similar to that outlined above. However, due to their charge, size and kinematics, there must be an adaptation to the Bethe-Bloch equation for electrons and positrons. For higher energies the process of energy loss is predominately determined by Bremsstrahlung processes (see Fig 3.4)

The slight difference in the curves of the electron and positron (which are identical accept for charge sign) come about due to different space charge interactions with the molecules.

Electron and Positron Ionisation

The stopping power, in units of MeV $\mathrm{cm}^2\mathrm{g}^{-1}$, for electrons and positrons through matter (as derived by Seltzer & Berger [6]) is given by the expression,

$$\frac{dE_n}{dx} = \frac{K_0}{2\beta^2}\frac{Z}{A}B(E_n). \tag{3.7}$$

$B(E_n)$ is the stopping number, of the electrons or positrons, at kinetic energy E_n and is defined by

$$B(E_n) = B_0(E_n) - 2ln(I_e/mc^2) - \delta. \tag{3.8}$$

Here, mc^2 is the particles rest energy (for electrons and positrons this is

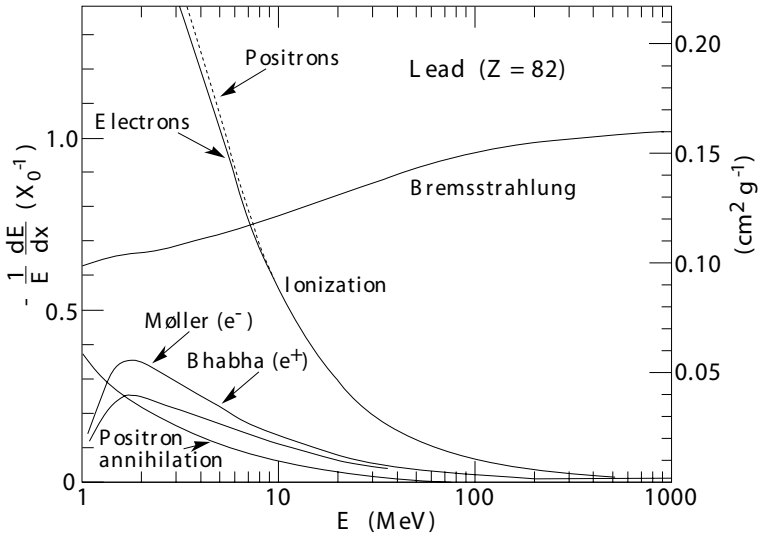

Figure 3.4: *Rate of energy loss per radiation length as a function of electron or positron energy, taken from [5].*

0.511 MeV). $B_0(E_n)$ is an individual function for either electrons,

$$B_0(E_n) = ln\Big[\tau^2\frac{(\tau+2)}{2}\Big] + \frac{\big[1+\frac{\tau^2}{8}-(2\tau+1)ln2\big]}{(\tau+1)^2}, \tag{3.9}$$

or positrons,

$$B_0(E_n) = ln\Big[\tau^2\frac{(\tau+2)}{2}\Big] + 2ln2 - \Big(\frac{\beta^2}{12}\Big)\Big[23+\frac{14}{(\tau+2)}+\frac{10}{(\tau+2)^2}+\frac{4}{(\tau+2)^3}\Big], \tag{3.10}$$

where $\tau = E_n/mc^2$ is the kinetic energy in units of the rest energy. δ and I_e are again the density effect correction factor and the mean excitation energy, respectively (equation 3.1).

Bremsstrahlung

Bremsstrahlung energy loss occurs when the incident electrons are decelerated by the field of a target atom. Their lost kinetic energy is emitted in the form of photons (or bremsstrahlung radiation). The rate of energy loss, for electrons and positrons passing through matter, due to bremsstrahlung is given by,

$$-\frac{dE_n}{dx} = 4\alpha N_A\frac{Z^2}{A}r_e^2E_n\cdot\ln\frac{183}{Z^{1/3}}, \tag{3.11}$$

where Z and A are the atomic number and atomic weight of the medium. N_A is Avogadro's number and E_n is the incident particles energy. α is the fine structure

constant defined as

$$\alpha = \Big(\frac{e^2}{4\pi\varepsilon_0\hbar c}\Big),$$

and r_e is the classical electron radius, given by

$$r_e = \Big(\frac{e^2}{4\pi\varepsilon_0 m_e c^2}\Big).$$

3.1.4 Photon Interactions with Matter

The processes involved when photons pass through matter are considerably different from those of the charged particles. Rather than electromagnetic interactions with the atomic electrons, there must be an actual absorption or single localized event within the matter. The photon-mass absorption length (or mean free path) is defined as

$$\lambda = \Big(\frac{\rho}{\mu}\Big), \tag{3.12}$$

where μ is the mass absorption coefficient (in cm g^{-1}) and ρ is the density of the matter, [5]. This quantity can then be used to calculate the intensity of the photons (I) remaining after traversing matter of thickness χ (in g/cm),

$$I = I_0 e^{-(\frac{\sigma N \chi}{\rho})} = I_0 e^{-(\frac{\chi}{\lambda})}. \tag{3.13}$$

σ is defined as the cross-section of the relevant reaction and N is the number density of the traversed substance. The absorption length is dependent on the material of the substance and the energy of the photon. This can be clearly shown for a selection of materials[3] in figure 3.5.

This energy dependence also extends to the processes that are involved in the photon-matter interactions. At low energies, up to several keV, the main process is the photoelectric absorption. As energies increase, up to a few hundred keV, Compton scattering becomes the dominant process, followed by electron-positron pair production for even higher energies.

Photoelectric Absorption

Photoelectric absorption occurs when the energy of the incoming photon, hf (where h is Plank's constant and f is the photon frequency), is greater than or equal to the energy of the electron shell of the absorbing atom (E_j), therefore $hf \geq E_j$. When this is the case an excitation of an electron in the shell takes place. If this excitation has an energy greater than the first ionising potential, Φ (effectively the minimum amount of energy required to escape from the atom's

[3]Data for photons of energies between 30 eV and 100 GeV, and for all elements, can be found in [35] and [34].

attractive electric forces), the electron will be ejected with an energy E_{elec}. This is defined by Einstein's photoelectric equation

$$hf = E_{elec} + \Phi \tag{3.14}$$

The excited atom can then return to it's ground state via either:

- fluorescence, where an electron from an energy shell $E_i < E_j$ moves to the j shell with the emission of a photon, of energy $E_j - E_i$,

- Radiationless transition, effectively a rearrangement of lower energy shells, causing an electron emission of energy approximately equal to E_j.

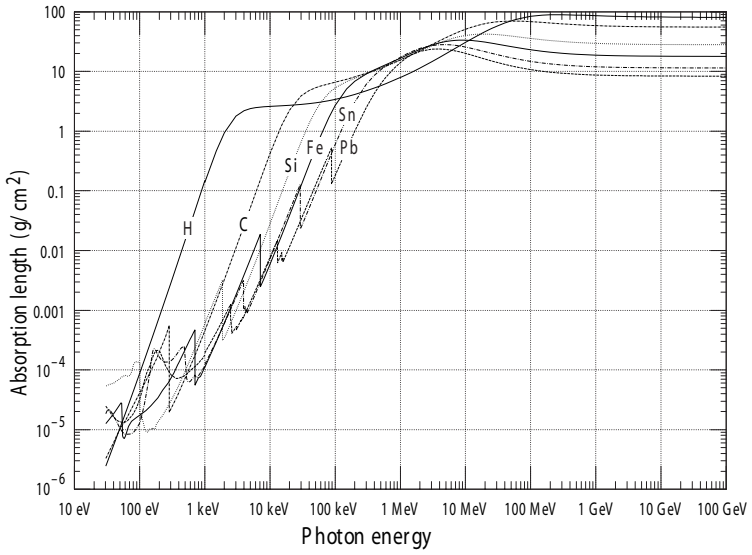

Figure 3.5: *The photon mass absorption length for various elemental absorbers as a function of photon energy, taken from [5]*

Compton Scattering

Compton scattering becomes more dominant when the energies of the photons exceed the highest atomic energy levels. Now the photon is scattered, by an angle θ, due to interactions with loosely bound electrons of the traversed material. This scattering causes a loss in energy and momentum ,$\Delta(1/hf)$, that can be described by the Compton shift equation

$$\Delta(1/hf) = \frac{1}{mc}(1 - cos\theta). \tag{3.15}$$

The loosely bound electrons will then be emitted with an energy $\Delta(1/hf)$.

Pair Production

This method of matter interaction is possible above energies of 1.02 MeV (the sum of the electron and positron masses). The premise of the process is that photons, with a correct momentum vector in the vicinity of a nucleus, can become trapped within the nucleus' coulomb field causing it to directly convert their energy into matter (ie. an electron and a positron). Energy in excess of 1.02 MeV will be converted into additional kinetic energy for the new particles. The positron usually undergoes quick annihilation into two photons.

3.2 Separation of Charged Particles

When a charged particle pair is created the likelihood is, if there are no external influences, that the pair will recombine and neutralize each other, due to the attractive forces between the particles (as stated by Coulomb's law (3.16)).

$$F = \frac{1}{4\pi\varepsilon_0}\frac{|q_1||q_2|}{r^2}, \tag{3.16}$$

where q_1 and q_2 are the respective charges and r is the distance between them.

However, in most particle detection devices, it is required that the pair remains separated so that they may be registered. A method of separating the particles is to apply a field to their environment.

3.2.1 Charged Particles in Electromagnetic Field

The force $\mathbf{F}$ acting on a charged particle passing through an electromagnetic field, at velocity $\mathbf{v}$, is given by the Lorentz force equation below

$$\mathbf{F} = q(\mathbf{E} + \mathbf{v} \times \mathbf{B}), \tag{3.17}$$

where $\mathbf{E}$ is the electric field vector and $\mathbf{B}$ is the magnetic field vector. In the previous consideration of a charged particle pair, if the resultant Lorentz force is greater than the attractive Coulomb force between the two particles, the pair will remain detached and accelerate away from each other. The rate at which this occurs can be derived by inspection of Newton's second law

$$\mathbf{F} = m\mathbf{a} = m\frac{d\mathbf{v}}{dt}. \tag{3.18}$$

It is now required to consider the concepts of special relativity, where $m = m(v) = m_0\gamma(v)$, in which m_0 is the rest mass.

$$\mathbf{F} = \frac{dm\mathbf{v}}{dt} = \mathbf{v} \cdot \frac{dm}{dt} + m \cdot \frac{d\mathbf{v}}{dt}. \tag{3.19}$$

From Einstein's mass-energy relationship ($E_n = mc^2$) this becomes,

$$\mathbf{F} = \frac{\mathbf{v}}{c^2} \cdot \frac{dE_n}{dt} + m \cdot \frac{d\mathbf{v}}{dt}. \tag{3.20}$$

Force can also be expressed as a function of the "work done" (W), which is the energy given to the particle to move it a distance x

$$\mathbf{F} = \frac{dE}{d\mathbf{x}} = \frac{W}{x}\hat{i}_x,$$

with this, equation (3.20) becomes

$$\mathbf{F} = m\frac{d\mathbf{v}}{dt} + \Big(\frac{\mathbf{F}}{c^2}\frac{dx}{dt}\Big)\mathbf{v} = m\mathbf{a} + \Big(\frac{\mathbf{F}\cdot\mathbf{v}}{c^2}\Big)\mathbf{v}, \tag{3.21}$$

by inserting equation (3.17), an expression for the acceleration of a particle in an electromagnetic field can be achieved,

$$m\mathbf{a} = q\Big[\mathbf{E} - \Big(\frac{\mathbf{E}\cdot\mathbf{v}}{c^2}\Big)\mathbf{v} + \mathbf{v}\times\mathbf{B}\Big]. \tag{3.22}$$

In order to expand this equation further the components of the fields must be considered. As mentioned above, the electric component of the field will act parallel to the motion of the charged particle, therefore $\hat{f} = \hat{v}$. The magnetic component of the field acts perpendicular to the motion of the particle, however this term may be considered to be 0 for this investigation. The primary reason for this assumption is that only an electric field will be applied to the BLMs installed in the LHC. Magnetic fields, which will be present in that environment, will have little or no effect at the positions of the detectors, [36]. Equation (3.22) therefore becomes

$$\begin{aligned} \mathbf{a} &= \frac{q\mathbf{E}}{m_0\gamma}\Big[1 - \Big(\frac{v^2}{c^2}\Big)\Big] + \frac{q(\mathbf{v}\times\mathbf{B})}{m_0\gamma} \\ \Rightarrow \mathbf{a} &= \frac{q\mathbf{E}}{m_0\gamma^3} \approx \frac{q\mathbf{E}}{m_0} \text{ (non-relativistic).} \end{aligned} \tag{3.23}$$

Therefore, the acceleration of a particle is directly proportional to the strength of the electric field that is acting upon it.

3.2.2 Electric Field Strength

An electric field may be created by applying a potential difference between two conducting surfaces, or plates. The strength of the potential difference, or the voltage, is expressed as

$$V = \int_{-}^{+} \mathbf{E}ds, \tag{3.24}$$

where E is the strength of the electric field and ds is the directional component of the field. A direct consequence of applying a field between the plates is that potential energy may be stored in the electric field, effectively creating a capacitor with a capacitance of

$$C = \frac{q}{V}. \tag{3.25}$$

The strength of the electric field may be calculated from Guass' law

$$\varepsilon_0 \oint \mathbf{E}.d\mathbf{A} = q,$$

where q is a charge on the plates enclosed by a Gaussian surface, and $\oint \mathbf{E}.d\mathbf{A}$ is the net electric flux through that surface. If it is assumed that the vectors of flux, $\mathbf{E}$ and $\mathbf{A}$, are parallel as it passes through the surface, the equation now becomes

$$E = \frac{q}{\varepsilon_0 A}, \tag{3.26}$$

where E is the magnitude of the field and A is the surface area of the electrodes. By combining equations (3.24) and (3.26) an equation for the voltage between two plates, as a function of the geometry of the plates, is achieved, equation (3.27).

$$V = \frac{q}{\varepsilon_0} \int_{-}^{+} \frac{ds}{A}, \tag{3.27}$$

3.2.3 Space Charge Effects

In a particle detector it is likely that there will be more than one charge present. As dictated by Coulombs law (3.16), these charges will naturally have an affect on each other. However, for low charge densities this affect is minute and the particles can be considered separate. The criterion for this can be derived from Poisson's one dimensional equation [37],

$$\nabla^2 V = -\frac{\rho}{\varepsilon_0},$$

where ρ is the charge density. Using equation (3.24) and $\rho = nq$, the equation becomes

$$\frac{d\mathbf{E}}{dx} = \frac{nq}{\varepsilon_0}, \tag{3.28}$$

with q equal to the elementary charge and n being the charge number density, measured in cm^{-3}. The condition for minimum space charge distortions of an applied field (E_0) is therefore

$$\int_a^b n dx \ll \frac{\varepsilon_0}{e} \int d\mathbf{E}, \tag{3.29}$$

which is dependant on both the strength of the field and the dimension of the detector, x. Equation (3.29) shows that, should the charge density increase beyond this boundary, they will begin to contribute to the field more significantly[4]. However, in this document it has been assumed, quite reasonably, that there are no space charge affects within the equipment, this will become clearer in later sections.

3.2.4 Movement of Charged Particles Through Matter

A charged particle, moving in an electric field, will gain on average, a set amount of energy from the field. However, if it is moving through matter it will always have limitations on the velocity at which it moves, beyond the obvious restriction of the speed of light.

Interactions with the molecules of the transversed material, will cause a loss in the energy of the particle. However, there is an equilibrium energy (ϵ), defined as the average balance between the energy lost via matter interactions and the energy gained from the field. This equilibrium energy duly corresponds to the maximum obtainable velocity of a charged particle passing through a medium, under the influence of an electric field, or the drift velocity (v_{drfit}).

If this equilibrium energy is small compared to the thermal energy of the gas, $\epsilon \ll (3/2)kT$ (k = Boltzmann's constant & T = absolute gas temperature), the collisions are said to be elastic, as no net movement of gas molecules will be occur. This is usually the case for ions, whose large mass restricts acceleration between collisions and causes a large fraction of the energy gained, to be lost during interactions. As a consequence the velocity of the ions is dictated by the thermal energy of the gas, and only a small fraction is due to the field.

Electrons, whose masses are considerably smaller than ions, have larger acceleration in the field and store energy between collisions to a greater degree. Therefore, for anything but low fields, the electrons can easily surpass the thermal energy of the gas ($\epsilon \gg (3/2)kT$), which brings the onset of inelastic collisions, as the energy transferred to the gas causes it to become excited, creating a net movement (increased vibrations). In this case their velocity becomes a function of the energy lost during an interaction.

The motion of electrons through gas also differs from that of ions. Due to their large masses, ions will not significantly deviate from their trajectory after collisions. Electrons, on the other hand, will be deflected and recoiled considerably, meaning their drift velocity is considered the net movement through the material, rather than the velocity which they travel at due to their energy.

[4] A space charge distortion effect has been calculated by Boag in [19] for large charge densities

3.2.5 Ion Drift Velocity

The drift velocity of an ion passing through a gas, under the influence of an electric field (E), is generally given by

$$\mathbf{v_i} = K\mathbf{E} \tag{3.30}$$

K, the ion mobility (measured in $\mathrm{cm^2V^{-1}s^{-1}}$), is the relationship of a specific particle traversing a specific gas, of absolute temperature T, as shown below. It is assumed that only elastic collisions occur and hence $\epsilon_{Eq} \ll (3/2)kT$.

$$K = \frac{e}{N}\Big(\frac{1}{3\mu_m k T_{eff}}\Big)^{\frac{1}{2}} \frac{1}{Q_D(T_{eff})}, \tag{3.31}$$

where k is the Boltzmann constant and T_{eff} is the effective ion temperaure, which is related to the gas' absolute temperature (T) and mass (M) by

$$\frac{3}{2}kT_{eff} \equiv \bar{\epsilon} = \frac{3}{2}kT + \frac{1}{2}Mv^2. \tag{3.32}$$

Here $\bar{\epsilon}$ is the mean relative energy. As the expression contains v, the randomly orientated velocity, a dependence upon the strength of the field also become apparent. This dependence, usually given as a function of the electric field strength (E) to neutral gas number density (N) ratio, E/N (measured in Townsends, Td, which is 10^{-21} $\mathrm{Vm^2}$), is shown in figures 3.6(a) & 3.6(b).

μ_m, of equation (3.31) is the reduced mass function relating the molecular gas mass to the ionic mass (m)

$$\mu_m = \frac{mM}{(m+M)}. \tag{3.33}$$

$Q_D(T_{eff})$, the diffusion cross section, is defined in terms of the scattering angle (θ) of a particle through some matter and the differential cross section of the passage ,$\sigma(\theta, \bar{v_r})$ (where $\bar{v_r}$ is the mean relative speed)

$$Q_D(T_{eff}) \equiv 2\pi \int_0^{\pi} (1 - cos\theta)\sigma(\theta, \bar{v_r}) sin\theta d\theta. \tag{3.34}$$

Ion mobility is a well-documented experimental value for many combinations of charged particles, gases, temperatures and field-density ratios[5]. Therefore extrapolations from data tables provides an equally accurate method of obtaining mobility values.

Figures 3.6(a) and 3.6(b), plotted from [16] experimental values, shows the dependence of K on E/N for N_2^+ ions in N_2 gas and how that dependence

[5]A good selection can be found through [15] and a range of articles written in the Atomic Data and Nuclear Data Tables publication, entitled Transport Properties of Gaseous Ions over a wide Energy Range. There are several parts, but [16], [17] and [18] have been referenced.

Figure 3.6: *Mobility of N_2^+ ions in N_2, plotted from [16]. Accuracy stated as ± 3%. For (a), mobilities > 200 Td may be estimated from the expression K = 3.27 - 0.83 ln E/N, R^2 = 0.97.*

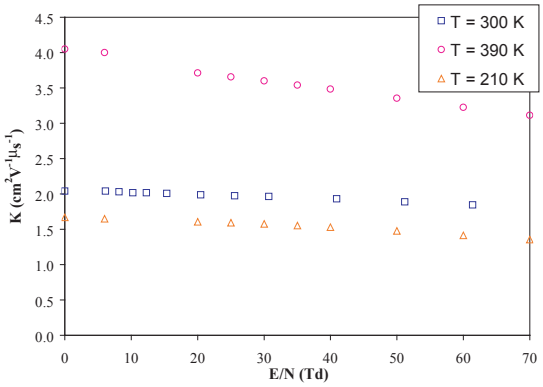

(a) *Mobility against E/N for several temperatures.*

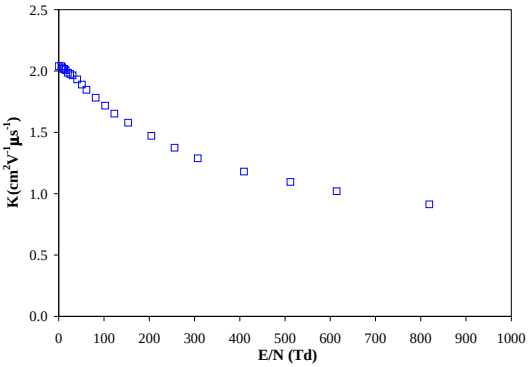

(b) *Mobility against E/N, at 300K.*

varies with temperature. It is useful to note that at low fields the mobility remains almost constant and then decreases logarithmically above a threshold field strength (approximately 30 Td).

Figure 3.7, alternatively demonstrates how the mobility of charged particles, passing through argon gas at a set field (10 Td) and temperature (300 K), is dependant on their atomic molecular masses (m_m).

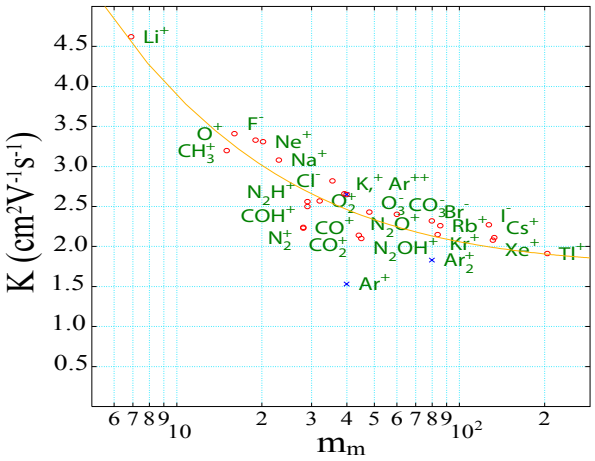

Figure 3.7: *Variation of mobility on atomic molecular mass. taken from [30], courtesy of Dr. R. Veenhof.*

It is highly important, especially when considering possible gasses for detectors, to observe that an ion passing through its own gas (Ar^+ in Ar, for this example) will have a lower than expected mobility. A comparison between Ar^+ and K^+, for example, with masses 39.9 and 39.1 AMU respectively, show a considerable difference in mobility, almost 50%.

The reason for this phenomenon is that it is possible for two common particles to exchange charge during an interaction. The result is that the initial charged particle (which would have acquired kinetic energy from the field) will become neutral and therefore unaffected by the electric field, eventually stopping its motion. The newly charged particle (initially with little or no energy) will acquire energy from the field and accelerate. This 'stop-start' system of propagation, shown in figure 3.8, will reduce the average drift velocity through the gas.

Figure 3.8: *Stop-Start process of ion propagation through parent gas.*

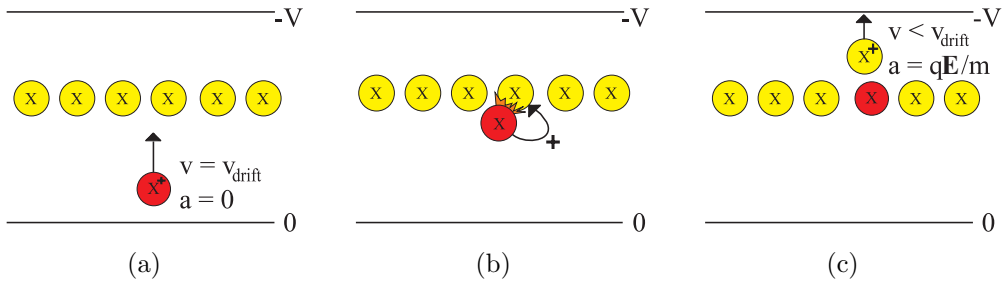

Adding an impurity to the gas increases the ion mobility slightly, but as stated by Mason and McDaniel [15] the affect is more profound for electrons than ions, as will be shown in the section 3.2.6.

The mobility (K) of a charged particle, in a mixture of neutral gasses, can be related to the mole fraction (X_j) of each gas (j) and that particles mobility in each individual gas (K_j). This is equated by Blanc's Law[6], below.

$$\frac{1}{K} = \sum \frac{X_i}{K_j} \tag{3.35}$$

Calculating the mobility is simplified if there is considerably more of one gas than the others (ie. for a two gas system % of $X \gg$ % of Y). Statistically, this allows only the considerations of the mobility of X^+ through X and the mobility of Y^+ through X, as it is more likely that Y ions will be ionised and be affected by

[6]Equation (3.35) has been simplified for small fields, the full expression, taken from [17], is given by

$$\frac{1}{K} = \sum_j \frac{X_j}{K_j}\Big[1 + \frac{1}{2}\Big(\frac{K_j'}{1+K_j'}\Big)(1-\delta_j)\Big],$$

where K_j' is the field derivative of K' and δ_j is the correction term.

the main gas (X) than the main gas (X) being ionised and being considerably affected by the impurity (Y) .

3.2.6 Electron Drift Velocity

At very low E/N values the drift velocity of electrons through a gas remains true to that described in the previous section. However, for large E/N values (when $\epsilon_{Eq} \gg (3/2)kT$) the previous assumptions become invalid and a new expression must be considered. The following formula, derived by Huxley and Crompton [14], describes the electron drift velocity (v_e) through a gas, showing that it is now dependant on the field strength and the gas through which it passes.

$$v_e = -\frac{4\pi}{3}\int_0^\infty v\frac{eE}{m\nu}\frac{d}{dv}f_0 dv. \tag{3.36}$$

It is important to know here that v is equal to the randomly orientated velocity of the electron which, when considering it's momentum (p), is effectively the energy of the electron,

$$E_n = \sqrt{p^2c^2 + m_e^2c^4}.$$

The term ν is the effective collision frequency within the gas and is given by

$$\nu = Nv\sigma_{m_{el}}(v),$$

where N is again the number density of the gas molecules and $\sigma_{m_{el}}$ is the electron momentum transfer cross section. This can be derived by the expressions

$$\begin{aligned}
\sigma_{m_{el}}(v) &= \sigma_{0_{el}}(v) - \sigma_{1_{el}}(v), \\
\sigma_{0_{el}}(v) &= 2\pi\int_0^\pi P(\mathbf{x}, v)sin\mathbf{x}\ d\mathbf{x}, \\
\sigma_{0_{el}}(v) &= 2\pi\int_0^\pi P(\mathbf{x}, v)cos\mathbf{x}sin\mathbf{x}\ d\mathbf{x},
\end{aligned}$$

in which $P(\mathbf{x}, v)$ is the differential scattering cross section and $\mathbf{x}$ is the position. The velocity distribution function, f_0, is expressed as

$$f_0(v) = f_0(v_0)exp\Big(-\frac{3m_e}{M}\int_0^v \frac{vdv}{\xi^2 + \bar{v}_c^2}\Big),$$

where $f_0(v_0)$ is the normalisation constant and ξ is simply the expression $e\mathbf{E}/m\nu(v)$. M and $\bar{C}_c^2$ are the mass and average velocity of the gas molecules respectively.

The main assumption here is that the velocity distribution function is independent of position, and is without the presence of space charge affects. This assumption clearly fails for large initial ionising densities and for certain

geometries, as described in Chapter 4. Huxley and Crompton [14] have also derived a further formula that tackles this situation, however it is unnecessary to consider this equation for the purposes of this investigation.

As mentioned in section 3.2.5, the drift velocity of electrons is drastically altered by the addition of an impurity to the gas. In fact, the word impurity can be a grossly misunderstood because in some instances it is required for better operation. The figure 3.9 represents how the calculated drift velocity of an electron changes with varying concentrations of $NeCO_2$ gas.

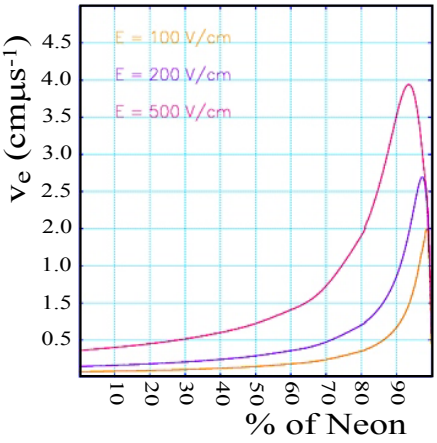

Figure 3.9: *The variation of electron drift velocity as a function of percentage of neon, in a neon carbon-dioxide mixture. Several field strengths have been plotted. Adapted from [29].*

This increase in drift velocity can be explained by considering the relationship between the velocity gained from the field (v) and the average fractional energy loss per collision ξ, derived from [7]

$$v_e = \frac{\xi}{v}$$

The addition of an impurity (especially a polyatomic gas) causes inelastic collisions which increase λ at the same time as lowering v (as inelastic collisions will cause the particle to lose more energy). This will therefore have the overall affect of increasing the drift velocity.

From figure 3.9 it is also possible to see that there is an inflection point after which increases in the concentration of CO_2 will decrease v_e. This maximum point, as would be expected, changes with the strength of the field.

However, the addition of an electronegative impurity (such as oxygen or water) causes a decrease in the height of the electron signal pulse. This is because some electrons will be attracted to and captured by, the pollutant electronegatvie gas molecules, reducing the total number that reach the electrodes.

3.3 Pulse Formation

When a charge pair is created in an electric field, the resultant positive and negative ions will drift towards the cathode and the anode electrodes, respectively (as discussed in section 3.2). Upon impact with an electrode the relevant particle will change the potential of that individual electrode by $\pm e/C$, from equation (3.25), where e is the charge and C is the capacitance of the two electrode system. However, as soon as the charges are created they also induce a change in potential on both electrodes as they move.

The induced potential (V_n) of an electrode n at a point in time (t), is therefore given as a function of both the positive, $-q_+(t)$, and negative, $-q_-(t)$, charges at time t. That is

$$V_n(t) = \frac{q_+(t) + q_-(t)}{C}. \tag{3.37}$$

In detectors, the charge pair can be thought of as a fast moving electron and a slow moving ion (by orders of magnitude, section 3.2). With this assumption, when the electron has been collected at the anode, at time t_1, the ion will not have moved. This would therefore make the induced potential on the electrode

$$V_{anode}(t_1) = \frac{q_+(t_1) - e}{C},$$

Where the signal induced by the ion, upon the electron impacting electrode (the anode), may be considered as an impedance to the total signal. Therefore the magnitude of the signal on the anode is lower than $-e/C$ while the ion is still within the system. Hence, when the ion has reached the cathode, at time t_2 (therefore $q_+(t_2) = 0$) the induced potential upon the anode will be

$$V_{anode}(t_2) = \frac{-e}{C}.$$

As the induced signal upon the cathode is equal in magnitude, but opposite in sign, to that of the anode, the full signal pulse for the entire system may be thought of as the induced signal upon a single electrode, when both charged particles have been collected, as shown in figure 3.10. If more than one charge pair is created, as would be expected within a detector, the total signal is a superposition of all such curves.

The shape and magnitude of the induced potential may be calculated from Green's reciprocation theorem [7]. This states that a set of n charges $q_1, q_2, \cdots q_n$ on n conductors, will induce potentials $V_1, V_2, \cdots V_n$ on the conductors, and if these charges are replaced by $q'_1, q'_2, \cdots q'_n$, which induce $V'_1, V'_2, \cdots V'_n$, then

$$\sum q_n V'_n = \sum q'_n V_n. \tag{3.38}$$

In a simple two electrode system (1 and 2) the induced charge q_1 is on plate 1 and the induced charge q_2 is on plate 2. The charge (that is the object which causes

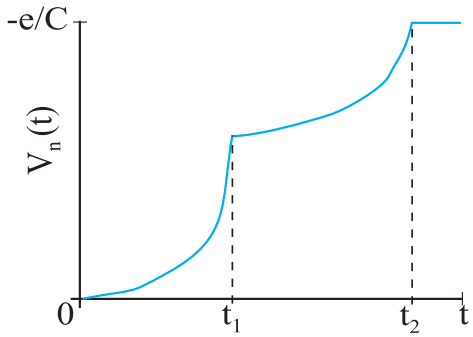

Figure 3.10: *Potential signal formation with time.*

the induction of charge upon the electrodes) q_3', whether it be ion or electron, has a magnitude of ze and may be considered on a infinitely small electrode (3). Initially the corresponding potentials are $V_1 = V_2 = 0$ and V_3. The potentials created when the charge reaches an electrode (hence $q_3' = 0$) are then V_1', V_2' and V_3', which is the potential between the initial position of the charge and the plate upon which it impacts. The theorem then becomes

$$q_1 V_1' + q_2 V_2' + q_3 V_3' = 0,$$

Under the assumption that the potential changes by the electrodes are small compared with the induced inter-electrode potentials, which is observable in most electrode particle detectors, $q_1 + q_2 + q_3 = 0$, the equation may be written in terms of the induced charges

$$q_1 = -ze\Big(\frac{V_3'}{V_1'} - 1\Big), q_2 = -ze\Big(1 - \frac{V_3'}{V_2'}\Big). \tag{3.39}$$

Now if it is taken that q_1 is the signal induced positive charge on an electrode and q_2 is the signal induced negative charge on the same electrode, $V_1' = V_2'$ and V_3' becomes a function of each particles induced potential between itself and the electrode n (ie. V_{ion}' and V_e'). This is a reasonable condition to make as the total induced signal is observed on a single plate. Finally, by substituting (3.39) into (3.37), and from equation (3.27) the expression for the induced potential on a single plate, is given by

$$V_n(t) = -\frac{ze}{C}\left[\frac{\int_n^{y_{ion}(t)} A^{-1} ds_{ion} - \int_n^{y_e(t)} A^{-1} ds_e}{\int_-^+ A^{-1} ds}\right], \tag{3.40}$$

where $y_{ion}(t)$ and $y_e(t)$ are the distances of the respective charged particles from the electrode n at time t. The terms A and ds again refer to the surface area of the electrodes and the direction of the field.

3.3.1 Current Pulse

In practice, it is more convenient to measure the current that flows within the chamber, rather than the potential that is induced. Given that the current, I, is defined as

$$I = \frac{dq}{dt},$$

by using the formulae $q = CV$, the expression for the current flowing through the chamber can be achieved, that is

$$I_n(t) = C\frac{dV_n(t)}{dt} = -\frac{d}{dt}ze\left[\frac{\int_n^{y_{ion}(t)} A^{-1}ds - \int_n^{y_e(t)} A^{-1}ds}{\int_-^+ A^{-1}ds}\right]. \tag{3.41}$$

Examples of how to apply this equation to ionisation chambers may be found in section 6.1.

3.3.2 Number of Primary Ionising Particles

The formation of a pulse in a detector comes about from the movement of charge pairs, within an electric field, that were created by an initial ionising particle. Therefore, in order to know the number of primary ionising particles, the desired function of the BLMs, the total number of created secondary charges (N_{sec}) must be known. This may be determined from either the total integrated charge (Q) or the total energy deposited between the detector's plates (E_{dep}), and is given by

$$N_{sec} = \frac{Q}{ze} = \frac{E_{dep}}{E_w}. \tag{3.42}$$

z represents the magnitude of the charges involved, however, from earlier assumption that only charge pairs are created (ie. one ion X^+, and one electron e^-), this will be equal to 1. E_w is the energy required to create a charge pair, values of which have been included for several relevant materials in Appendix A.

The number of primary ionising particles (N_{prim}) may then be calculated from the formula

$$N_{prim} = \frac{N_{sec}}{n_{sec}}. \tag{3.43}$$

where n_{sec} is the average number of secondary particles created within a detector, per primary particle. This experimentally determined value is specific to the type of primary particle and to the detector's set-up (size, volume of gas, type of gas, etc).

3.4 Signal-Voltage Relationship

From sections 3.2 and 3.3, it should now become clear that there is a signal dependence upon the magnitude of the electric field between the electrodes. This

may be appropriately represented graphically, as shown in figure 3.11. For curve (a), two parallel electrodes (infinitely large along the same plane) have a potential V between them. Filling the void between the electrodes is a gas with n_q charge pairs, liberated from the gas molecules by an ionising particle.

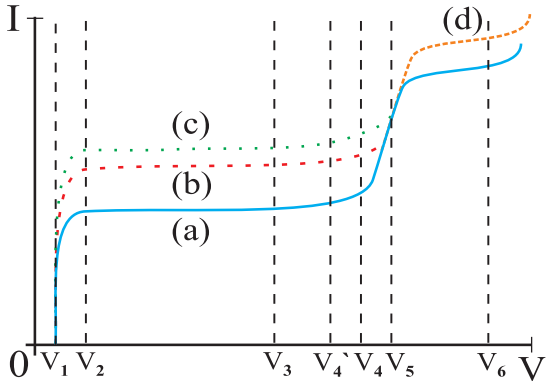

Figure 3.11: *Representation of the signal-voltage relationship.*

When V is very small ($V < V_1$) the field strength will not be strong enough to separate the produced charge pairs, therefore they will usually recombine[7]. There should be no signal within this region as no charges reach the electrodes (number arriving at plates, n_p, equals 0). Above the threshold of V_1 the charges begin to overcome natural attractive forces and inducing a signal on the plates, however some still recombine ($n_p < n_q$).

Between V_2 and V_3 recombination losses are negligible and all charges reach the plates ($n_p = n_q$). This plateau is called the 'ionisation chamber' region and it allows primary particle determination, as described in section 3.3.2, and characterisation. Above the point V_3, increases in the voltage will begin to provide the charges with sufficient energy to start creating charge pairs during collisions with other molecules, effectively causing an 'avalanche' within the gas ($n_p > n_q$). The signal begins to rise exponentially up to V_5, after which their is a small linear increase in the signal, followed by a logarithmic rise.

The avalanche affects between V_3 and V_4 allows the detection of low energy ionising particles, which do not have enough energy to be detected by ionisation chambers. This section of the graph is called the 'proportional counter' region, and it may be used for pure counting of particles or characterising them (such as measuring energy, as described earlier).

V_4 to V_5 is the region of 'limited proportionality' and is not an area commonly used in detector applications. Positive ion space charge affects inhibit the production of further avalanches causing the area to no longer be proportional

[7]It was found during the investigations that this was not always the case, [25]

and requiring a well stabilized power source to stop rapid increases of n by small increase of V.

Beyond V_5 is the 'Geiger counter' region which is used purely for the detection of particles. Here the collected charge pairs greatly outnumber the initial ones ($n_p \gg n_q$), thus allowing the counting of lightly ionising particles. The term counting specifically refers to a relative amount of ionising radiation and not the exact amount.

V_6 marks the end of the useful voltage scale, as any initial ionisation causes a continuous discharge within the chamber.

It is also of interest to note what occurs when either the initial amount of ionisation is increased, (c), or the chamber length is increased (b). For both conditions the ionisation chamber region remains the same, with only an increase in signal magnitude.

The Geiger counter region is independent of initial ionisations and therefore is unaffected by any increase, however a longer detector allows larger avalanches to propagate, producing an increased signal, (d).

The proportional counter region, on the other hand gives an increased signal for both a longer geometry and an increased initial ionisation. The latter, however, causes the region to come to an end sooner, due to increased avalanche density. This is shown by V_4', which is dependant on the initial ionisation size.

Summary

To summarise each detector region;

- ionisation chambers and proportional counters can be used to identify and characterise particles,
- proportional counters and Geiger counters may be used to detect and count lightly ionising particles,
- there is little or no saturation affects (problems caused by a very large amount of initial ionising particles) for ionisation chambers and Geiger counters, respectively. For ionisation chambers, any affects are noticed after the condition set by equation (3.29),
- all detector regions produce larger signals with longer geometries, provided the distance between the plates is constant.

Chapter 4

Beam Loss Monitor Prototypes for the LHC

Ionisation chambers are the proposed devices to be used in the beam loss monitoring system for the LHC. As discussed in the previous chapter, they can be used to determine the number of primary ionising particles entering the chamber (immediately discounting Geiger counters) and have good saturation properties (an advantage over proportional counters). The specifications for their operation in the LHC, as of 10^{th} January 2005, are stated as;

- 70% of the charge should be collected within 100μs (ie. one revolution of the LHC),
- the total volume of a chamber should be 1 litre,
- the chambers must be highly reliable,
- the mean time between failures should be 20 years,
- linear gain variations must be less than 20 %,
- dark current produced without charge must be less than 100 fA,
- chambers must stay within the ionisation chamber property region.

4.1 Chamber Designs

Currently, three type of ionisation chamber have been proposed for the LHC beam loss monitoring system. The parallel plate ionisation chamber, figure 4.1 (a), is currently in use as BLMs for the SPS and several other CERN accelerators. They consist of many alternating aluminium anodes and cathodes encased within a nitrogen filled stainless steel tube and have a very high reliability. Several small

Figure 4.1: *Prototype chamber designs, not to scale. Full design drawings for each chamber have been included in Appendix C*

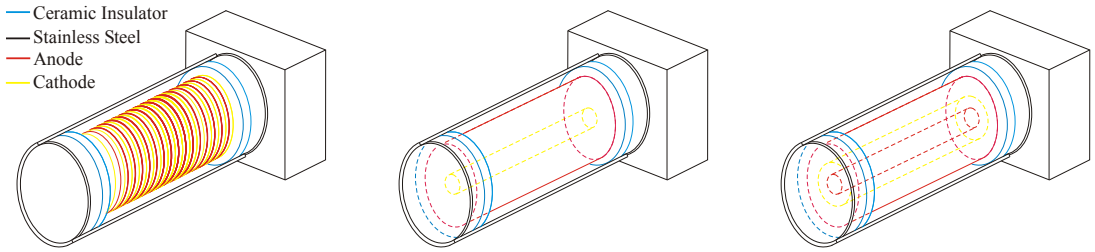

(a) *Parallel Plate Chamber.* (b) *2-Coaxial Chamber.* (c) *3-Coaxial Chamber.*

design alterations in the SPS chambers have been proposed for the prototype LHC parallel plate chambers.

The 2 and 3, coaxial ionisation chambers, figures 4.1(b) and 4.1(c), respectively, are prototype designs for the LHC beam loss monitoring system and are, as yet, not in use for such a job at CERN. They consist of 2 and 3 concentric aluminium electrode tubes, again encased within a stainless steel tube.

The voltage between the electrodes of all the prototype chambers has been selected to be 1500 V. The current SPS chambers run at approximately 800 V.

Design investigations must be carried out on all the prototype chambers to ensure that they are within the design specifications, and to determine which of the chambers is the most suitable for the LHC beam loss monitoring system.

4.2 Filling Gas Choices

The filling gas of the chambers has not yet been specified in the designs, but the choice should allow the chamber to operate within the specifications, discussed at the start of the chapter. Ideally this would mean that the gas has both a large rate of energy loss (so lots of ionisation will take place when particles pass through it) and a high mobility (so the particles produced may quickly be collected at the electrodes), while still remaining in the ionisation chamber property region (some gasses bring on the onset of the proportional counter region earlier than others).

In addition to this, it would be expected that the gas should have good radiation lifetime properties. Specifically, large gas mixtures (such as air) may produce unwanted impurities when exposed to ionising radiation, simply by the combination of foreign charged pairs. Pure gasses are less likely to be affected in this way as they cannot combine with anything other than an identical particle, or cannot combine easily with other particles (in the case of halogen gasses).

With these considerations, the following gases have been proposed for the LHC ionisation chambers:

Nitrogen - N_2

Pure nitrogen is the gas that is currently in use within the SPS ionisation chambers. It satisfies the conditions, mentioned above, well. A disadvantage to this gas comes when considering leaks within the detector.

Should a leak occur, and air enters the chamber, it would be very difficult to notice as both have similar properties (air is approximately 78% nitrogen). A way to combat this is to fill the chamber to a pressure greater the one atmosphere, as pressure increases cause a linear increase in signal[1] (below 10 ATM). Therefore the signal will be less for a chamber at 1 ATM (such as a chamber with a leak) than a chamber at pressures greater than 1 ATM.

Argon - Ar

Pure argon has a larger rate of energy loss than the nitrogen ($\{dE/dx\}_{min}$(Ar) = 2.79 keV/cm, $\{dE/dx\}_{min}(N_2)$ = 2.28 keV/cm) but has lower electron and ion drift velocities (see Appendix A). Therefore argon is likely to have a larger signal, but the ions will move slower.

Also, as a noble gas, argon allows the onset of the proportional counter region at lower fields than would be allowed in gases with more complex molecules[2] (N_2, for example). As stated this is an unwanted affect, should this occur near the operational region.

Argon 93%, Carbon-Dioxide 7%, Ar(93)CO_2(7)

This Ar-CO_2 mixture has approximately the same energy loss rate and ion velocity as the pure argon, but the addition of the CO_2 impurity will allow the electrons to move faster than in the pure argon gas.

The carbon-dioxide will also act as a quenching gas, inhibiting the onset of proportional counter region in the argon.

All three gases are both easy and cheap to acquire and fill. However, argon has the advantage of being used in one of the leak test procedures for the chambers.

[1] This relationship was noted by the work of Gianfranco Ferioli and presented internally at CERN.

[2] As described Gas Mixtures in Gaseous Detectors, [32].

4.3 Theoretical Field Magnitudes

From the geometry mentioned above, and the discussions of section 3.2.2, the theoretical field strengths of the three prototype chambers may be calculated.

Parallel Plate Chamber

In the parallel plate chamber each anode-cathode combination may be thought of as a separate pair of infinitely long electrodes (in the same plain, x) with a distance d between them (ie. $y = d$). With this in mind equation (3.27) becomes

$$V = \frac{q}{\varepsilon_0} \int_0^d \frac{dy}{x^2} = \frac{q}{\varepsilon_0} \frac{d}{x^2}$$

but as $E = q/\varepsilon_0 A$, where A is the surface area (x^2), from equation (3.26), this may be rearranged to

$$E = \frac{V}{d}, \tag{4.1}$$

and hence is constant for a given voltage and plate distance, which is expected for such a set up. This can be seen in figure 4.2, which has been plotted using LHC parallel plate chamber specifications ($V = 1500$ V and $d = 0.5$ cm).

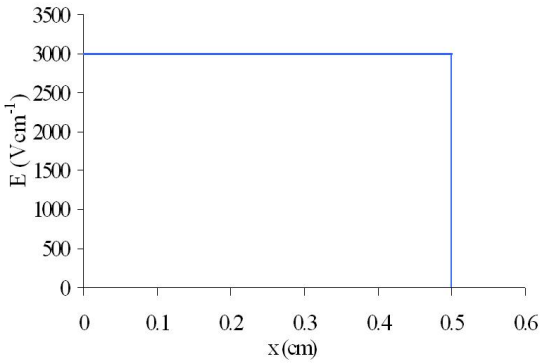

Figure 4.2: *Field magnitude as a function of position, in the LHC parallel plate ionisation chambers*

In reality this relationship is not totally accurate. As the plates are not infinitely long electrodes, field distortions will be created near to the edges, making the field between the plates non-uniform[3]. However, these affects cause only a slight deviation from the theory when near to the centre of the electrodes.

[3]Electrode edge field distortion affects have been discussed, for the case of an ionisation chamber, by R. Witkover & D. Gassner [23]

2-Coaxial Chamber

For the coaxial chambers the surface area is given by $A = 2\pi rL$, where r is the radius and L is the length of the tube. Therefore considering E as a function of the radial position ($s = r$) within two concentric cylinders of radius a and b (with $a < b$), equation (3.27) becomes

$$E = \frac{V}{\ln(b/a)r} \tag{4.2}$$

Using the 2-coax prototype configuration, where $a = 0.5$ cm, $b = 3.3$ cm and $V = 1500$ V, figure 4.3 can be plotted. From the graph, it is clear that for the 2-coax chamber, the field strength is dependant on the position within the field.

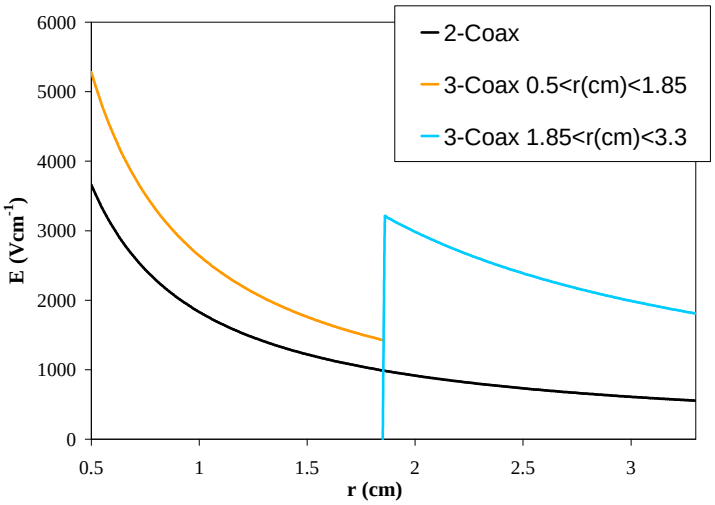

Figure 4.3: *Field magnitude as a function of radial position, in the LHC 2 & 3-Coaxial ionisation chambers*

3-Coaxial Chamber

The 3-coaxial chamber is treated in much the same way as the 2-coaxial, with the exception of the geometry. E is now considered as a function of the radial position within two sets of concentric cylinders of radius a, b and c (where $a < b < c$) and the voltages are given by V_{ba} and V_{cb}. Therefore equation (3.27) becomes

$$E_{ba} = \frac{V_{ba}}{r\ln(b/a)}, \quad E_{cb} = \frac{V_{cb}}{r\ln(c/b)} \tag{4.3}$$

which again may be plotted using the 3-coax prototype configuration, $a = 0.5$ cm, $b = 1.85$ cm, $c = 3.3$ cm and $V_{ba} = V_{cb} = 1500$ V (figure 4.3).

4.4 Chamber Space Charge Effects

It is now possible to calculate the charge density levels that will begin to contribute to the electric field of the chamber.

Parallel Plate Chamber

Under the consideration that the field should remain constant within the parallel plate chamber, equation (3.29) becomes

$$\int_0^d n\, dx \;\ll\; \frac{\varepsilon_0}{e}\int d\mathbf{E} \tag{4.4}$$

$$\Rightarrow n \;\ll\; \frac{\varepsilon_0}{e}\frac{V}{d^2}. \tag{4.5}$$

Therefore, considering the geometry and setup mentioned in previous sections, space charge affects begin to distort the field as $n \rightarrow 3.3 \times 10^{11}$ elementary charge pairs per cm^{-3} per plate pair. For the LHC, which will accelerate bunches each comprised of up to 10^{11} particles, of which only a very small fraction of particles should be lost from the beam, it should be highly unlikely that this charge density should be reached and hence little or no space charge affects should be observed within these chambers. .

2-Coaxial Chamber

The combination of equations (3.29) and (4.2) produces an equation for the space charge density criteria in a coaxial chamber, which may be expressed as

$$\int_a^b n\, dr \;\ll\; \frac{\varepsilon_0}{e}\int d\mathbf{E} \tag{4.6}$$

$$\Rightarrow n \;\ll\; \frac{\varepsilon_0}{e}\frac{V}{r(b-a)\ln(b/a)}. \tag{4.7}$$

By inserting the relevant geometry, this equation may be represented graphically, as shown in figure 4.4. This shows that the charge density may be larger near to the centre of the chamber, a plausible idea when considering that this is the area of largest field and hence would require more charge to alter it.

3-Coaxial Chamber

The criterion for the space charge density within the 3-Coaxial chamber may be calculated in much the same way as the 2-Coaxial, with the expressions given

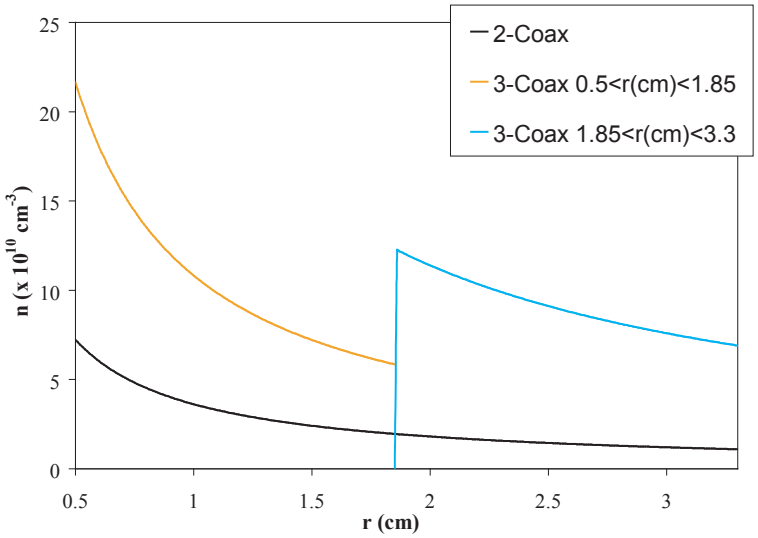

Figure 4.4: *Space charge density as a function of radial position within the LHC 2 & 3-Coaxial ionisation chambers*

as

$$n_{ba} \ll \frac{\varepsilon_0}{e} \frac{V}{r(b-a)\ln(b/a)}, \tag{4.8}$$

$$n_{cb} \ll \frac{\varepsilon_0}{e} \frac{V}{r(c-b)\ln(c/b)}. \tag{4.9}$$

These have also been plotted in figure 4.4, and show that higher charge density is allowed within the 3-coaxial chambers, compared to the 2-Coax.

4.5 Detector Electronics

In order to obtain and record the induced signals within the ionisation chambers, the devices must be connected to some sort read-out electronics. Several variations of equipment may be used for this task, but the majority of experiments conducted for this investigation used a common setup, which is also used within the SPS ionisation chamber readout system. This section briefly discusses the electronic equipment that is used in conjunction with the beam loss monitors at CERN.

Low Pass Filter

Low pass filters are built directly onto all ionisation chambers used for beam loss monitoring. Figure 4.5 shows that they are simply a capacitor and a resistor,

and hence should not be affected greatly by high radiation levels [24]. The low

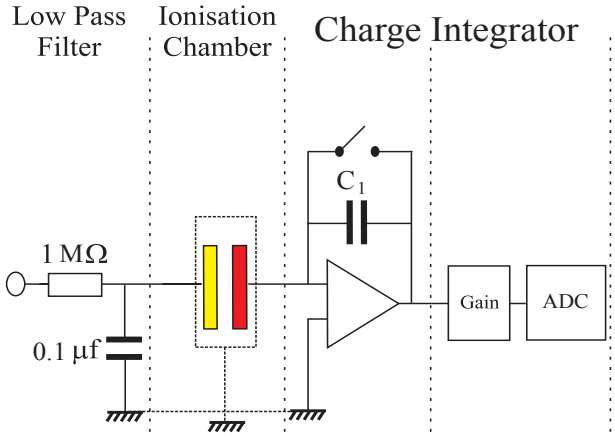

Figure 4.5: *Standard read-out electronic circuit.*

pass filter principally acts as a charge "reservoir". Should a fast large beam loss occur the charge is extracted from the charged local capacitor rather than the power source, which may be over a kilometre away. This allows a quick signal rise time within the detector. The filter also helps protect against high voltage variations in the power supply.

Charge Integrator

The charge integrator is where each signal pulse is recorded, summed over a set period of time, digitalised and stored in memory. The simplified electronic layout is shown in figure 4.5. The signal produced within the chamber may therefore be calculated from voltage recorded over the analogue to digital converter (ADC).

$$\begin{aligned} V_{ADC} = G\frac{Q}{C} &= G\frac{IT}{C} \\ \Rightarrow I &= CV_{ADC}\frac{1}{GT} \end{aligned} \tag{4.10}$$

where, quite simply, the current (I) is the total charge recorded (Q) in the time period of collection (T). The total charge collected is represented by V_{ADC}, the operational amplifier capacitor (C_1) and the chosen gain on the signal (G). This type of circuit is a simple signal integration circuit and may be found in most literature[4].

[4] An example may be found [20] as well as references to other publications.

Chapter 5

Particle Interactions with Ionisation Chambers

It has already been discussed that particles will always be lost from the beams of accelerators, resulting in interactions with the machine's walls. When these interactions occur energy will be deposited within the walls, as a function of the distance through which the particle has travelled (as shown in section 3.1.1). Should this deposited energy be sufficient enough, particles may be produced and liberated. In turn, these created particles may interact with the wall, producing further particles. The overall affect is a shower of secondary particles being emitted from the point of initial impact upon the wall.

Secondary showers provide a wider surface area of detection than a single lost particle, due to an avalanche effect during propagation. It is therefore much easier to detect the shower which a lost particle creates, rather than the particle itself. This added to the fact that it is extremely impractical to place the detectors within the LHC machine itself, the BLMs are installed externally and are primarily designed to detect the produced secondary showers, which can be back-calculated to the number of initial particles lost, by statistical methods.

In order to assess the ionisation chamber's effectiveness at detecting the secondary showers, the signal produced within the chambers must be known for the shower's dynamic range of the particles and energies. However, it is costly, time consuming, and in certain instances extremely impractical to perform experiments to explore, what is potentially, a large variety of variables. For this reason it was proposed that a series of simulations should be conducted using the hadronic shower code *Geant 4* (*G4*).

Further to this, the code was used to simulate how the amplitude of the signal changes with the position of the impacting particles on the ionisation chambers. This data was subsequently compared against the results of similar experiments, which were conducted within a SPS extraction line, so as to determine the codes accuracy

5.1 *Geant 4* ionisation chamber program

The premise of the program was to measure the energy deposited in a volume of matter (called the sensitive detector) by a particle impacting upon the ionisation chambers, and the secondary particles which it creates via matter interactions. This full process was classified as an 'event' and for most of the simulations run, each event was conducted 10000 times (this proved to give a good ratio between statistics and program calculation time).

The program included the full list of 'ordinary' physics processes and particles that were currently available to *G4*[1], so as to give a more general purpose simulation. The geometry of the chambers ,within the program, was represented as a simplified version of the proposed chambers mentioned in section 4.1 and can be shown Appendix B. It should also be noted that no fields were simulated within the program.

For each of the chamber designs the sensitive detector has been considered as the material (usually a gas) in and around the electrodes. The relevant properties for some of the sensitive detector and chamber design, materials has been included in Appendix A.

5.1.1 Stopping Power Simulations

As a preliminary check of the programs ability to measure the energy deposited within a material, simulations were conducted to measure the rate of energy loss (dE/dx) for protons, with a momentum p, passing through a slab of helium gas, of thickness x. This data was then compared against the analytical and experimental values, previously shown in figure 3.2.

The figure clearly shows, for momenta lower than 10 GeV/c, that the simulated data and the literature data closely match. A difference in the data arises for larger momenta, suggesting a variation in the density affect coefficients of the two models. At momenta larger than 1000 GeV/c, the simulation begins show a large increase in the rate of energy loss. This represents the onset of the radiative loss part of the stopping power spectrum, which commences earlier than that predicted within the literature data. This would suggest either this process was not considered within the literature calculations, or the density affect (already established as being different) alters the point at which radiative losses occur.

To better measure the codes capabilities it would be suggested to directly compare the results against experimental data of a similar scale. However, the comparison between the minimum rate of energy loss for the simulation and published data [2] shows a very good agreement, with an error of only 0.1%.

It should be considered that the *G4* program, written for these tests, is quick and effective method of determining the energy deposited within a material.

[1] This physics list can be viewed within the ExampleNO4 program of [28]

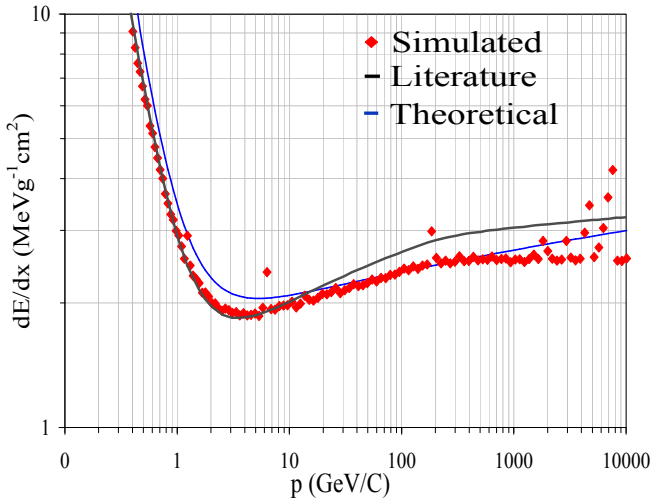

Figure 5.1: *Rate of energy loss for protons passing through helium gas. Simulated data was taken from the* G4 *code. Theoretical and literature data were taken from previous figure 3.2.*

5.2 Beam Scan Investigations

The discussions of section 3.1.1, should make it clear that the amount of energy deposited within a material is dependant on, not only, the paritcle's type and momentum, but also the distance it travels through a specific material. It would therefore be reasonable to assume that the signal produced within a chamber, will be dependant on the filling gas of the detector and on the particle's impact position with the chamber, as some trajectories may be longer or contain more matter than others.

It is, however, undesirable to have large fluctuations of the signal within the detectors, as mentioned in Chapter 4. For this reason a number of simulations and experiments were carried out in order to investigate the ionisation chamber's signal response to the type of filling gas and the initial ionising particle's impact position. These tests would also act as a direct method of determining the *G4* program's capabilities, by comparing the simulation results against experimental data. This was conducted, in general, by scanning a beam over ionisation chambers filled with various gases.

5.2.1 Simulations

These simulations were conducted with the *G4* program mentioned in section 5.1, on the simplified chamber geometries shown in Appendix B.

The program was edited so that one event represented the combined interactions of one proton, with a kinetic energy of 400 GeV, launched from

an initial position x, in the direction y so that it impacted perpendicular to the z plain. After each run of 10000 events the initial launching position was changed to $x + dx$ and the program was run again. The overall affect was a beam scan along a plane of the chamber.

The orientation of the chamber dictated where exactly the protons impacted. The main orientation considered was that of the longitudinal axis being in the z plane, as shown in figure 5.2(a). However, the beam scan simulation affects of the longitudinal axis being in the x and y plane, shown in figure 5.2(b) and 5.2(c) respectively, were also simulated.

The simulations were carried out on all the chamber designs, and with a selection of sensitive detector materials, namely the filling gases mentioned in section 4.2 (at 20^{o}C and 1 ATM).

Figure 5.2: *Simulated beam scan setup, where the impact is perpendicular to the z plane*

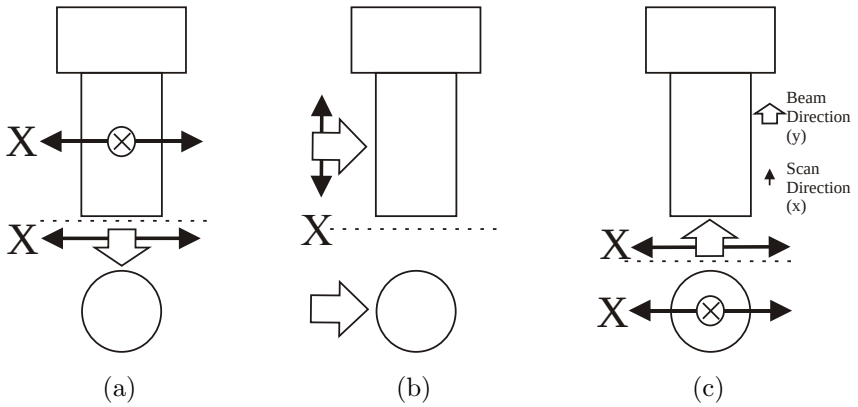

5.2.2 Experiments

These experiments were carried out within the T2 experimental area of the SPS accelerator. The chambers were installed on a remotely controlled sliding table, which in turn was situated by an open air section of the accelerator (effectively a small gap in the machine), as shown in the figure 5.3. When the machine was operational, the chambers would be scanned through the beam and the signal that was produced by the impact of a particle bunch would be recorded at each position, using the standard electronics.

Due to the size of the gap and the orientation of the sliding table, only the signal response for the transverse impact upon the chambers could be recorded. This experimental set-up is shown in figure 5.3, with the voltage of the chambers being set at 1500 V. The environment each chamber was exposed to during these tests has been summarised in table 5.1.

Figure 5.3: *Beam scan SPS extraction line experimental set-up.*

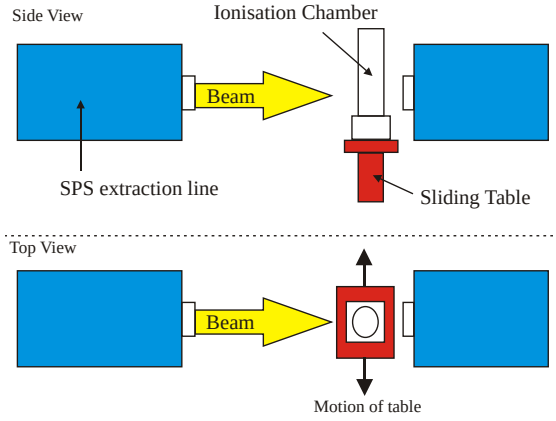

(a) *Diagram of SPS beam scan experiment.*

(b) *Picture of ionisation chamber on the sliding table at the 'air gap' in the SPS extraction line.*

	Parallel Plate Chamber	2-Coaxial Chamber	3-Coaxial Chamber
Beam Particle Type	Protons	Protons	Protons
Beam Energy (GeV)	400	400	400
Beam Size (cm), 4 σ			
Vertical	0.6	1.2	1.2
Horizontal	0.5	1.0	1.0
Number of Particles ($\times 10^{11}$)	30.0±0.1	36.1±0.1	35.0±0.1
Filling Gas	N_2	Ar	$ArCO_2$
Gas Pressure (atm)	1.1	1.0	1.0

Table 5.1: *Experimental beam scan values.*

Unfortunately, at the time of these experiments there were insufficient prototype chambers for beam scan investigations of the filling gas (which were simulated, section 5.2.1). Also the process of gas removal and refilling was extremely time consuming and difficult, making it an unpractical option due to the limited experimental period that was available.

5.2.3 Results and Analysis

The results of the beam scan simulations on the parallel plate ionisation chambers, mentioned in section 5.2.1, are shown in the figure 5.4. The simulations have been

superimposed on the experimental beam scan results, as mentioned in section 5.2.2 and compared to the geometric layout of the chamber. The simulations[2]

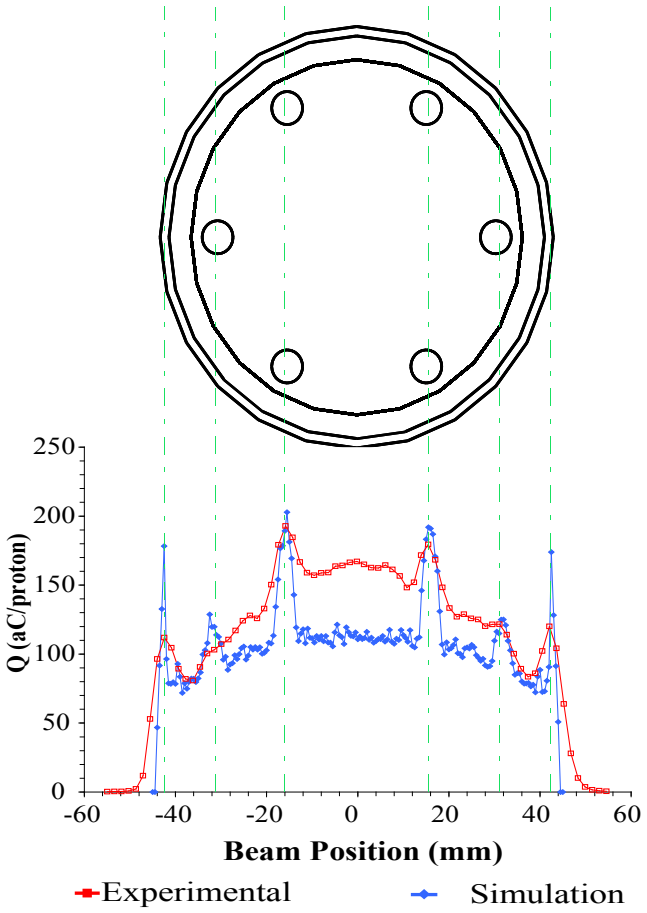

Figure 5.4: *The results of the simulation and experimental beam scan tests on a nitrogen filled parallel plate chamber. These have been compared against the geometry of the chamber. The experimental results have been horizontally scaled, to the first peak, due to differences in the measuring scale. There has been no vertical scaling.*

and experiments clearly show that the signal depends on the position where the beam impacts upon the chamber. When the beam impacts upon an edge of a chamber the signal is considerably smaller than when it hits the centre. This would therefore suggest that the signal will be largest for particles that remain in the chamber for a longer period of time (ie. particles that have a long trajectory

[2]Only the simulations for the transverse impacts upon the chambers have been shown, due this disertations spatial constraints. The other orientations showed similar patterns to those presented, [26].

path).

These results also show that when the beam passes through a support rod the signal is increased. The reason for this is because the rod material has a higher energy loss rate than that of the gas ($\{dE_n/dx\}_{min}(\mathrm{Al}) = 4.46$ MeV/cm, $\{dE_n/dx\}_{min}(\mathrm{N_2}) = 2.28 \times 10^{-3}$ MeV/cm), allowing more energy to be deposited within the rods and hence creating a large amount secondary ionising particles. These secondaries will then deposit a greater amount of energy within the gas than the original beam because they will have a considerably lower momentum (see figure 3.1).

The experimental results show some noticeable differences to the simulated data. The overall signal is larger, except at points where the beam impacts upon the rods. The experimental data also produces wider signal peaks at these points. Both of these observations can be explained from the fact that the simulations used an infinitely small point charge particle beam and the experiments used a finite size beam.

A scanned finite sized beam would therefore impact upon more matter, hence producing a wider signal peak. It would also increase the chances of the beam hitting both the gas and an electrode simultaneously, causing an affect similar to the beam passing through the rods (ie. an increase in signal due to the larger energy loss rate of the plate material) and is an explanation to the generally higher signals.

Figure 5.5 shows the beam scan simulation plot for the 2-coaxial and 3-coaxial ionisation chamber. This has again been superimposed over the experimental beam scan results and compared against the geometry. It should be noted, however, that there was insufficient experimental data for the 3-coaxial chamber to plot on the graph due to test complications (which will be mentioned later).

A similar relationship to the parallel plate chambers was found, with wide and high signal peaks being found on the coaxial electrodes (where there is more material with a higher rate of energy loss). However, there remains a striking difference between the results. The overall experimental signal is lower than the simulated (approximately 30% at the mid-point between electrodes), especially when the beam approaches the inner electrode.

An explanation of this is due to there being no field within the inner electrode of the chamber, hence any charge pairs created in this region will not produce a signal. Therefore, when the beam (or part of the beam) enters this region there will be a reduced contribution to the signal. The *G4* program, on the other hand, registers all energy deposited within the gas, including the inner electrode region.

A direct method of measuring the *G4* program's accuracy is to compare the total integrated charge per proton for both the simulated and experimental results. This has been shown in figure 5.6. The percentage difference between the two types of data is ± 35% for both the parallel and 2-Coaxial. This percentage difference is most likely larger than reality as the position increments, used in determining the integrated charge, were considerably larger for the experiments

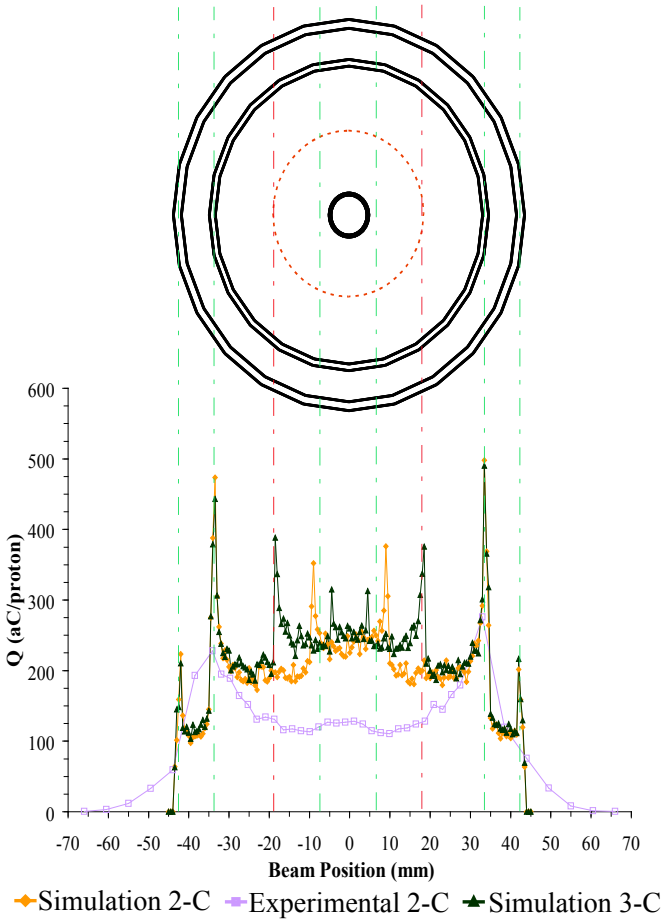

Figure 5.5: *The results of the simulation and experimental beam scan tests on argon filled 2 & 3-Coaxial Chambers. These have been compared against the geometry of the chambers. The experimental results have been horizontally scaled, to the first peak, due to differences in the measuring scale. There has been no vertical scaling. No experimental results have been shown for the 3-Coaxial chamber due to experimental complications. The small difference between the position of the inner electode comes from an error in the geometry input, which makes little affect to the overall result.*

than the simulations (2mm and 0.5mm increments, respectively). However, this common factor provides an estimated error within the simulation program.

The experimental and simulated data presented figure 5.6 also shows that the 2-Coaxial chamber provides a greater total integrated charge per proton than the parallel. This is due to the beam interacting with more matter in the 2-Coaxial (the metal electrodes) than the parallel, and hence creating larger amounts of ionising secondaries.

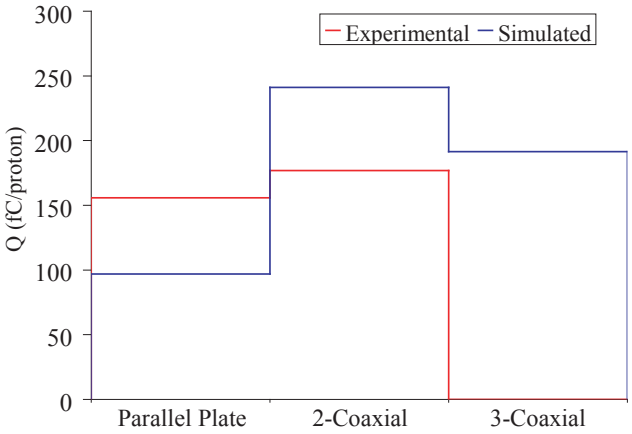

Figure 5.6: *Total experimental and simulated integrated charge of each chamber, for the beam scan scenario.*

As the simulations give a fairly good representation of the experiments, it is possible to analyse the effectiveness of each of the chamber types from the figure 5.7. The simulated parallel plate chamber seems to give an overall lower signal than the coaxial chambers. The simulated 3-Coaxial and 2-Coaxial chambers give much the same signal until the beam passes the middle electrode of the 3-Coax. At this point the chamber produces a larger signal (as the beam must pass through more dense matter, ie. the aluminium electrodes), hence has providing a greater overall simulated signal for the 3-Coaxial chamber.

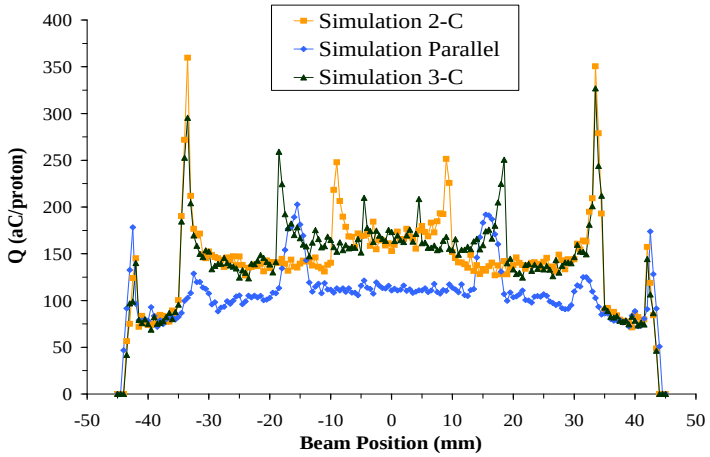

Figure 5.7: *Simulated signal response (in charge per proton) of the nitrogen filled parallel plate chamber and the 2 & 3-Coaxial chambers.*

In reality however, the 3-Coaxial chamber caused the beam to be regularly dumped. Similarly, occasional dumps occurred when the beam passed the edges of the electrodes in the 2-Coaxial chamber (the signal peak points), where as there were no such problems with the parallel plate chamber.

These dumps were caused by an increased amount of secondary particles being produced due to the chambers (as would be expected due to the beam interacting with more matter as it transverses more metal electrodes). These secondaries were observed by symmetry detectors, already installed near the test point, and caused them to dump the beam.

It may also be noted from both figure 5.7, and the experimental results of figures 5.4 and 5.5, that the parallel plate chamber produces the most homogenous signal response to ionising particles. This means that the fluctuations (σ) of the signal are lower for the parallel plate chamber than the coaxial chambers ($\sigma = 31$ & 51 aC/proton for the simulations, respectively, & $\sigma = 56$ & 63 aC/proton for the experiments conducted on the parallel plate chamber and the 2-Coaxial chamber, respectively).

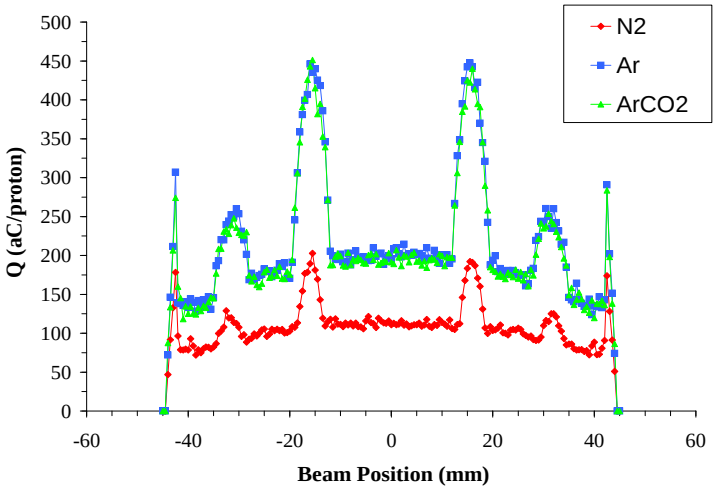

Figure 5.8: *Simulated signal response (in charge per proton) of the parallel plate chamber, filled with either nitrogen, argon or argon(93%)carbon-dioxide(7%) gas.*

The simulated affect of altering the filling gas of the parallel plate chamber has been shown in figure 5.8. Clearly by using argon instead of nitrogen the magnitude of the signal is increased (1.77 times, on average). This is not an unexpected pattern as argon has a larger rate of energy loss than nitrogen ($\{dE/dx\}_{min}$(Ar) = 2.79 keV/cm, $\{dE/dx\}_{min}(N_2)$ = 2.28 keV/cm). and hence would be expected to have more energy deposited within it.

The argon carbon dioxide mixture produces near identical results to that of the pure argon, again a logical result due to the argon having a considerably

larger concentration than the carbon-dioxide within the mixture (93% Ar to 7% CO_2). An identical response is found when the gases are changed within the 2 & 3-Coaxial chambers.

5.2.4 Error Analysis

As the simulations were conducted 10000 times for each point, the fluctuations in the values can be considered negligible. The only other source of error for the simulations comes from the conversion from energy to charge, primarily the $E_w \pm 0.1eV$. However, this produces only very small fluctuations and hence the error in the simulated values has not been plotted.

Errors in the experimental values come mainly from signal fluctuations in repeated readings and the accuracy of determining the number of particles within the beam. The relative error in the average signal for one position, taken from the fluctuations around the mean, was taken as 0.02.

The error in the determination of the number of particles within the beam was given as $\pm 0.1 \times 10^{11}$. The combination of these meant that the expected error in the signal (at a maximum point, ie. the place where the relative error causes the largest fluctuation) is approximately 0.7 aC/proton, again too small to plot on the graphs.

5.2.5 Conclusion

The experiments and simulations discussed within this section, show that the *G4* ionisation chamber simulation code provides a good model of the particle interaction processes which occur within the detectors. The percentage difference in the total integrated charge between the simulated and experimental data was determined to be $\pm 35\%$.

It should also be clear that the largest signals are produced by particles with the longest path through the chambers. This is highlighted within the parallel plate chambers, which generally produce lower signals than the coaxial chambers.

The parallel plate chambers have be shown to have the most homogeneous signal response to an impacting particle, with the fluctuations being shown to be $\sigma = 31$ & 51 aC/proton for simulated parallel plate chambers and coaxial chambers, respectively, and $\sigma = 56$ & 63 aC/proton for the experiments conducted on the parallel plate chambers and the 2-Coaxial chambers, respectively.

Finally, it has been shown that gases with high rates of energy loss will provide larger signals within the chamber, with argon giving a signal approximately 1.77 times that of nitrogen.

5.2.6 Further Suggestions

Should this topic be further investigated, it would be suggested that more experiments be conducted to see how the different orientations of the detectors affect the signal. Specifically measurements should be made with the coax chambers as it may be found that at other angles of beam impact may result in a greater amount of secondaries.

It would also be suggested that the beam scan experiments be conducted on a chamber that may be refilled with other gases, so as to compare against the simulation results found in section 5.2.3. Further to this more points should be taken to identify the simulations accuracy.

Finally, it may be of interest to repeat the simulations with the addition of the relevant fields, namely the electric field between the electrodes. This may bring the data closer to that found in the experiments.

5.3 Secondary Shower Interactions

The collisions with the accelerators walls, of the highly energetic particles, lost from a beam bunch, will most likely produce a secondary shower that is comprised of a wide selection of particles, with each type having a range of energies. The discussions of section 3.1 would therefore suggest that each of these shower constituents will interact with the ionisation chambers differently, and hence produce different signals. However, the premise of the BLM detectors is to produce a specific signal response per lost proton, effectively the sum of the signal responses for the constituent shower particles weighted against their distribution.

It is therefore crucial that the signal response of the chambers is known for each of the shower's constituent particles, at their dynamic range of energies, so that effectiveness of the protection system may be known. For this reason a series of simulations were carried out to investigate these effects.

5.3.1 Secondary Shower Production Simulations

Unfortunately, as the LHC is not yet operational, it is very difficult to specifically know the type of particles, and their range of energies, that are produced due to a particle-wall interaction. For this reason simulations were conducted by Dr. Laurette Ponce (using the *Geant 3.21* hadronic shower code) to list the particles produced, and the range of energies involved, due to particle-wall interactions at predicted loss points along the LHC accelerator system. The program was run for both the injection energy beam (450 GeV) and the maximum energy beam (7 TeV).

The simulated spread of particles and energies for the 450 GeV and 7 TeV beams, are shown in figure 5.9(a) and figure 5.9(b) respectively. Table 5.2 lists the

most abundant particles produced (along with their particle number reference, for the graphs) and the range of energies expected.

		Secondary Particle Energies			
Particle Number	Particle Type	450 GeV		7 TeV	
		Max (GeV)	Min (GeV)	Max (GeV)	Min (GeV)
1	Gamma	0.03	0.01	0.80	0.33
2	Positron	0.16	0.01	0.80	0.35
3	Electron	0.12	0.01	0.80	0.35
4	Neutrino	0.10	0.04	0.60	0.20
5	$Muon^+$	0.30	0.04	1.00	0.60
6	$Muon^-$	0.30	0.04	1.00	0.60
7	$Pion^0$	-	-	-	-
8	$Pion^+$	1.00	0.04	5.00	2.00
9	$Pion^-$	1.00	0.04	5.00	2.00
10	$Kaon^0$ long	-	-	-	-
11	$Kaon^+$	-	-	-	-
12	$Kaon^-$	-	-	-	-
13	Neutron	0.60	0.08	3.00	1.80
14	Proton	0.60	0.08	3.00	1.80

Table 5.2: *The beam loss particle spectrums for the LHC. Values have been recorded for injection and extraction energies (450 GeV & 7 TeV). Only the most abundant particles have been listed, as these significantly contribute to the signal. The number of these particles decays exponentially with total energy.*

5.3.2 Secondary Shower Interaction Simulations

In the previous section, the secondary shower spectrum of particles and energies was identified for predicted loss areas in the LHC accelerator. Clearly it would be extremely difficult to conduct experiments to investigate all these variables, as well as being time consuming. Hence, the *G4* ionisation simulation program (mentioned in section 5.1) was used to investigate the interactions.

These simulated tests were conducted so that one event represented the combined interactions of a particle, with a specific kinetic energy, being launched towards an ionisation chamber. The particle type and energy was dictated by the results obtained in section 5.3.1. These simulations were carried out on all chamber designs, with either Nitrogen, Argon or Argon Carbon-Dioxide being the filling gas.

The position, and direction, of impact upon the chambers was dependant on the type of chamber used within the simulation. The particles were fired towards the 2 & 3-coaxial chambers so that they would pass through the largest amount of

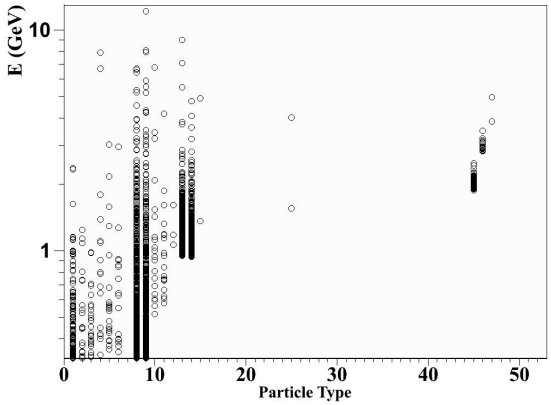

(a) *450GeV*

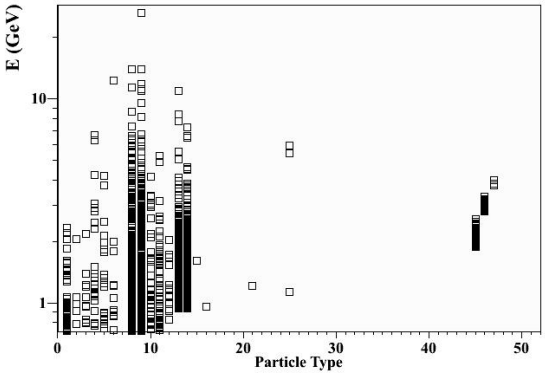

(b) *7TeV*

Figure 5.9: *The simulated total energy of the secondary shower particles from a 450 GeV and 7 TeV LHC beam, courtesy of Dr. L. Ponce. Particle type is the particle number.*

the chamber (shown in figure 5.10(a)), and so give the maximum signal response. The set-up was similar for the parallel chamber, but the stainless steel support rods provided an additional problem for considering the impact position of the particles.

The results of section 5.2 show that 15% of the total signal is contributed from the impact of a particle upon a rod. Couple this with the possible orientations to which the particle can impact with the chamber (hitting no rods, one rod, etc), a 20% rod interaction factor is introduced. In order to simulate this consideration, the program was written so that the particles would impact upon the chamber at a "non-rod" point 40000 times and at a "rod point" 10000 times (as shown in figure 5.10(b)). The total energy deposited within the parallel plate chamber, for

both impact positions, was then averaged over 50000 events.

Figure 5.10: *Simulated chamber designs and beam trajectory.*

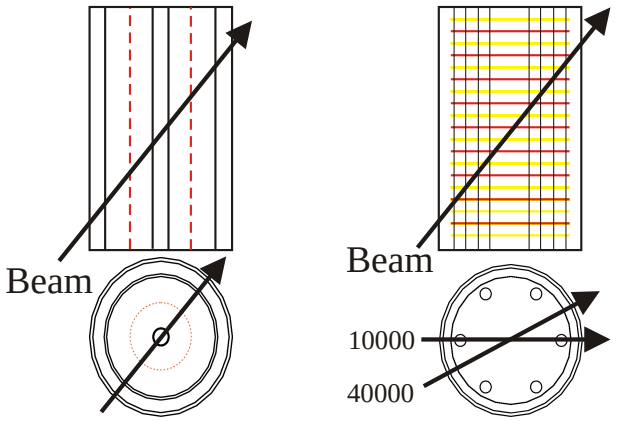

(a) *Coaxial ionisation chambers*

(b) *Parallel ionisation chambers*

5.3.3 Results and Analysis

The results for the energy range simulations upon the nitrogen filled ionisation chambers have been shown in figure 5.11. The graphs clearly show that the higher energy particles, unsurprisingly, deposit the most energy within the chambers. An exception to this is the neutrinos, which do not deposit any energy at all.

The graphs show that the signal within the 2 & 3-Coaxial chambers is almost identical for all energy ranges. Further to this the graphs also highlight that the coaxial chambers provide a larger signal than the parallel, a conclusion complemented by the results discussed within section 5.2.

An exception to this is for the very low energy range (the low energies of the 450 GeV spectrum), where it can be seen that the parallel plate provides a larger signal. This occurs because the coaxial chamber's extra matter begins to absorb the lower energy particles, rather than create the secondary showers that were present at higher energies. Overall, this means the parallel plate chamber is more sensitive to lower energies and the coaxial is more sensitive to higher energies.

By considering the total integrated charge of the spectrum (hence the signal that is produced per lost beam proton) the differences between each detector may be emphasized. Table 5.3 shows that the 2-Coaxial chamber produces a signal larger than the 3-Coaxial at the 450 GeV range (by only 4%), while the reverse affect is observed at the 7 TeV range (by only 1%). The parallel plate chambers have a 35% lower signal than the coaxial chambers at the high end of the 450

Figure 5.11: *Simulated signal response of the prototype chambers for the 450 GeV and 7 TeV particle spectrums.*

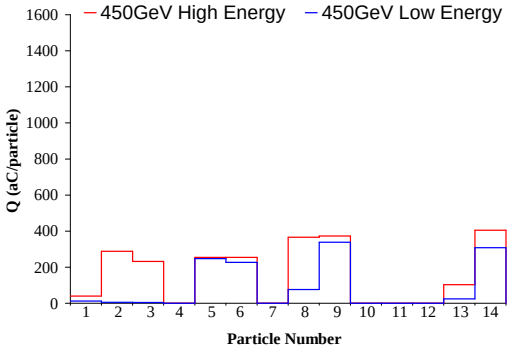

(a) *Parallel Plate - 450 GeV*

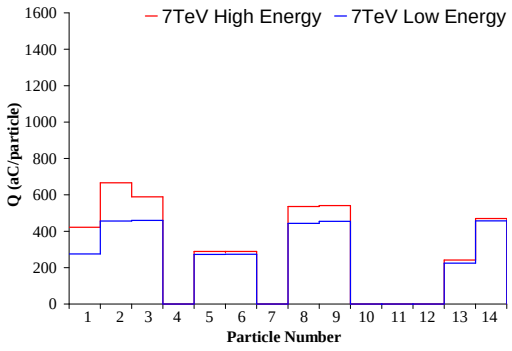

(b) *Parallel Plate - 7 TeV*

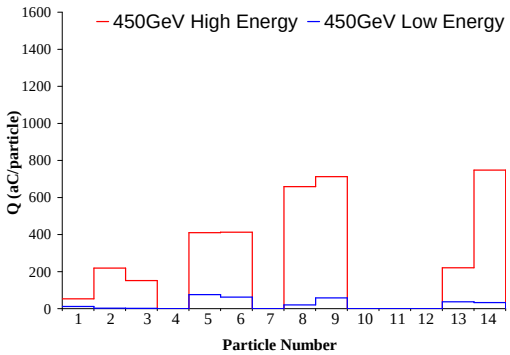

(c) *2-Coaxial - 450 GeV*

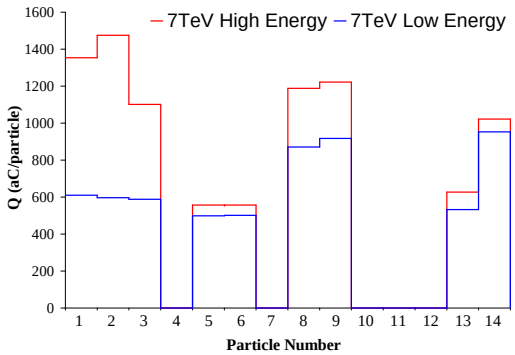

(d) *2-Coaxial - 7 TeV*

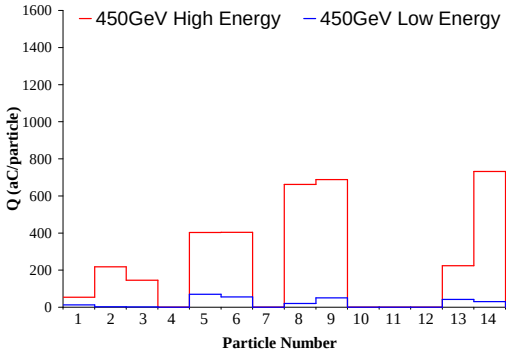

(e) *3-Coaxial - 450 GeV*

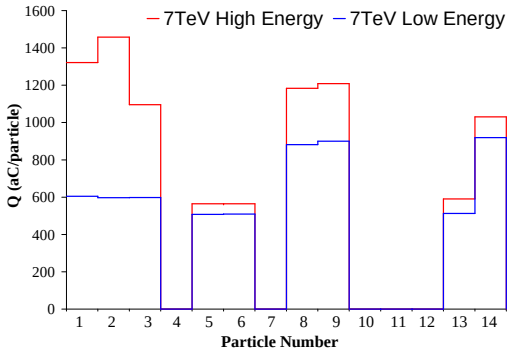

(f) *3-Coaxial - 7 TeV*

GeV spectrum, and a 75% larger signal for the lower end. The 7 TeV spectrum gives a 66% lower signal for the parallel detectors.

	Integrated Charge (fC/proton)			
	450 GeV		7 TeV	
Chamber Type	Max	Min	Max	Min
Parallel Plate (N_2)	2.32	1.24	4.04	3.32
Parallel Plate (Ar)	-	-	7.18	5.89
Parallel Plate (Ar(93)CO2(7))	-	-	7.08	5.89
2 Coaxial (N_2)	3.59	0.30	9.02	6.03
3 Coaxial (N_2)	3.53	0.28	9.10	6.07

Table 5.3: *Table of total simulated integrated charge, per lost beam proton.*

Figure 5.12 shows the signals produced when the 7 TeV particle spectrum interacts with a parallel plate chamber, of varying filling gas types (Nitrogen, Argon or Argon Carbon-Dioxide). The results are similar to those found in section 5.2.3, being that the gases with the higher rate of energy loss produce higher signals, ie. Argon has a signal 1.78 times as large as Nitrogen. This constant factor suggests that the signal is proportional to the rate of energy loss of the filling gas type.

Figure 5.12: *Simulated signal response of the parallel plate chamber, with different filling gases, for the 7 TeV particle spectrum.*

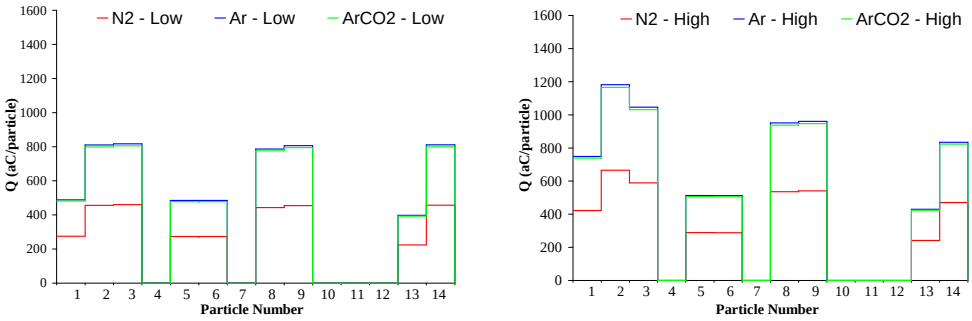

(a) *Low end of energy spectrum.* (b) *High end of energy spectrum.*

It is also possible to see that the pure Argon allows slightly larger signals than the Argon Carbon-Dioxide mixture (by approximately 2%, from table 5.3).

5.3.4 Error Analysis

As the simulations were conducted between 10000 and 50000 times for each particle type and energy, the fluctuations in the values can be considered negligible. The only other source of error for the simulations comes from the conversion from energy to charge, primarily the $E_w \pm 0.1eV$. However, this again produces only negligible values.

In the previous section,5.2, the percentage error between simulated and experimental values was obtained, $\pm$ 35%. This factor should be considered when applying these results to real situations.

5.3.5 Conclusion

The secondary particle shower interaction simulations, disscused within this section, have shown that the most energetic particles are expected to provide the largest signals within the chambers.

It has also been shown that the coaxial chambers are expected to provide the largest signal over for most spectrums (by between 35% and 66%), with the parallel plate chamber only providing higher signals at very low energies (by 75%).

This section has also presented the total integrated charge produced within each chamber, per proton lost from the LHC beam bunches, values of which have been given in table 5.3.

Finally, it has been shown that gases with high rates of energy loss will provide larger signals within the chamber, with argon giving a signal approximately 1.78 times that of nitrogen. This result is complemented by the data of section 5.2, which provides a similar result.

5.3.6 Further Suggestions

The simulations documented within this section provide a comprehensive investigation into the dynamic beam loss spectrum interactions with the ionisation chambers. The only main suggestions for an expansion to these tests could be an experimental confirmation of the results.

It has already been discussed that such experiments would be both time consuming and difficult, but C. Theis *et al.* ([21] & [22]) documents a similar detector investigation, with experimental evidence, that may be useful should this be attempted.

A further suggestion to this, would be to conduct the simulations with the relevant fields in place (namely the electric field) so as to more accurately represent reality.

Chapter 6

Signal Responce

It has been discussed, within Chapter 4, that the LHC beam loss monitors must collect at least 70% of the total charge created due to ionisation, in 100 μs (one revolution of the LHC). This factor allows quick large losses to be safely dumped before any machine damage occurs.

In order to assess the prototype ionisation chamber's effectiveness within the LHC, the signal response of each chamber type must be known. Similarly, the signal response for each potential filling gas must be examined, so that the gas which produces the largest signal within the shortest time may be used. In order to investigate these factors a number of simulations and experiments were conducted.

6.1 Theoretical Signals

The theoretical form of the signals produced within the chambers may calculated from the discussions of Chapter 3 and geometry mentioned in Chapter 4.

6.1.1 Parallel Plate Chambers

The parallel plate chamber has been considered to be two infinitely long electrodes, therefore electrode edge effects may be ignored. The charge pairs that are created within the chamber, are assumed to have no initial velocity ($v_0 = 0$) and no space charge affects between them.

Acceleration Time

The time taken for the electrons and ions to reach their respective drift velocities may be calculated from equation (3.22),

$$\mathbf{a} = \frac{q\mathbf{E}}{m_0},$$

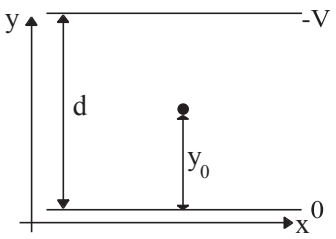

Figure 6.1: *Theoretical parallel plate set-up.*

where q and m_0 are the charge magnitude and the rest mass, respectively, for each of the liberated charged particles. **E** is the electric field strength of the chamber. As the acceleration is parallel to the field, the parallel plate field strength magnitude, equation (4.1), may be substituted into the equation, hence

$$a = \frac{qV}{m_0 d},$$

where V is the potential difference between two electrodes separated by distance d. Therefore for the parallel plate chamber geometry (mentioned in section 4.1), with a specific filling gas (nitrogen in this example), the acceleration times for an electron, $\mathrm{t}_e(\mathrm{a})$, and an ion, $\mathrm{t}_{N_2^+}(\mathrm{a})$, may be calculated.

$$t_e(a) = v_e \cdot \frac{m_e d}{eV} = 9.1 \text{ ns}, \tag{6.1}$$

$$t_{N_2^+}(a) = v_{N_2^+} \cdot \frac{m_{N_2^+} d}{eV} = 290 \text{ ns}, \tag{6.2}$$

where the drift velocity of electrons (v_e) transversing N_2 is 18.0×10^5 cm/s and the drift velocity of N_2^+ ions ($v_{N_2^+}$) passing through N_2 is 6.1×10^3 cm/s (Appendix A)

Charge Collection Time

The time taken for each charge pair particle to be collected at their respective electrode may be calculated from the expression

$$t(c) = \frac{d}{v_{drift}},$$

provided the drift velocity of the charged particles (v_{drift}) is constant. Therefore, continuing on the example of a nitrogen filled parallel plate ionisation chamber, the maximum collection time for an electron, $\mathrm{t}_e(\mathrm{c})$, and an ion, $\mathrm{t}_{N_2^+}(\mathrm{c})$, may be

shown to be

$$t_e(c) = 0.3\ \mu\text{s}, \tag{6.3}$$
$$t_{N_2^+}(c) = 83\ \mu\text{s}, \tag{6.4}$$

for the scenario where an electron and an ion will travel the maximum distance possible, 0.5 cm (ie. the model is effectively two independent charge pairs, one being created very close to the anode and the other very close to the cathode). When this is the case only the charge that must travel the distance d may be considered for the total signal, as the signal induced by the other charged particle will be negligible (as it will be collected instantaneously).

These results highlight two important assumptions for the signal shape calculations. Firstly, as $t_e(c) \gg t_{N_2^+}(c)$ the ions may be considered stationary during the formation of the electron signal pulse. Similarly the electrons may be considered fully collected at the anode during the formation of the ion signal pulse.

The second important assumption is that the acceleration times may be considered instantaneous, as $t(c) \gg t(a)$. This effectively means that, immediately after creation, the ions and electrons will be moving at their respective drift velocities.

Signal Shape

The overall signal response of an electron and an ion transversing the maximum distance of a parallel plate chamber may now be determined. By substituting in the geometry of the system into equation (3.41) the current signals, as a function of position within the chamber, are achieved.

$$I_n(t) = -\frac{d}{dt} ze \left[\frac{\int_n^{y_{ion}(t)} A^{-1} ds - \int_n^{y_e(t)} A^{-1} ds}{\int_-^+ A^{-1} ds} \right].$$

If the direction of the field (s) is thought of as perpendicular to the surface area of the electrodes (A), the expression for the induced current upon the anode becomes

$$\begin{aligned} I_{anode}(t_e) &= -\frac{d}{dt} e \left[\frac{\int_0^{y_0} A^{-1} ds - \int_0^{y_e(t)} A^{-1} ds}{\int_0^d A^{-1} ds} \right] \\ &= -\frac{d}{dt} e \Big(\frac{y_0 - y_e}{d} \Big), \end{aligned} \tag{6.5}$$

$$\begin{aligned} I_{anode}(t_{N_2^+}) &= -\frac{d}{dt} e \left[\frac{\int_0^{y_{N_2^+}(t)} A^{-1} ds - \int_0^0 A^{-1} ds}{\int_0^d A^{-1} ds} \right] \\ &= -\frac{d}{dt} e \Big(\frac{y_{N_2^+}(t)}{d} \Big). \end{aligned} \tag{6.6}$$

Here, y_0 is charge pair's distance from the electrode (the anode in this example, thought to be at 0) at the point of creation. As $y - y_0 = vt$, these expressions may be re-arranged to

$$I_{anode}(t_e) = e\frac{v_e}{d}, \tag{6.7}$$

$$I_{anode}(t_{N_2^+}) = e\frac{v_{N_2^+}}{d}. \tag{6.8}$$

In equation (6.8), if the ion is to travel the maximum distance of the chamber it must be created very close to anode and move away from it (towards the cathode), hence $y_0 = 0$ and v is negative.

By inserting the appropriate values into the above equations, the signal magnitude as a function of time may be plotted for ions and electrons transversing the maximum distance of a chamber, as shown in figure 6.2

Figure 6.2: *Theoretical signal response of parallel plate chamber, for an electron and an ion transversing the maximum distance of the chamber.*

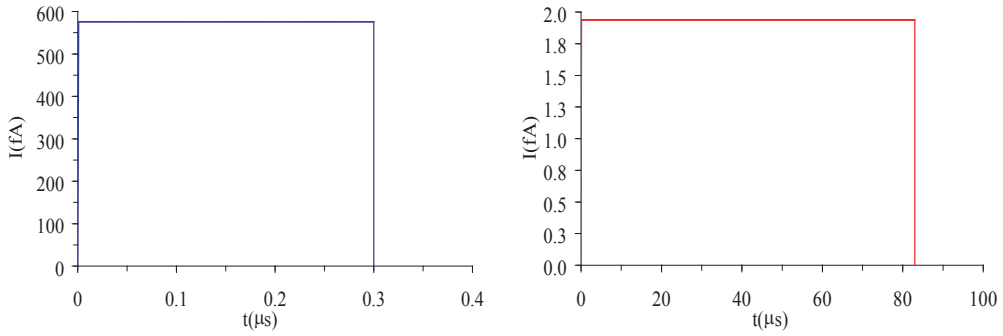

(a) *electron* (b) *ion*

The graphs clearly show that, for a parallel plate chamber the magnitude of the signal is dependant on the size of the chamber and the speed of the charged particle. The length of the signal is dependant on the collection time of the charge pair, $t_{N_2^+}(c)$ & $t_e(c)$. Further to this the integral below the curves is indentical.

6.1.2 Coaxial Chambers

The formation of signals within a coaxial chamber is slightly more difficult to formulate. Equations (6.7) & (6.8) show that the signal magnitudes and the charge collection times are dependant upon the speed at which the charge pair particles move through the chamber, which in turn is dependant upon the field strength. It is reasonable to assume (and will be shown later) that the same

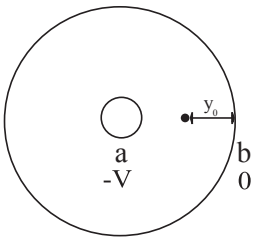

Figure 6.3: *Theoretical coaxial set-up. For simplicity of the calculations, the anode has been taken as the outer electrode.*

relationship applies for the coaxial chambers.

The problem lies within the discussions of section 4.3, where it has been shown that the field varies with position within the chamber. This additional factor brings added complications to signal equations, as the electron, and ion, drift velocities depend on the field strength.

Acceleration Time

The time taken for the charges to reach their drift velocities, directly after creation, may again be considered to be instantaneous.

Charge Collection Time

The charge collection times, $t(c)$, for the coaxial chambers may be obtained from the equation

$$S_{0-n} = vt(c) - \frac{1}{2}at(c)^2,$$

where S_{0-n} is the distance between the point of creation and the charge collection electrode. Substituting in the respective values of velocity (v) and acceleration (a) for the ions and electrons, the following expression is achieved.

$$\begin{aligned} S_{0-cathode} &= v_{ion}(E)t(c) - \frac{eE}{2m_{ion}}t(c)^2 \\ &= v_{ion}(E)t(c) - \frac{eV}{2m_{ion}r\ln(b/a)}t(c)^2, \end{aligned} \tag{6.9}$$

$$\begin{aligned} S_{0-anode} &= v_e(E)t(c) - \frac{eE}{2m_e}t(c)^2 \\ &= v_e(E)t(c) - \frac{eV}{2m_e r\ln(b/a)}t(c)^2. \end{aligned} \tag{6.10}$$

The terms $v_{ion}(E)$ and $v_e(E)$ are the ion's and electron's drift velocity as a

function of field strength, respectively. The expression for the coaxial chamber's field strength as a function of position, equation (4.2), has been substituted into the equations.

Signal Shape

Using the geometry of the 2-Coaxial system only (the 3-Coax will simply be a combination of two 2-Coaxial systems), equation (3.41) gives the expressions

$$\begin{aligned} I_{anode}(t_e) &= -\frac{d}{dt}e\left[\frac{\int_b^{y_0} A^{-1}ds - \int_b^{y_e(t)} A^{-1}ds}{\int_a^b A^{-1}ds}\right] \\ &= -\frac{d}{dt}e\frac{\ln y_0 - \ln y_e}{\ln(b/a)}, \end{aligned} \tag{6.11}$$

$$\begin{aligned} I_{anode}(t_{N_2^+}) &= -\frac{d}{dt}e\left[\frac{\int_b^{y_{N_2^+}(t)} A^{-1}ds - \int_b^{b} A^{-1}ds}{\int_a^b A^{-1}ds}\right] \\ &= -\frac{d}{dt}e\frac{\ln y_{N_2^+} - \ln b}{\ln(b/a)}. \end{aligned} \tag{6.12}$$

Due to the field, the position is now given by $y - y_0 = vt - 1/2at^2$, which from equation (3.23), and the knowledge that the motion of the ion is away from the anode (therefore $v_{N_2^+}$ is negative), allows equations (6.11) and (6.12) to be written as

$$\begin{aligned} I_{anode}(t_e) &= -\frac{d}{dt}e\frac{\ln y_0 - \ln\left(y_0 + v_e(E)t - \frac{qE}{2m_e}t^2\right)}{\ln(b/a)} \\ &= -\frac{d}{dt}e\frac{\ln y_0 - \ln\left(y_0 + v_e(E)t - \frac{qV}{2m_e r\ln(b/a)}t^2\right)}{\ln(b/a)}, \end{aligned} \tag{6.13}$$

$$\begin{aligned} I_{anode}(t_{N_2^+}) &= -\frac{d}{dt}e\frac{\ln\left(y_0 - v_{N_2^+}(E)t - \frac{qV}{2m_{N_2^+}}t^2\right) - \ln b}{\ln(b/a)} \\ &= -\frac{d}{dt}e\frac{\ln\left(y_0 - v_{N_2^+}(E)t - \frac{qV}{2m_{N_2^+}r\ln(b/a)}t^2\right) - \ln b}{\ln(b/a)}. \end{aligned} \tag{6.14}$$

Both these expressions, plus equations (6.9) & (6.10), are extremely difficult and laborious to solve directly (if solvable at all). Numerical solving methods (where the velocities field dependence is extrapolated from the published data) and simulations provide a better option for obtaining the solution. For this reason simulations were conducted, using the *Garfield* simulation program, to obtain the theoretical signal response of the coaxial chambers.

6.2 Garfield Simulations

The *Garfield* simulation code was originally developed at CERN, by Rob Veenhof, as a tool to model gaseous detectors. It may be used to calculate the trajectories of particles moving through a field, and the signals which they produce. In this investigation the code was adapted for a program that would measure the signal response of liberated charge pairs within any of the prototype ionisation chambers.

The geometries of the chambers were extremely simplified versions of the designs mentioned in section 4.1. The parallel plate chamber was taken as two infinitely long plates, 0.5 cm apart. Similarly, the coaxial chambers were simulated as two infinitely long concentric cylinders. The 2-Coaxial chamber was two cylinders of radius 0.5 cm and 3.3 cm. The 3-Coaxial, however, was simulated as two separate systems, two cylinders of radius 0.5 cm and 1.85, and two of radius 1.85 and 3.3 cm. These geometries have been shown in figure 6.4.

Figure 6.4: *Simulated Garfield geometry.*

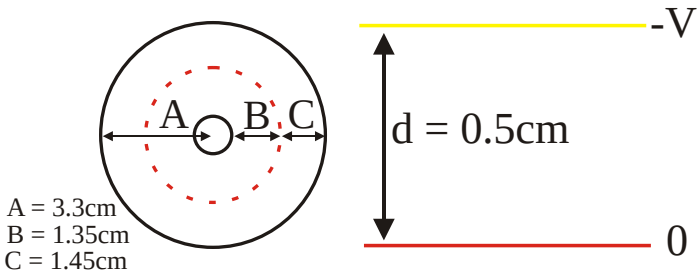

(a) *Coaxial Chambers* (b) *Parallel Plate Chambers*

The filling gasses were once again either Nitrogen, Argon or Argon Carbon-Dioxide (at 20^{o}C and 1 ATM), however some additional simulations were conducted on oxygen and air so as to examine the effect of possible leaks within the chambers.

The liberated charge pairs, which are clearly dependant upon the type of filling gas, were simulated separately from each of the constituents, in the sense that the simulations were carried out for the ions, then for the electrons. Also each charge pair was independent of another, ie. no space charge affects between particles were considered.

The movement properties of the electrons were generated from within the simulation by using the MAGBOLTZ program [31]. The movement properties of the ions, however, needed to be inserted into the program, specifically the mobility of the ion through the gas[1]. For the coaxial chambers the mobilities

[1]Some mobility values have been included in Appendix A.

had to be entered into the program as tables[2] (from which the data could be extrapolated within *Garfield*). Both the ions and electrons were considered to have no initial velocity.

The mobility values of the $ArCO_2$ mix brings a possible source of error for the program. Only one mobility may be stated for the simulation. This mobility is a direct representation of the particle that is ionised and moving through the detector. However, within a gas mixture two different types of particles may be ionised. In the case of $Ar(93)CO_2(7)$ there is considerably more argon than carbon-dioxide, therefore from section 3.2.5, a combined mobility may be considered. This would be made up of the mobility of Ar^+ ions through Ar gas (the most likely situation) and the mobility of CO_2^+ ions through Ar gas.

The latter situation is not a well documented reaction. For this reason it was assumed that the reaction between the two particle types is reversible, [12]

$$Ar^+ + CO_2 \rightleftharpoons Ar + CO_2^+.$$

In this instance the mobility of Ar^+ ions in CO_2 gas (a documented value) may be assumed to be approximately equal to the mobility of CO_2^+ ions in argon gas. The work of Mason[3] suggests that this could produce an error of approximately $\pm$ 5%. However, a brief test of the program showed that an error of $\pm$ 10% may produce an error of only $\pm$ 8 % within the signal time, suggesting that this initial assumption is sufficient.

For the main simulations, the charge pairs were distributed throughout the chamber via one of two methods;

Beam Distribution

This was used to simulate the direct impact of a particle beam upon the chamber. It simply consisted of a n particles at n_p points along a line.

Homogeneous Distribution

This distrbution was used to simulate a BLM operational situation for coaxial chambers, that being charge pairs being created at many points within the chamber. It also takes into consideration the fact that there can physically be more particles at the outer cylinder wall of the coaxial chambers than at the centre. This distribution is given by

$$n(r) = \frac{n_{total} r dr}{(b^2 - a^2)},$$

[2]This data was be obtained from [16], [17] and [18] as the mobility of the ions changed with the field (see section 4.3). Other sources may also be found within [15]

[3]The comparison of the mobility of N_2^+ ions in O_2 (3.29 cm/Vs) against the mobility O_2^+ ions in N_2 (3.14 cm/Vs) , from [11].

where $n(r)$ is the number of charges at radius r and n_{total} is the total number of charges within the chamber. The radius of the inner and outer concentric cylinders is given by a and b respectively.

6.3 Experiments

The signal response of the prototype chambers was experimentally investigated within a PSB beam dump extraction point. During an experimental run, up to two chambers would be installed within the dump area, as shown in figure 6.5(a).

The primary chamber would be installed directly in the beam line, at an open air point, where a 1.38 GeV proton beam would impact upon it. The secondary chamber was installed so that the secondary particle spectrum, created by the beam interactions with the first chamber, would impact upon it. This chamber was placed 50cm behind the primary and 20cm below.

This set-up would allow both the homogeneous (secondary chamber) and beam distributions (primary chamber) of charge pairs to be investigated and compared against the experimental data. However, the exact intensity of particles impacting upon the secondary chamber was difficult to determine. For this reason these results were normalised against the beam intensity, like the primary chambers.

Figure 6.5: *Diagram of experimental set-up for PSB test.*

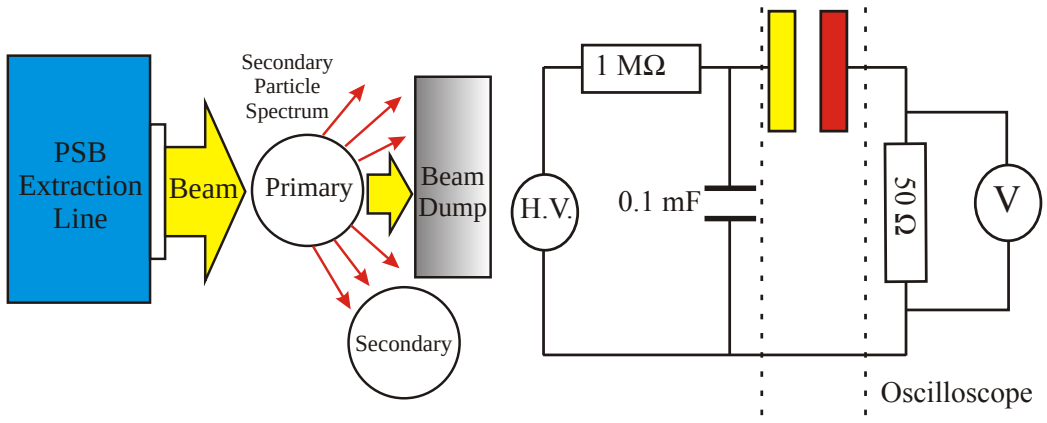

(a) *Experimental lay-out* (b) *Electronic setup*

The high voltage supply (*H.V.*) was a variable voltage source so that the characteristics of the chamber could be altered during the experiments.

The signal response of the detectors was measured using an oscilloscope, with a termination of 50 Ω (rather than the integrator electronics), and was set up as shown in figure 6.5(b). This would allow both the signal size and time to be

observed. Further to this, by altering the time period of the oscilloscope, the individual electron and ion signals could be distinguished.

6.4 Results and Analysis

The results for the simulated signal response of single charge pairs transversing a nitrogen filled ionisation chamber have been shown in figure 6.6. The theoretical signal response (shown in section 6.1.1) has also been superimposed on the plot.

The results show the signal height is irrespective of the distance travelled by the charge pairs (S) , as predicted within the theory. Similarly, the simulated results give both a signal height and charge collection time (for the maximum distance travelled in the chamber) similar to that predicted by the theory. The difference in the signal height (ΔI) and charge collection time ($\Delta t(c)$), for the electrons, was 6 % and 2 % respectively.

Figure 6.6, also shows how the signal is formed for more than one charge pair (the 'resultant' data series). As discussed within section 3.3, the overall signal for multiple charge pairs is a superposition of all individual signals. Therefore, for both homogeneous and beam type distributions, an overall linear relationship would be expected for the total signal.

Figure 6.6: *Simulated and theoretical signal responses of an electron or an ion travelling a distance S through a nitrogen filled parallel plate chamber. The resultant curve shows the superposition of the single plots. Theoretical is obtained from section 6.1.1.*

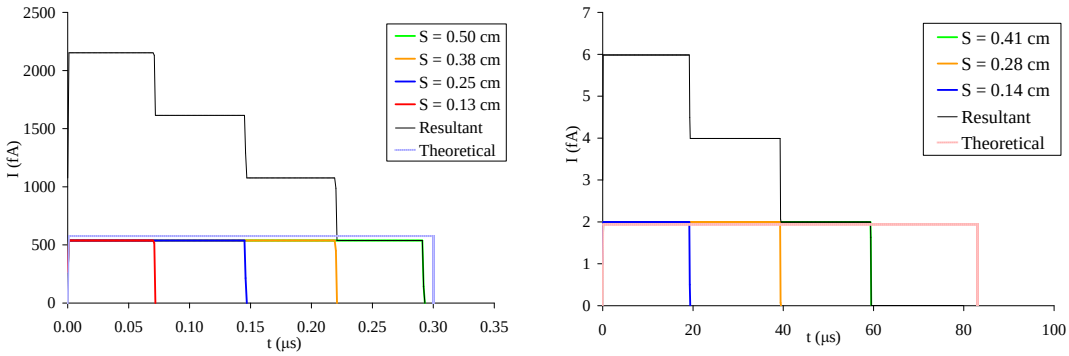

(a) *electron* (b) *ion*

The simulated response for a 100000 charge pairs in parallel plate chamber, filled with various gases, has been shown in figures 6.7(a) and 6.7(b). The

experimental results for similar parallel plate tests (with various filling gases) have been plotted within figures 6.7(c) and 6.7(d).

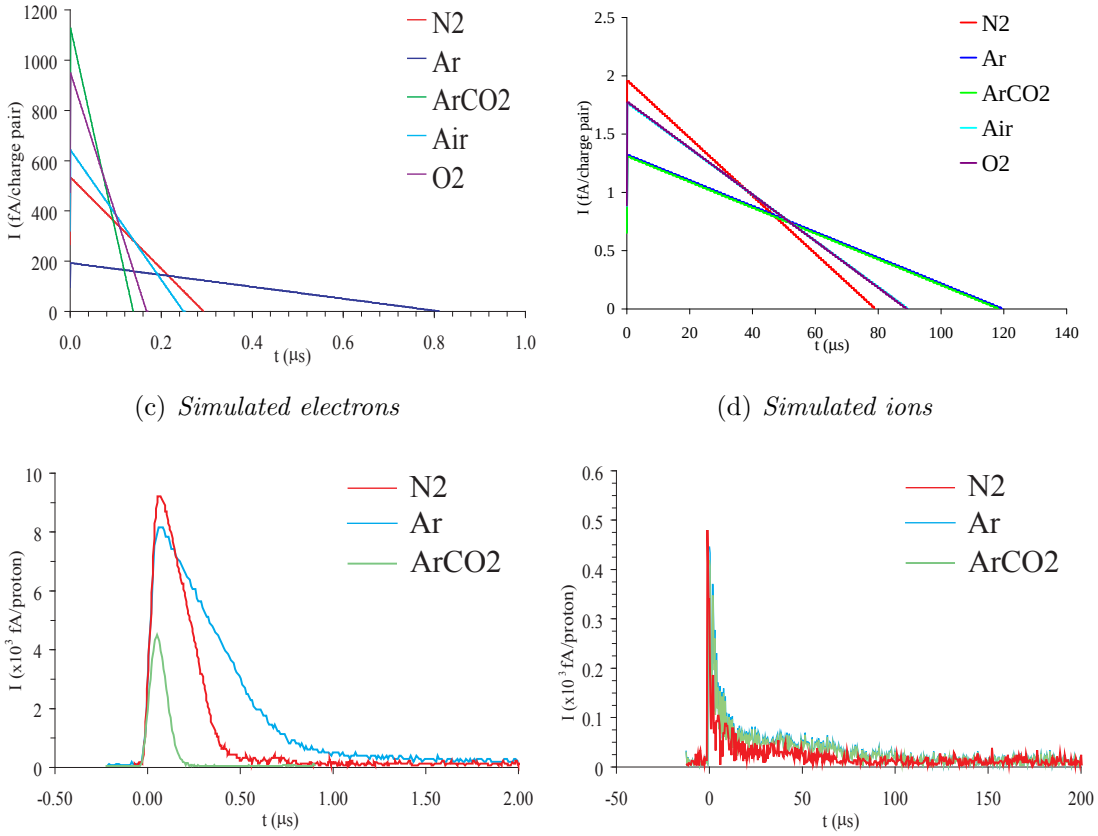

(c) *Simulated electrons*

(d) *Simulated ions*

(e) *Experimental electrons*

(f) *Experimental ions*

Figure 6.7: *Simulated and experimental response of parallel plate ionisation chamber filled with various gases*

With the exception of the experimental ion signal, the results show a linear decrease in total response with time, as would be expected from the results of figure 6.7. The experimental ion data shows an initial large signal pulse followed by a steady decline. This initial large peak is a fraction of the electrons contribution to the overall signal, which was unable to be removed from the ions time period on the oscilloscope. The steady decline shows the main characteristics of the ion signal.

Within the simulations it is assumed that all the charge pairs are created instantaneously, and accelerate very quickly to their drift velocity. However, in reality this is not immediate as particles will impact upon the chambers at different times, and for different lengths of time. This is why the experimental

results show a non-zero start (the data has been moved slightly to coincide with an instant signal peak) and a slight 'tailing-off' at the end of the signal pulse.

The tailing-off makes it difficult to get an exact signal response time for the experimental data (especially the ions). However, by taking the straight line fit for the main electron and ion signal pulse declines (excluding the tail-off), the difference between the simulated and experimental data can be estimated to be approximately 10 %.

The signal height of the experimental data is considerably larger than that simulated. This is explained through the methods of normalisation for the two data sets. The simulated data is exactly normalised to the number of charge pairs that were within the system.

The experimental tests were normalised to the beam density of the PSB, and here in lies the problem. For the primary chambers, the impact of the beam is thought to create approximately 150 charge pairs per cm per proton, hence producing a larger signal per proton.

The secondary chamber will be exposed to an unknown amount of ionising particles, which will in turn create an unknown amount of charge pairs. However it is possible that more charge pairs will be produced than the normalisation, hence producing a larger signal.

Analysis of the gas data shows that the nitrogen, argon and argon carbon-dioxide act as their properties state, see section 4.2. Ar and $ArCO_2$ have the lowest ion mobilities and hence, as shown, have the slowest ion signals. Also as the mobilities of these two gases are quite similar ($K(Ar) = 1.64cm^2V^{-1} \cdot \mu s^{-1}$, $K(ArCO_2) = 1.68cm^2V^{-1} \cdot \mu s^{-1}$) the signal shape and times are also very similar, highlighting the discussions at the end of section 6.2.

The N_2 has a larger ion mobility that the Ar & $ArCO_2$ gases, hence it produces the quicker ion signals. It also has a drift velocity larger than the Ar and hence has a quicker electron signal.

The addition of CO_2 to the Ar gas greatly increases the electron drift velocity, as expected. The electron signal time is almost 5 times quicker than pure Ar, and twice as quick as N_2. Similarly, the nitrogen is provides a quicker signal for all but the $ArCO_2$ electron drift velocity.

The oxygen and air simulation results show similar electron and ion signal times to the nitrogen ($\pm 30\%$ and $+11\%$, respectively). Therefore a leak in a nitrogen filled chamber will show no adverse affects. Conversely, a leak in an argon or argon carbon-dioxide filled chamber will decrease the total signal time, as both air and oxygen have better transport properties (Appendix A), with the exception of the electron drift velocity in $ArCO_2$.

Figure 6.8 presents the simulated signal response of single charge pairs transversing a nitrogen filled 2-Coaxial chamber. Once again the resultant curve has been plotted, to show how a signal forms for many charge pairs.

The results for the coaxial chambers show that the signal now depends on the distance the charge pair particles move through the chamber, and hence the

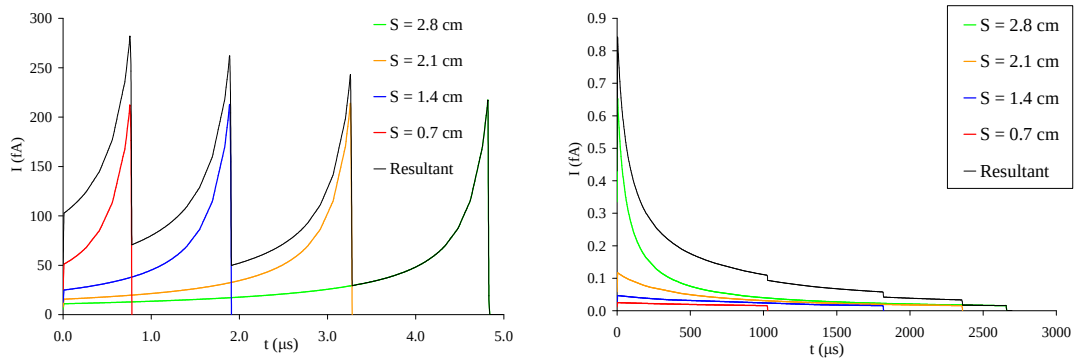

(a) *electrons* (b) *ions*

Figure 6.8: *Simulated signal responses of an electron or an ion travelling a distance S through a nitrogen filled 2-Coaxial chamber. The resultant curve shows the superposition of all the signal plots.*

time they remain within it (as would be expected from the theory that shows the signal will be dependant on the time). Figure 6.8(a) shows that, although the total electron signal will change with time, the final peak height (before collection) will constant ($\approx$ 210 fA). Conversely the ion signal is different for each distance the charge pair travels.

Within the parallel plate chambers the two distribution functions caused no real difference in signal time or signal formation (signal height would obviously vary due to the different intensities of a direct beam impact and a secondary impact). Within the coaxial chambers the simulations showed that the signal time is equal for the two particle distributions, but the resultant signal formation is not, as shown in figure 6.9.

The graph shows the simulated resultant signal of many charge pairs in a 2-Coaxial chamber. A clear signal magnitude difference is present for the two distribution types. The reason for this is less charge pairs are allowed near the inner electrode for the beam distribution than with the homogenous distribution. This means that more signal will be produced near the inner region for the homogeneous distribution.

The coaxial chambers were installed at the primary position, for the experiments carried out within the PSB. The comparison between the signals presented in figure 6.9 and the experimental signals (figure 6.10) show similarities in shape for the beam distribution. The parallel plate chambers were installed at the secondary position. As the parallel do not show a signal shape difference between homogenous and beam, no analysis could be made.

The experimental and simulated signal response of all three chamber types, filled with the argon carbon-dioxide mixture, has been shown in figure 6.10. The

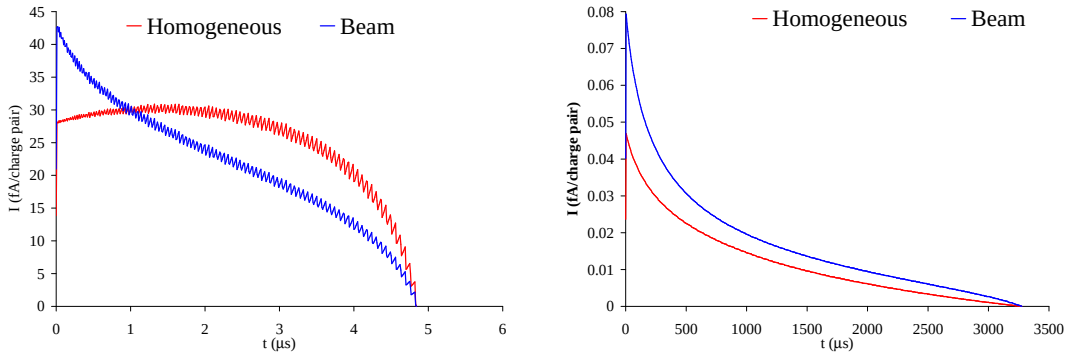

(a) *electrons* (b) *ions*

Figure 6.9: *Simulated signal of charge pairs passing through a $ArCO_2$ filled 2-Coaxial chamber, with either a homogenous or beam distribution placement.*

3-Coaxial data is the summation of the two sets of results for the inner and outer system of electrodes, mentioned in the simulation set-up.

Both sets of results show that the parallel plate chamber produces the quickest signal. It is twice as fast as the 2-Coaxial electron signal and 5 times quicker for the 3-Coaxial electron signal. Similarly the parallel plate chamber collects the ion signal 50 times and 10 times as fast as the 2 & 3-Coaxial chambers, respectively.

Comparisons between the simulated and experimental results highlight some discrepancies between the results. The overall experimental signal shape of the 2-Coaxial system is similar to that found within the simulations, and the electron signal (depending upon interpretation of the of the tailing-off) gives a difference in signal time of approximately 20%. However, the simulated ion signal time is almost 50 times larger than the experimental.

There are two explanations for the large ion signal difference. By examining the experimental curve, it could be suggested that the oscilloscope time scale was too short, as it possible that the signal pulse has not yet reached zero. Secondly it is feasible that *Garfield's* extrapolation of the ion mobilities from the data tables imprecise, hence reducing the accuracy of the simulated ion movement.

Further to this the experimental results of the 3-Coaxial chamber seem to be slightly flawed. The signal length of the electrons is considerably larger than the 2-Coaxial electron signal length, and the ion signal length is almost identical, despite the charges have to travel a shorter distance. Further to this the form of the experimental plots within figure 6.10 seems to show considerably less fluctuations in the signal, compared to other results observed. For this reason it is suggested that their may have been an error when the experiment was conducted.

The simulations also show that the chamber with the quickest signal provides the largest signal peak, as predicted in the theory. However, in reality this seems

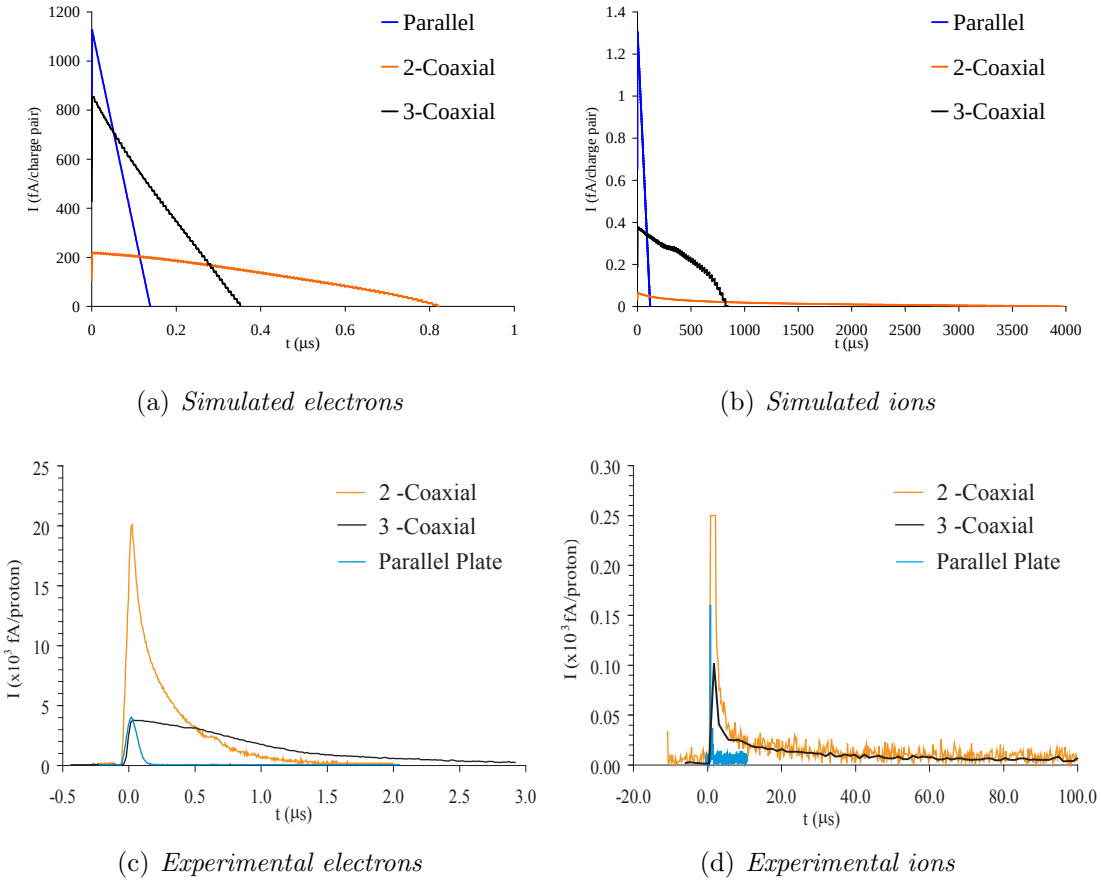

(a) *Simulated electrons*

(b) *Simulated ions*

(c) *Experimental electrons*

(d) *Experimental ions*

Figure 6.10: *Experimental and simulated signal response of the parallel plate, 2 & 3-Coaxial ionisation chambers, filled with $ArCO_2$ gas. The simulated coaxial data was run with a beam distribution.*

to be reversed, with the 2-Coaxial signal providing the largest signal. This is most likely down to the chamber being directly within in the beam, high intensity ionisation, and the parallel being in the secondary position, lower number of incoming ionising particles. However, a larger signal than the parallel plate chamber was also found within the results of chapter 5.

For both the experimental and simulated testing, it was possible to vary the potential difference that was applied between the electrodes of the chambers. One set of tests involved completely inversing the applied voltage to see the affect on the signal. Theoretically there should be no real change in signal for the parallel plate chambers, which was observed experimentally.

For the coaxial chambers it would be expected that the signal time remains the same, but the signal shape would be different. This was observed in both the experimental and simulated results shown in figure 6.11.

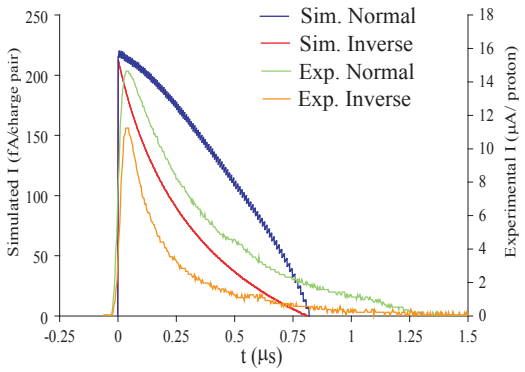

Figure 6.11: *Simulated and experimental signal of electrons passing through a $ArCO_2$ filled 2-Coaxial chamber, with normal and inversed polarity operating voltages. Beam distribution used.*

For both the electrons and the ions (not shown here) the change of electrode polarity has the effect of decreasing and increasing the magnitudes of the respective signals induced upon the electrodes. This effect may be explained from the form of the theoretical pulse formation equations (section 6.1.2), which show that the signal size has some dependence upon the direction in which the charges travel (i.e. changing a sign within the equations causes different signals). This would therefore suggest that the polarity of the chambers should be fixed for operation.

The results plotted in figure 6.12 show the simulated effect different filling gases have upon the 2-Coaxial signal. No experimental results have been plotted due to insufficient data. Only $ArCO_2$ and Ar coaxial chambers were available for the tests, of which the Ar filled chambers were found to start showing signs of the proportional counter region around the operating voltage (1500 V), hence little data was available. At high beam intensities the voltage at which this change of characteristic would occur, was even less.

This data is similar to that shown earlier for the parallel plate chamber (figure 6.7). The nitrogen gas again provides quicker ion signals than both the argon and argon carbon-dioxide filling gases, as well as a quicker electron signal than the pure argon gas. The argon-carbon dioxide mixture provides the quickest electron signal.

To determine the amount of signal collected at the electrodes, in 100μs, it is best to consider the amount of charge within the system. The integral below the curve is calculated by taking the current per charge pair and multiplying it by the measuring period of each reading (the time increment for the simulations, and the measuring increment on the oscilloscope for the experiments). Then, the relative amount of charge collected at the anodes within 100μs (Q_{100}) is simply

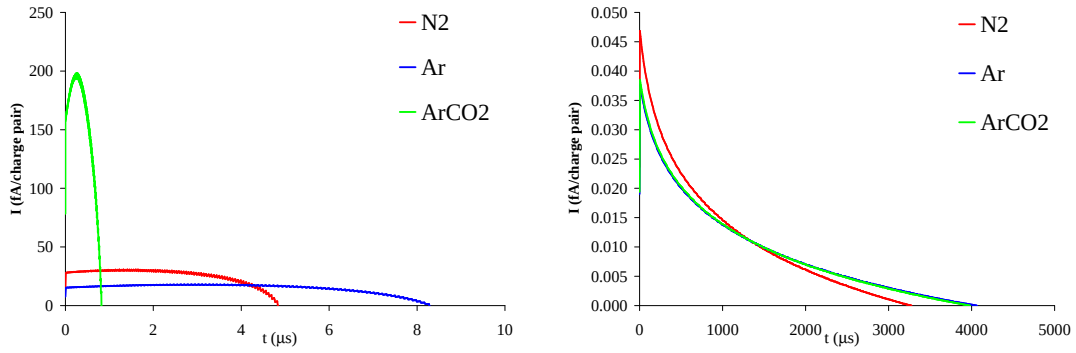

(a) *electrons* (b) *ions*

Figure 6.12: *Simulated signal response of the 2-Coaxial ionisation chamber, filled with different gases. A homogeneous distribution was used.*

the total charge at 100μs divide by the total charge for the entire signal pulse. Values for a selection of the experiments and simulations conducted have been shown in table 6.1.

		Q_{100} (%)	
Chamber Type	Gas	Simulated	Experimental
Parallel Plate	N_2	100	100
	Ar	99	87
	$ArCO_2$	99	100
	Air	100	-
	O_2	100	-
2-Coaxial Chamber	N_2	79	-
	Ar	78	-
	$ArCO_2$	78	100
Inverse Voltage	$ArCO_2$	23	-
3-Coaxial Chamber	N_2	73	-
	Ar	72	-
	$ArCO_2$	72	94

Table 6.1: *The percentage of total charge collected in 100μs from simulated and experimental data.*

The data in the table show that, for all the chambers considered within these experiments, over 70% of the signal is collected within 100μs. Simulations and experiment suggest that the parallel plate chamber collects 100% of the signal within the LHC revolution time.

The table also highlights the need for correct operating voltage on the coaxial chambers. The inverse voltage 2-Coaxial chamber collects only 23% of the signal, suggesting that the original polarity is the best for operation. This may also explain why the 3-Coaxial chamber collects the least amount of signal, which was found in both experimental and simulated data. The layout of this chamber means that one set of concentric electrodes will have normal polarity and the other inverse polarity, hence reducing the overall signal magnitude.

A result of this is that the fastest signal is not necessarily the chamber that allows the most signal to be collected. This is shown in the table for the comparison between the $ArCO_2$ filled 2 & 3-Coaxial chambers, and is due to the signal time being the same for both polarities, but the magnitude being different

The table also shows that the pure argon filling gas seriously reduces the amount of charge collected at the anodes. Further to this the simulations show that oxygen or air in the chamber will allow 100% of the signal to be collected in 100 μs. This means that normal operation will be maintained for nitrogen filled chambers with leaks, and actually improved for argon filled chambers.

6.5 Error Analysis

As the simulation was run at least 100000 times per simulation, no specific errors may be noted from the program. The only one that may be considered is that of errors within the entering of the mobilities, which as shown earlier, a 10% error in mobility relates to a 8% error within the collection time. As the error in the mobility is very small for the direct entering in the program, and unknown for the extrapolated tables, this has not been plotted.

Experimental error primarily comes from the normalisation of the signal. As mentioned earlier, a certain amount of charge pairs will be created per cm per proton. As the exact number has not yet been determined for the prototype chambers, and the distance travelled by each proton is not known (the beam is finite size) an estimate in the error of normalisation is difficult.

Similarly, as both the number of impacting particles and the number of charges created is not known for the secondary chambers, an error estimate for normalisation is very difficult. Due to this uncertainty, and the method of data collection (i.e. results taken directly from the oscilloscope), no error has been shown for the data.

6.6 Conclusion

The simulations and experiments discussed within this chapter have shown that all the prototype ionisation chambers will collect over 70% of their signal within 100μs, with simulations suggesting the parallel plate chamber will collect the most

signal (100%) and the 3-Coaxial will collect the least (73%), which was confirmed experimentally (94%).

It was also made clear through simulations and experiments that the parallel plate chamber provides the quickest signals. It allowed electron signal collection and ion signal collection, on average, 3 and 30 times as fast as the coaxial chambers. The 2-Coaxial chamber was shown to have the slowest signals.

It has been shown that generally the nitrogen gas produces the quickest signals for the suggested filling gas types, with the exception of the electron signal of the argon carbon-dioxide mixture.

Simulation have also shown that, should air or oxygen leak into the parallel plate chamber, the electron and ion signals will be similar to those of nitrogen ($\pm$ 30% and +11%, respectively) and will allow 100% of the total signal to be collected within 100μs.

Finally it has been suggested that the *Garfield* code, which was written to simulate LHC beam loss monitor signal responses, provides a good model for the parallel plate chamber and the electron signal of the coaxial chambers. Further work may be required to adapt the code for the ion signals within the coaxial chambers.

6.7 Further Suggestions

The results presented in this chapter have provide a fairly conclusive investigation into the signal response of the beam loss monitor prototypes for the LHC. However, to carry on this investigation further it is suggested the further experimental tests be carried out on all the gas mixtures in each of the chambers.

Additional experiments are proposed, involving tests with the coaxial chambers outside of the beam (to confirm distribution results) and further experiments upon the 3-Coaxial chamber (to explore previous anomalous results). Experiments with varying beam intensities may also be advisable, to investigate how this affects the operational characteristics of the chambers.

It has also been suggested that further work may be required to adapt the *Garfield* simulation code for ion movement. Primarily this would be to provide better extrapolations of the ion mobility data.

Chapter 7

Beam Loss Monitor Lifetimes

The ionisation chamber beam loss monitors, currently installed in the accelerators at CERN, are considered highly reliable devices. Their mean time between failures is approximately that specified within the LHC design specifications, being 20 years/failure.

However, to increase this reliability, and more importantly ensure that the prototypes are designed to at least reciprocate the previous versions very low failure rate, inspections were made of several ionisation chambers that were considered to have 'failed', so that any common fault may be discovered and fixed.

Further reliability considerations come from the fact that chambers installed within accelerators will be exposed to large doses of ionising particles and radiation during their lifetime. This should be considered as a hostile environment as it has been shown that any interaction between ionising particles and matter leads to a transfer of energy. This may results in physical or chemical changes in the matter, some of which may be unwanted.

Rather than specific damage or failure, the signal produced within the chambers may degrade over the years, effectively lowering the signal per proton. This would relate to an increased chance of quenches or damage within the accelerator, as more secondary particles would be required to interact with the chambers to reach the threshold dumping values.

A signal-time calibration factor would combat this affect by automatically adjusting the signal threshold for old chambers. In order to achieve this investigations were conducted to observe how the operational characteristics of the beam loss monitors changed with time.

7.1 Discussions of Possible Faults

It has been proposed that there are three main explanations for signal degradation (ageing effects) and chamber failure (when a chamber must be removed), these

are; Mechanical Damage, Material Damage and Radioactivity. These have been discussed within the following sections

7.1.1 Mechanical Damage

Mechanical damage to the chambers mainly covers, what may be considered as human error. This includes such things as incorrect manufacture or poor assembly, both of which should be found during the commissioning of the chambers.

Internal damage may also be caused by external stress (dropping or knocking), which may occur after the commissioning and is therefore very difficult to protect against

Further to this, mechanical damage could arise from the increase of heat caused by the secondary particles energy deposition. However, this is extremely unlikely within these chambers as not only will the energies be too low, but it is the chamber's role to stop such temperature increases by dumping the beam.

7.1.2 Material Damage

Material damage of the chambers is considered as either damage caused to the solid mater (the metal casing, anodes, etc.) or the adding of impurities to the gas (causing signal problems).

A particle detectors prolonged exposure to charged particles (whether they be secondary or internal charge pairs) brings on the possible problem of deposits upon the electrodes[1]. These affects manifest themselves as films or protrusions that can reduce the signal or cause field distortions (affecting the ionisation chamber regional characteristics), but the severity of these effects is dependant on the chamber geometry (wire electrodes are prone to this problem) and operating conditions (proportional and Geiger counters are also prone to deposits).

The radiation itself may cause damage to the solid matter[2]. When heavy charged particles transverse insulating or semi-conducting materials, the local structure of the solids change and tracks are formed. Continued exposure will increase the number of tracks and possibly cause lasting damage.

Structural changes and embrittlement may also occur within solid materials exposed to large doses of radiation. This is caused by the ionising particles colliding with the atoms of the material and creating a local displacement in the structural form.

The addition of impurities to the gas may cause problems with the signal response of the chamber, or even change the operational characteristics (ie. from ionisation to proportional). Impurities may appear when the created ions of the

[1] As described in [32]
[2] As described in [24]

gas recombine with foreign ions (ie. ions that are not of the same type). The chances of this happening are small, but increase with large ionising particle fluxes and complicated gas mixtures (air for example).

Further to this, impurities may occur naturally by desorbtion. This is the process by which gases that are trapped within solid matter slowly escapes with time. The process is accelerated by increased particle flux through the solid matter. Desorbtion can be minimized by proper cleaning and commissioning techniques, for the chambers.

7.1.3 Radioactivity

Prolonged exposure to large doses of radiation will make the beam loss monitors radioactive. When this occurs, the detectors themselves create charge pairs, and hence add to the signal. This is taken into consideration for the calculation of the signal, by subtracting the detector's offset (effectively the background radiation).

However, if the chambers are extremely radioactive the charge pairs they create, combined with the secondary shower's charge pairs, may allow the onset of space charge interactions or bring the detector close to saturation levels, thus effecting the signal.

7.2 Faulty Chamber Inspection Experiments

A selection of tests were proposed so as to inspect the faults of several nitrogen filled SPS type ionisation chambers. The order in which these were to be conducted has been shown in figure 7.1.

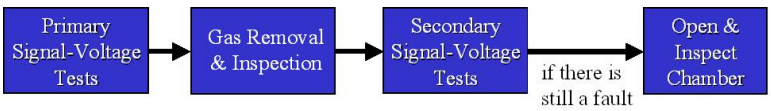

Figure 7.1: *Sequence of inspection tests.*

The initial 'Signal-Voltage' tests were conducted in the laboratory using the standard charge integrator electronics, a variable voltage supply and a cesium-137 radioactive source. These tests simply involved measuring the signals produced within the chamber, due to the Cs-137 source, at different operating voltages. This would allow the signal voltage relationship of the chamber to be plotted.

By observing the detector's signal-voltage characteristics conclusions about the faults may be made. For example, large fluctuations within the ionisation chamber region suggest field instabilities within the device [23], similarly if the signal increases significantly with voltage the chamber is operating within the proportional counter region.

It should be noted that the source was placed at the centre point of the chambers, so as to produce the maximum signal within the device (section 5.2.3).

The next set of tests, 'Gas Removal and Inspection', were proposed to inspect the internal pressure and composition of the chamber gas. The set-up of these tests has been shown in figure 7.2.

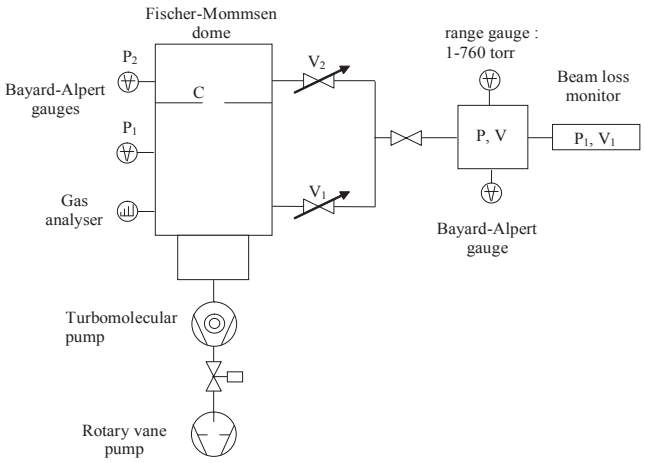

Figure 7.2: *Equipment layout for Gas Removal and Inspection tests, courtesy of F. Billard, CERN.*

At construction, the ionisation chambers are filled with the detector gas through a metal tube at the top of the chamber. After filling, the tube is 'nipped', effectively sealing the system. These tests involve applying a small force to the end of the nipped off tube, hence opening it slightly and liberating the gas.

The chamber gas will then pass into a pressure controlled environment, allowing the pressure within the chamber to be recorded. After this it will move into a gas analyser, which will give the composition of the chamber's filling gas. Unfortunately, due to departmental time constraints, these gas tests are still being conducted (as of 10.04.05).

Following the gas experiments, it was proposed that the chamber's signal-voltage' characteristics should be tested again. This time the chamber will now contain atmospheric air which, as mentioned is section 4.2, will produce similar characteristics to nitrogen (if the original filling gas was at 1.1 ATM the signals produced with air will be slightly smaller). If faults in the signal are still observed after gas extraction (ie. if the problem was not caused by the gas), the chambers were to be opened and internally examined.

7.2.1 Test Chambers

The ionisation chambers proposed for the inspection tests have been summarized in table 7.1. All detectors were nitrogen filled, SPS type, parallel plate chambers.

The I(Cs-137) column refers to the current produced within the chamber, at operational voltage (1500 V), when exposed to the cesium-137 radioactive source. The offset column, as mentioned earlier, is the background signal produced within the chamber. For non-radioactive SPS type ionisation chambers I(Cs-137) $\approx$ 45 $\pm$ 2 pA, and the maximum laboratory offset is 0.3 pA.

Chamber Number	I(Cs-137) (pA)	Offset (pA)	Inspection Reason	Suspected Problem	Chamber History
PIC003	27	0.3	low current	Possible gas leak	Installed in SPS
PIC006	51	0.3	high current	Filled to high pressure	Installed in SPS
PIC007	53	0.3	high current	Filled to high pressure	Never been installed
PIC009	43	0.3	reference chamber	-	Never been installed
PIC010	45	1.0	high offset	Unknown	Never been installed
PIC001	53	0.2	high current	Filled to high pressure	Never been installed

Table 7.1: *Chambers to be inspected. Chamber number is the project reference number for each chamber.*

7.2.2 Results and Analysis

Although the fault inspection experiments are still being conducted, the initial signal-voltage tests have been completed, the results of which have been shown in figure 7.3. This data shows, when comparing against the reference chamber PIC009, that all the test chambers seem to be working within the normal ionisation chamber region properties. The average fluctuations in the signal plateau (ionisation chamber region) are only 0.75 pA ($<\sigma>$), and all chambers reach the start of this section at about 50 V. This therefore suggests that there are no field distortions within the chamber, and most likely no forms of damage that may cause these distortions.

Further to this, the 'fault' in the chambers seems to cause a proportional shift in the magnitude of the signal for the entire voltage range. This would therefore back the proposal that some of the test chambers have different internal gas pressures, due to the fact that (as mentioned in section 4.2) variations in pressure cause linear variations in the signal output for ionisation chambers.

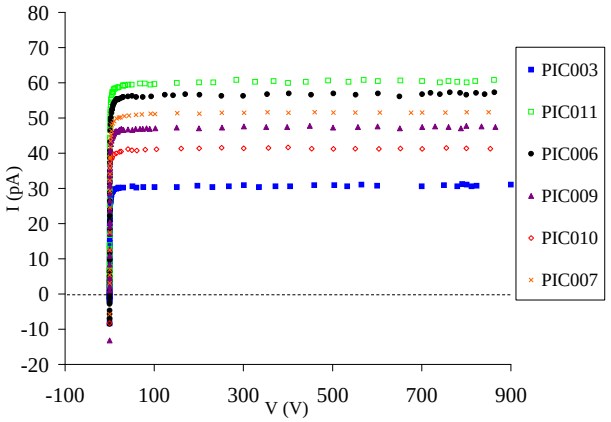

Figure 7.3: *Signal-Voltage relationship of the test chambers. Experiments conducted with Cs-137 source and standard electronics.*

7.2.3 Error Analysis

Two main sources of error arise within the signal-voltage experiments. The varying voltage source, for high potential differences (>300 V), is only accurate to ± 1 V, however this is too small to plot on the horizontal axis.

The other cause of error is the fluctuations in the signal, caused by electronic noise and the random emittance of the radioactive source. These factors mean that the signal error is on average ± 0.75 pA, again too small to be plotted on the vertical axis of the graph.

7.2.4 Conclusion

The experiments discussed within this section show that the faulty test chambers are all operating within the normal ionisation characteristics for the SPS type parallel plate chambers. This suggests that there is no internal damage to these chambers.

The results also show that the faulty chambers receive a proportional shift in the signal magnitude for the entire voltage range. This suggests that the problem with the chambers could be related to the internal pressure of the chambers.

7.2.5 Further Suggestions

The voltages used in the initial experiments were limited by the capacitor in the low pass filter, which cannot accept more than 1500 V. As an extension to these tests, it is suggested that this capacitor is replaced, with one that allows larger

voltages, and the readings are extended to the start of the proportional counter region.

7.3 Accelerated Lifetime Experiments

It has been proposed that ionisation chambers exposed to large amounts of radiation, for long periods of time, may develop signal degradation. This hypothesis has been supported by tests conducted in 2003 on all the installed SPS ionisation chambers (over 200), shown in figure 7.4. Each of the installed chambers were exposed to the Cs-137 source and their signal recorded. The figure shows the distribution of main ring[3] and injection/extraction[4] detectors around the mean signal (45 pA).

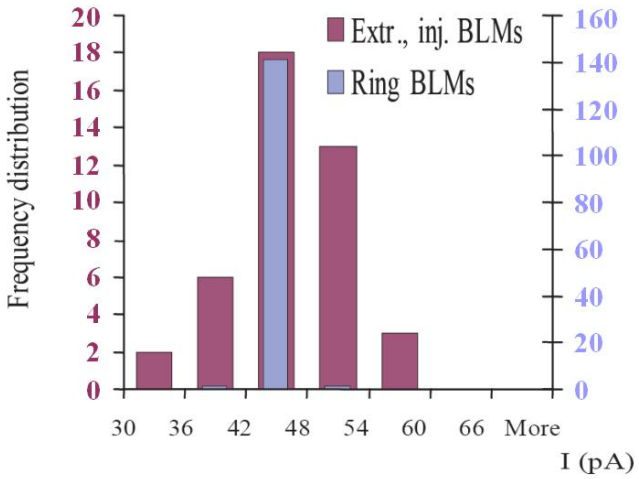

Figure 7.4: *Signal magnitude of SPS main ring, extraction and injection ionisation chambers exposed to a Cs-137 source.*

The results of the figure 7.4 show that chambers installed within the main ring are closely distributed around the mean value ($\sigma = \pm 0.5\%$). Chambers installed in the more radioactive injection /extraction areas have a wider distribution around the mean value ($\sigma = \pm 5.0\%$), thus backing the theory of signal degradation.

To observe the signal degradation within the chambers, accelerated lifetime tests were proposed. The premise of these investigations was to expose the chambers to very large doses of radiation for an extended period of time, and to monitor how the signal changes.

[3]Chambers installed in the main ring monitor losses from the SPS accelerator.

[4]Chambers installed within the extraction or injection lines are placed in areas were the beam is either injected into or removed from the SPS main ring.

These tests were conducted within the splitter section of a SPS extraction line. Here the beam is 'split' into three separate beams and is exposed to very large loss rates from the beam. The radiation exposure of chambers installed within this area is thought to be 20 times larger than that of the SPS main ring chambers (which were estimated to receive 1.4 ± 1 kGy per year per chamber, [27]).

Two 'new' ionisation chambers were installed together, with dosimeters, in the splitter for the 2004 SPS operational cycle. This area is so radioactive that access is not allowed during the running period of the accelerator. Therefore these chambers (including detectors already installed within the area) were tested with the Cs-137 source before and after the operational cycle. At the end of the cycle the dosimeters were removed and analysed.

Unfortunately, at the end of the 2004 SPS operational period, a CERN-wide equipment failure[5] meant that the charge integrator electronics would not work correctly. For this reason a low current multi-meter was used instead. This would give an instant reading of the current passing through the chamber, rather than an integrated signal.

7.3.1 Results and Analysis

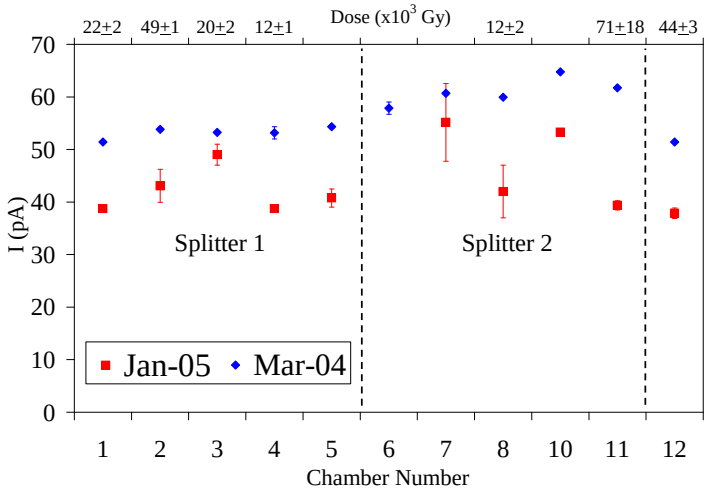

Figure 7.5: *Signal response to Cs-137 source for all splitter chambers. Splitter 1 & 2 are different areas within the splitter. Chambers 1 & 12 are installed within at the same position within splitter 1. Tests were conducted in 2004 and 2005. All values have been offset adjusted.*

[5]The failure was with the timing trigger mechanism of the standard electronics.

The signal response to the Cs-137 source, for the SPS splitter ionisation chambers, at the beginning and the end of the 2004 SPS operation period has been shown in figure 7.5. The radiation dose the chambers received during this period has also been shown. The comparison between the two sets of data show that the signal after shutdown (Jan-2005) is lower than before, suggesting signal degradation.

Further comparisons are inconclusive as the variations in the signals for the Jan-2005 results are too large. This is caused by the use of the low current multimeter in obtaining the signals. As it took instantaneous current readings, it lacked the statistical advantage of the charge integrator electronics, which would take 465 independent signal readings in 9.81s.

Analysis of the Mar-04 data series shows that there is a difference in the average signal for splitters 1 & 2. This again provides evidence for the signal degradation proposal, as the chambers within splitter 1 were changed between 8-12 years ago[6] and the splitter 2 chambers have been installed since SPS construction.

7.3.2 Error Analysis

The error bars plotted in figure 7.5 have been obtained from the fluctuations around the mean for each chamber.

7.3.3 Conclusion

It has been shown for the SPS type ionisation chambers, that prolonged radiation exposure causes a variation in the signal of the detector. However, no relationship between the length, or dose, of exposure and the change in signal has yet been found, due to technical difficulties. Therefore no calibration constant has been proposed.

7.3.4 Further Suggestions

As there is a clear radiation effect upon the signal, it is suggested that the SPS splitter chambers are re-examined at a later date with the standard detector electronics and cesium source.

[6]Unfortunately there is no record of the exact installation date.

Chapter 8

Design Conclusions

A comprehensive investigation into the design considerations for ionisation chambers, used as LHC beam loss monitors, has been presented in the previous chapters. It has been shown, with simulations and measurements, that the parallel plate and 2-Coaxial chambers collected 100 % of their total signal in 100 μs, while the 3-Coaxial collects 94%. Further to this the parallel plate chambers were found to give the quickest signals, being, on average 3 and 30 times quicker than the coaxial chambers, for the electron and ion signal respectively.

The parallel plate chamber was also found to have the most homogeneous signal throughout the chamber, with the simulations showing 40% lower fluctuations than the coaxial chambers, and experiments showing 12% lower fluctuations. The difference in the total integrated charge between simulations and measurements was found to be approximately 35%, for a proton beam.

The coaxial chambers were found to provide the largest signal per lost beam proton, with the 2 & 3-Coaxial being approximately equal. However, the sensitivity to low energy particles was less than the parallel plate chambers, due to the additional matter of the coaxial electrodes. Simulations showed that the non-gaseous matter affects the fluctuations in the signal response by absorbing lower energy particles, and creating large ionising secondary showers for high energy particles.

The investigations also highlighted that the filling gases with the fastest drift velocities would provide the quickest signals, and the gasses with the largest energy deposition rates would provide the largest signals. Measurements showed that the nitrogen gas produced the quickest signals (with the exception of the argon carbon-dioxide electron signal) and the argon produced the largest signals (1.77 times larger than the nitrogen).

The possible leak impurities, oxygen and air, were found to have similar electron and ion signal times to nitrogen ($\pm$30% and +11 %, respectively) and also allowed 100% of the signal to be collected in 100 μs, for a parallel plate chamber.

It has also been shown that the SPS type ionisation chambers display

signs of signal degradation with prolonged exposure to high levels of radiation. Experiments found that low radiated chambers ($\approx$ 1 kGy/per year) show a variation in the mean signal (σ) of only 0.5%, where as higher radiated chambers (between 2-10 kGy/year) show $\sigma = 5\%$. Experiments are still being conducted to determine an ageing calibration constant.

The cumulative result of these design investigations is the decision that the LHC beam loss monitors will be the nitrogen filled parallel plate chambers. Their reliability, quick signals and low fluctuations outweigh the coaxial chamber's better sensitivity. These chambers will be filled to 1.2 ATM, so that possible chamber leaks may be identified by the lower signals produced at 1 ATM.

Appendix A

Material Data Tables

Table A.1: *Relevant gaseous material properties.*

Gas	Z	A (AMU)	ρ^a (g/l)	$\{dE_n/dx\}_{min}{}^b$ (MeV cm^{2}g^{-1})	$I_e{}^c$ (eV)	Φ^d (eV)	$E_w{}^e$ (eV)	K^f (cm^2/Vs)	$v_e{}^g$ $\times 10^5$cm/s
He	2	4.00	0.179	1.937	24.6	-	41	-	22
N_2	7	14.01	1.250	1.825	82	14.5	35	2.0	18
O_2	8	16.00	1.141	1.801	95	13.6	31	2.05	31
Ar	18	39.95	1.782	1.519	188	15.8	26	1.6	10
CO_2	-	44.02	1.977	1.819	85	13.7	33	2.3	-
Air^i	-	-	1.293	1.815	85	-	35.6	2.3	20

Table A.2: *Relevant solid material properties.*

Material	ρ^h (g/cm^3)	Composition	Z	A (AMU)	$\{dE_n/dx\}_{min}{}^h$ (MeV cm^{2}g^{-1})
Stainless Steel	8.03	Fe 75%	26	56	
		Cr 17%	27	52	
		Ni 8%	28	88	
Aluminium	2.70	Al	13	27	1.615

[a] Values taken at STP, [2].
[b] Evaluated at 20°C and 1 ATM, [2].
[c] Taken from [6].
[d] Values availabel from `http://www.vcs.ethz.ch/chemglobe/ptoe/index.html`.
[e] Taken from [8].
[f] For field strengths of 3000 V/cm, temperatures of 300K and pressures of 1 ATM, [16].
[g] For field strengths of 3000 V/cm, temperatures of 300K and pressures of 1 ATM, [7].
[h] Taken from [2].
[i] Within disertation, air is considered 78% N_2, 21% O_2 & 1% Ar.

Appendix B

Simulated *Geant 4* Chamber Geometry

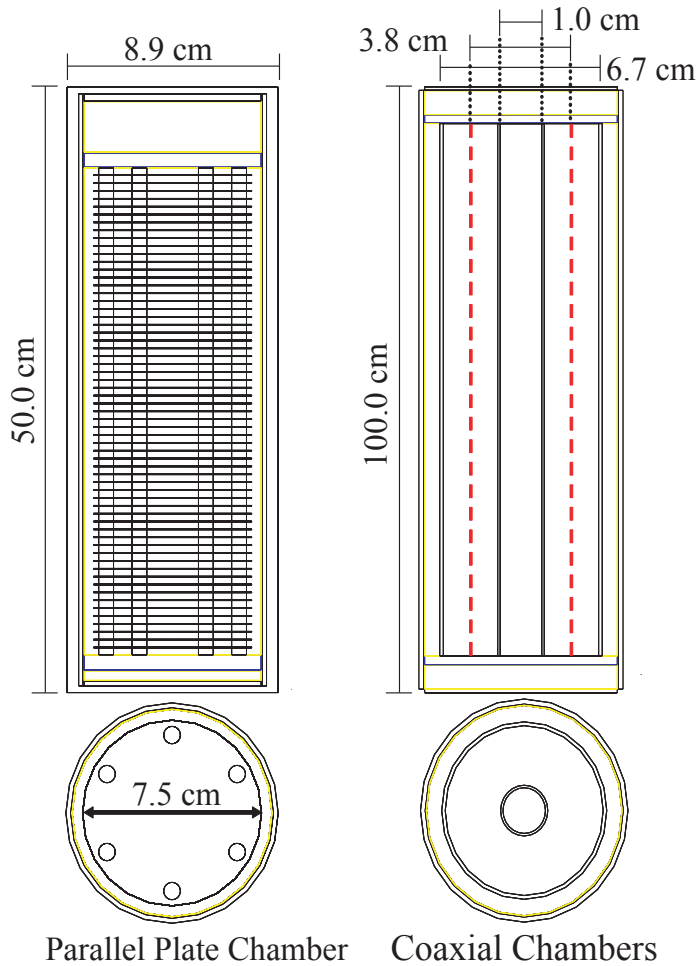

Appendix C

Chamber Technical Drawings

The figures presented in the following three pages of this appendix are the technical drawings[1] for all three ionisation chambers. They are, in order of appearance,

- the Parallel Plate Ionisation Chamber,
- the 2-Coaxial Ionisation Chamber,
- the 3-Coaxial Ionisation Chamber.

For each chamber the outer casing is stainless steel and the electrodes are aluminium. The insulators are an aluminium compound ceramic (Al_2O_3). For the parallel plate chamber the support rods are stainless steel.

The outer casing is approximately 8.9cm in diameter. The length of the casing is 50cm and 100cm for the parallel and coaxial chambers respectively.

The coaxial electrodes are approximately 1.0cm, 3.8cm and 6.7cm in diameter for the inner, middle and outer electrodes respectively.

The parallel plate electrodes are 0.5cm apart and have a diameter of approximately 7.5cm.

[1] Full schematics are available at `https://edms.cern.ch/`

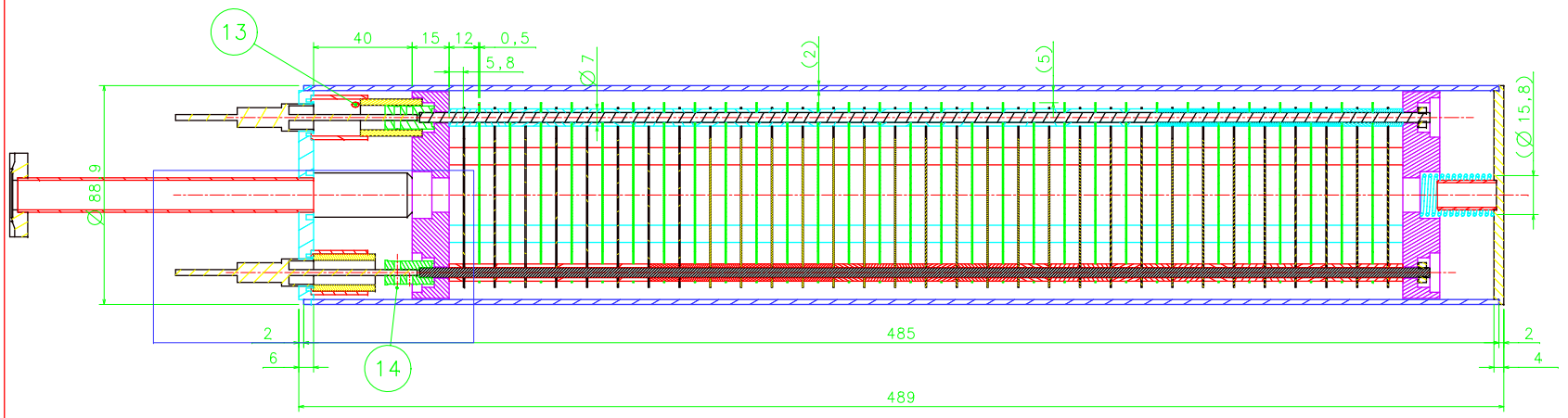

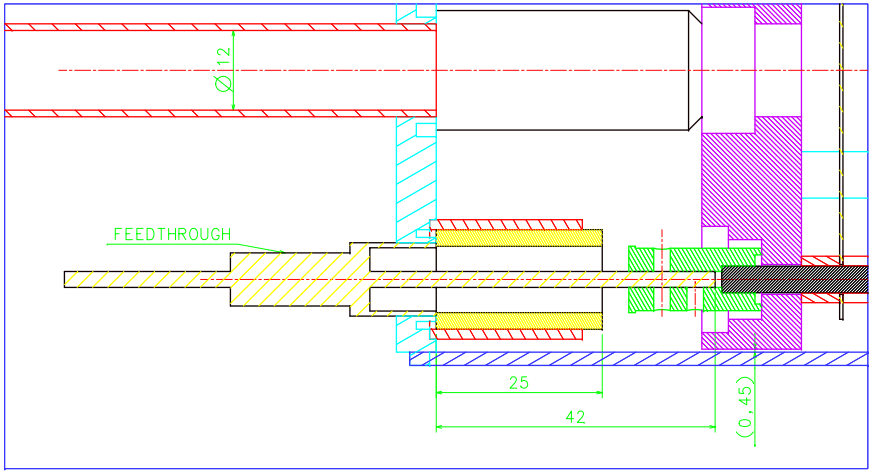

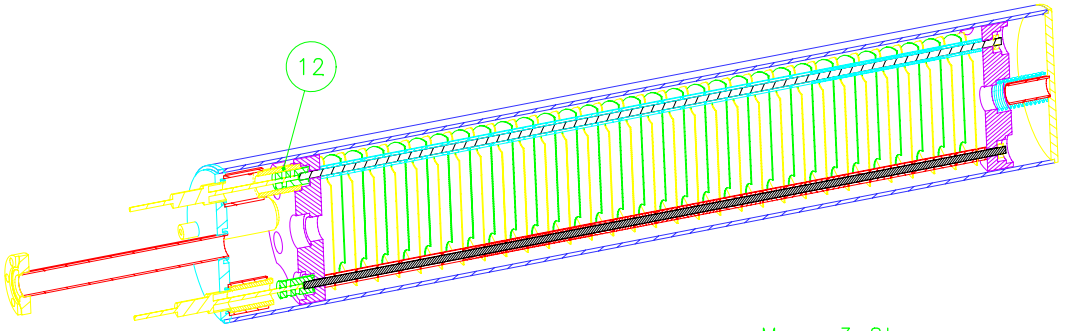

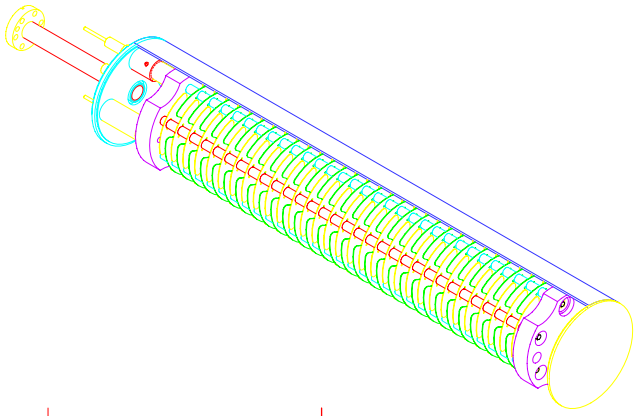

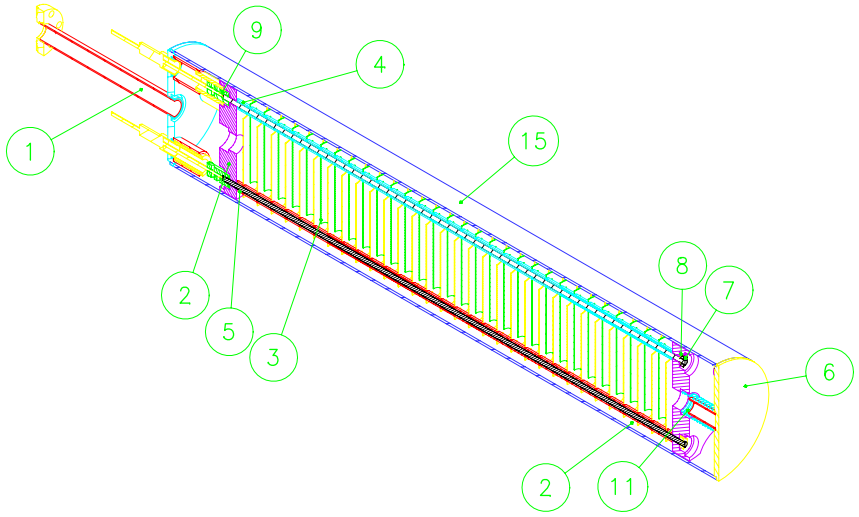

Mass=3.8kg

QUANT	DESCRIPTION	POS.	MAT.	OBSERVATIONS	REF.CERN
1	ROUND TU. 304L WELD. 88,9x2,0	15			39.39.05
	TUBE ROND 304L SOUDE 88,9X2,0				088.2
2	VIS S.T. 6PC CHAN.INOX M 3X4	14			47.62.87
	VIS S.T. 6PC CHAN.INOX M 3X4				145.0
2	INOX SP.CYL.SCR.A4 316 M3 x 6	13			47.62.39
	VIS CYL.FO.INOX A4 316 M3 x 6				306.8
2	ALUMINA TUBE Ø 15/10	12	Al203		19.63.30
					128.9
1	COMPRESSION SPRING	11	1.4310	Ferroflex VD-180M-14	
4	TIGHTENERS M4 –	10		LHCBLM__0016 TYPEA-VARIANTE 1	
	–				
2	TIGHTENERS M4 –	9		LHCBLM__0016 TYPE B-VARIANTE 1	
	–				
6	SPRING WASHER Ø 8/4,2-0,2	8	1.4310	BOSSARD BN838	
6	HEX.NUTS INOX A4 316 0,8D M4	7			47.43.77
	ECROU 6P.INOX A4 316 0,8D M4				040.1
1	BOTTOM COVER –	6		LHCBLM__0006-TYPE A	
	–				
6	ELECTRODE SPACERS –	5		LHCBLM__0007 TYPE C	
	–				
183	ELECTRODE SPACERS –	4		LHCBLM__0007-TYPE A	
	–				
61	ELECTRODE –	3		LHCBLM__0004	
	–				
2	ALUMINE INSULATOR –	2		LHCBLM__0005	
	–				
1	COVER ASSEMBLY –	1		LHCBLM__0002-TYPE A	
	–				
	ENS./ASS.		S.ENS/S.ASS.		

Beam Loss Monitor

MULTIPLE ELECTRODE BLM
WELDED VERSION ASSEMBLY

ECHELLE SCALE 1:1

DES./DRA.	G.FOFFANO	2004-05-06
CONTROLLED	R.PERPET	2004-05-07
RELEASED	E.HOLZER	2004-05-18
APPROVED	–	–

LHCB_BLM____BEAM_OS000_B0072_B0072005PL

REMPLACE/REPLACES

RELEASED BY PROJECT ENGINEER | FOR INFORMATION | QAC – | LHCBLM__0001 | SIZE 1 | IND.

IND.	DATE	NOM/NAME	ZONE	MODIFICATION

DESIGN, RUGOSITE, TOLERANCES SELON NORME ISO
DRAWING, RUGOSITY, TOLERANCES ACCORDING TO ISO STANDARD
PROJECTION

ORGANISATION EUROPEENNE POUR LA RECHERCHE NUCLEAIRE
EUROPEAN ORGANIZATION FOR NUCLEAR RESEARCH

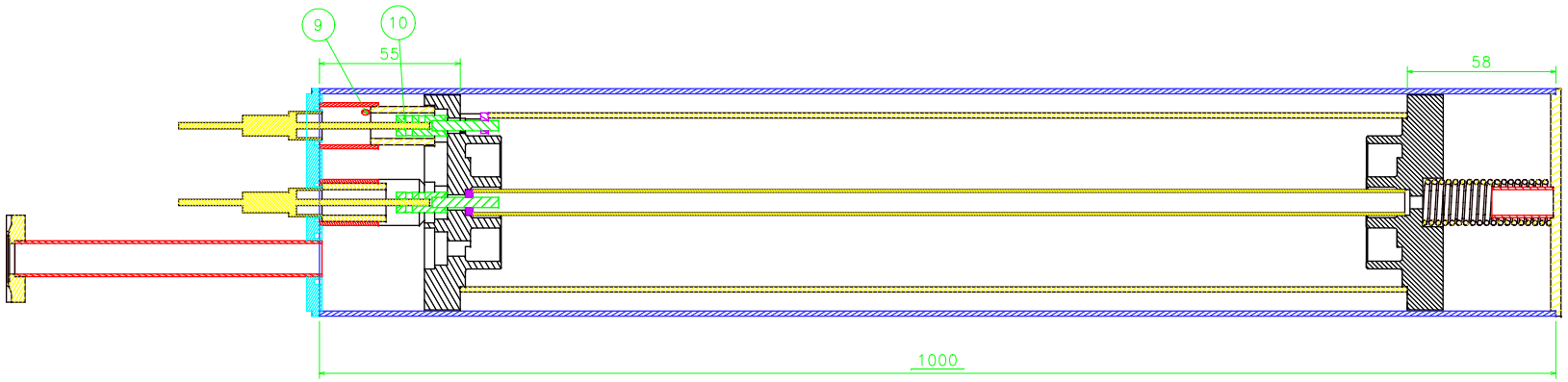

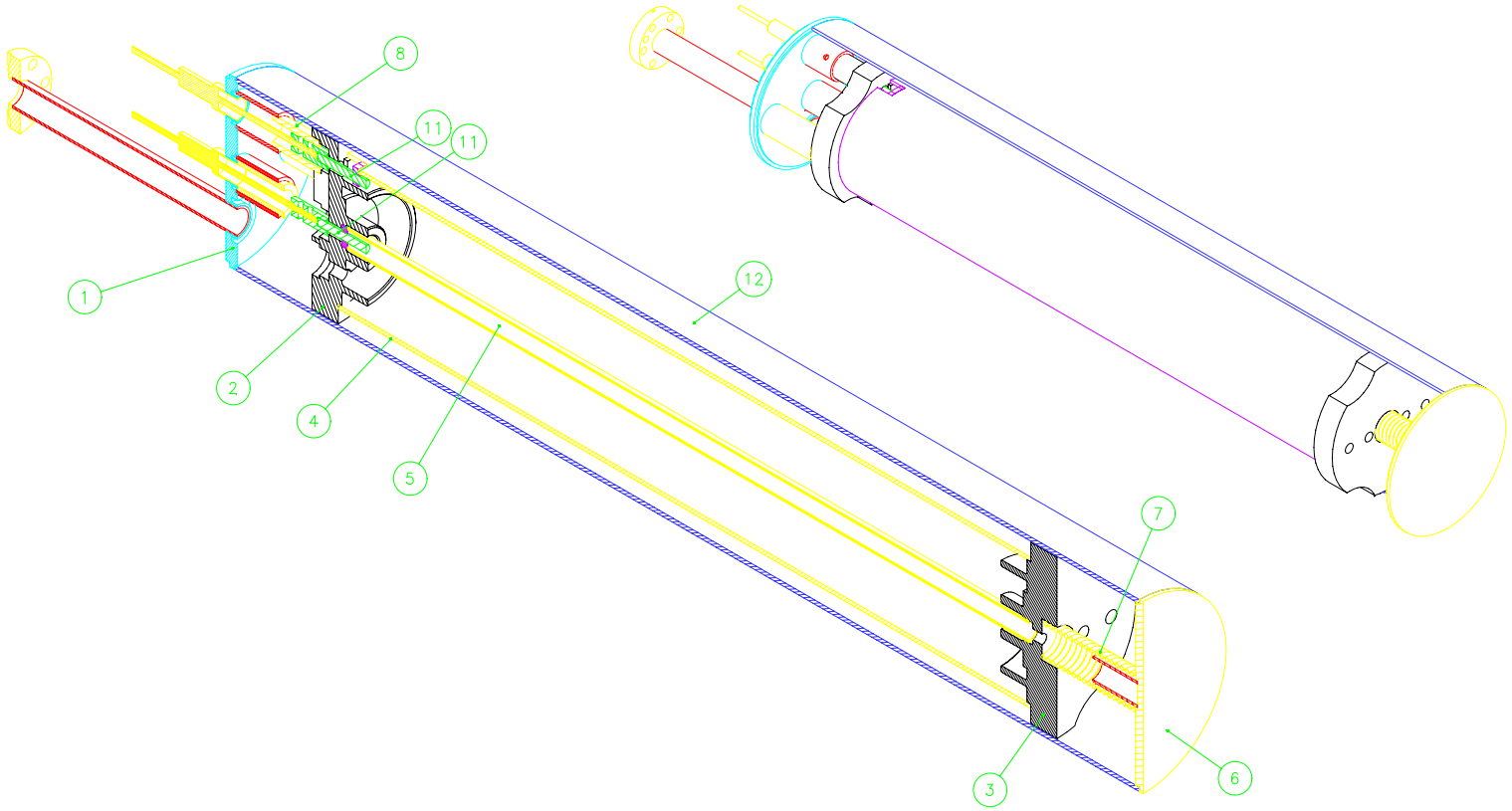

QUANT.	DESCRIPTION	POS	MAT.	OBSERVATIONS	REF.CERN
1	ROUND TU, 304L WELD. 88,9x2,0	12			39.39.05
	TUBE ROND 304L SOUDE 88,9X2,0				088.2
2	MULTIPLE ELECTRODE BLM - TIGHTENE	11		LHCBLM__0016 VARIANTE 4-TYPE B	
	–				
2	VIS S.T. 6PC CHAN.INOX M 3X4	10			47.62.87
	VIS S.T. 6PC CHAN.INOX M 3X4				145.0
2	INOX SP.CYL.SCR.A4 316 M3 x 6	9			47.62.39
	VIS CYL.FD.INOX A4 316 M3 x 6				306.8
2	ALUMINA TUBE ∅ 15/10	8	Al2O3	L=25mm	19.63.30
					128.9
1	COMPRESSION SPRING	7	1.4310	Ferroflex VD-251A	
1	WELDED BLM - BOTTOM COVER	6		LHCBLM__0006 TYPE C	
	–				
1	COAXIAL BLM - CENTRAL ELECTRODE	5		LHCBLM__0032	
	–				
1	COAXIAL BLM - EXTERNAL ELECTRODE	4		LHCBLM__0030	
	–				
1	COAXIAL BLM - ALUMINA TYPE 2	3		LHCBLM__0019	
	–				
1	COAXIAL BLM - ALUMINA TYPE 1	2		LHCBLM__0018 -VERSION B	
	–				
1	2 ELECTRODES COAXIAL BLM - WELDED	1		LHCBLM__0026	
	–				

ENS./ASS. S.ENS./S.ASS.

Beam Loss Monitor

2 ELECTRODES COAXIAL BLM ASSEMBLY (WELDED)

ECHELLE SCALE 1:1

DES/DRA.	G.FOFFANO	2004-05-06
CONTROLLED	C.MENOT	2004-06-07
RELEASED	B.DEHNING	2004-06-08
APPROVED	–	–

LHCBJBLM____BEAMLOS000JB007JB007209PL

REMPLACE/REPLACES

RELEASED BY: PROJECT ENGINEER | FOR INFORMATION | GAC: – | LHCBLM__0021 | SIZE 1 | IND. A

IND.	DATE	NOM/NAME	ZONE	MODIFICATION
A	2004-06-07	G. FOFFANO		UPDATED

DESIGN, RUGOSITE, TOLERANCES SELON NORME ISO
DRAWING, RUGOSITY, TOLERANCES ACCORDING TO ISO STANDARD
PROJECTION

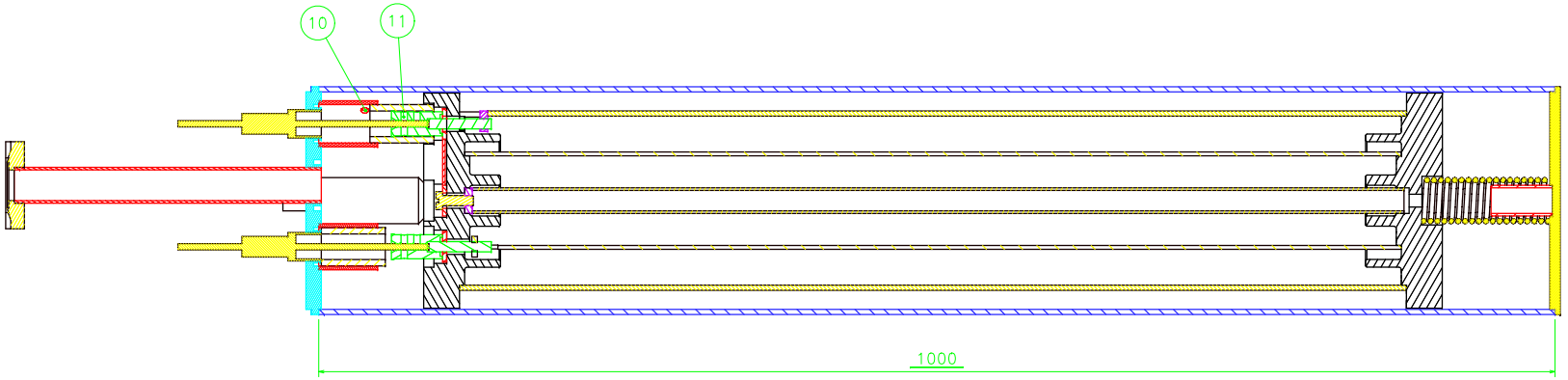

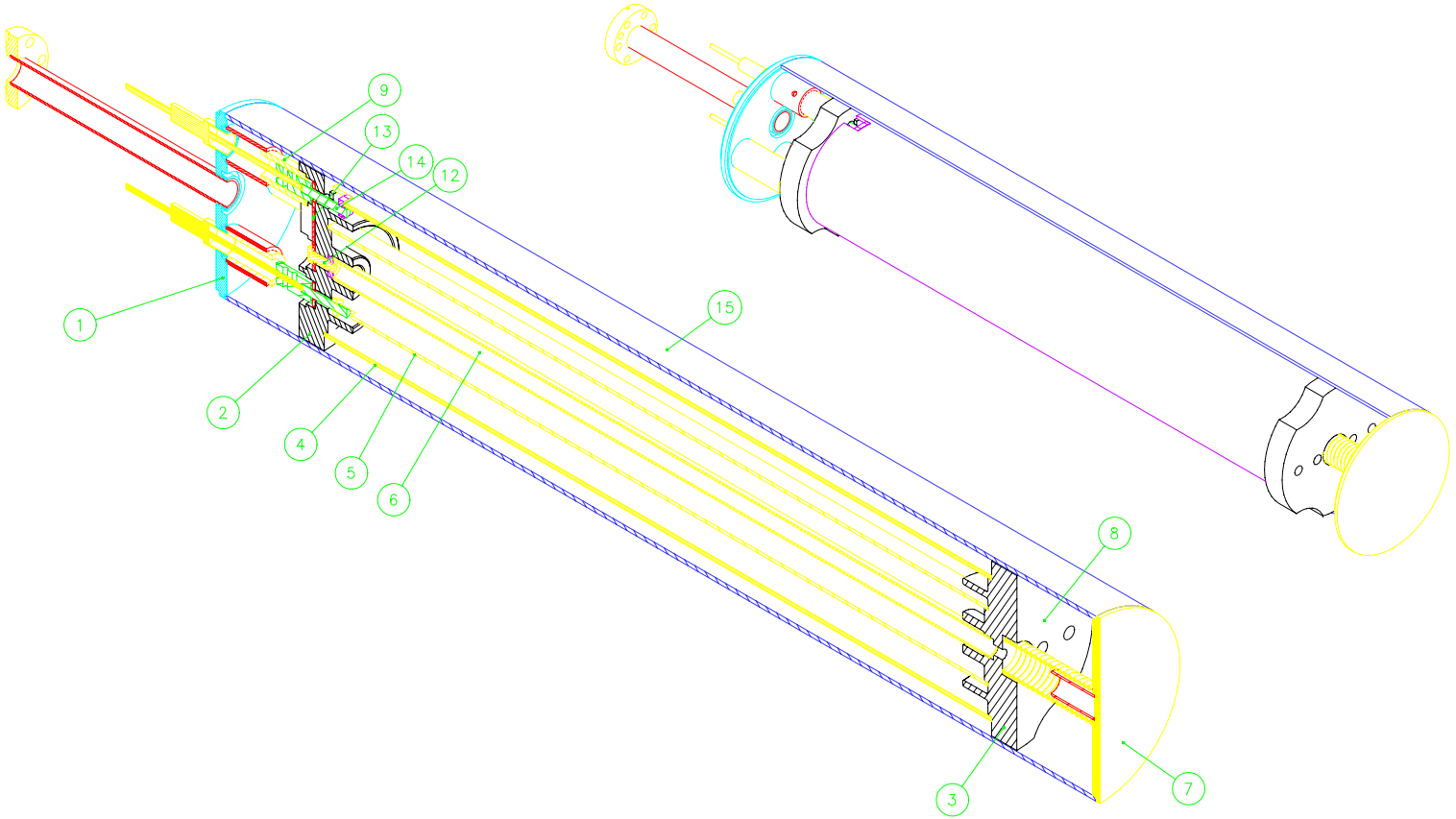

QUANT	DESCRIPTION	POS	MAT.	OBSERVATIONS	REF.CERN
1	ROUND TU. 304L WELD. 88,9x2,0	15			39.39.05
	TUBE ROND 304L SOUDE 88,9X2,0				088.2
1	MULTIPLE ELECTRODE BLM - TIGHTENE	14		LHCBLM__0016 VARIANTE 4-TYPE B	
	–				
1	3 ELECTRODES COAXIAL BLM - ELECTR	13		LHCBLM__0033	
	–				
1	INOX SP.CYL.SCR.A4 316 M4 x10	12			47.62.39
	VIS CYL.FD.INOX A4 316 M4 x10				410,9
2	VIS S.T. 6PC CHAN.INOX M 3X4	11			47.62.87
	VIS S.T. 6PC CHAN.INOX M 3X4				145,0
2	INOX SP.CYL.SCR.A4 316 M3 x 6	10			47.62.39
	VIS CYL.FD.INOX A4 316 M3 x 6				306.8
2	ALUMINA TUBE ∅ 15/10	9	Al203	L=25mm	19.63.30
					128.9
1	COMPRESSION SPRING	8	1.4310	Ferroflex VD-251A	
1	WELDED BLM - BOTTOM COVER	7		LHCBLM__0006-TYPE C	
	–				
1	COAXIAL BLM - CENTRAL ELECTRODE	6		LHCBLM__0032	
	–				
1	3 ELECTRODES COAXIAL BLM - MIDDLE	5		LHCBLM__0031	
	–				
1	COAXIAL BLM - EXTERNAL ELECTRODE	4		LHCBLM__0030	
	–				
1	COAXIAL BLM - ALUMINA TYPE 2	3		LHCBLM__0019	
	–				
1	COAXIAL BLM - ALUMINA TYPE 1	2		LHCBLM__0018 -VERSION A	
	–				
1	3 ELECTRODES COAXIAL BLM - WELDED	1		LHCBLM__0025	
	–				

ENS./ASS. S.ENS/S.ASS.

Beam Loss Monitor

3 ELECTRODES COAXIAL BLM
ASSEMBLY (WELDED)

ECHELLE SCALE 1:1

DES/DRA.	G.FOFFANO	2004-05-06
CONTROLLED	R.PERPET	2004-05-07
RELEASED	E.HOLZER	2004-05-18
APPROVED	–	–

LHCB_BLM____BEAM_LOS000_B007_B007210BPL

REMPLACE/REPLACES

RELEASED BY PROJECT ENGINEER | FOR INFORMATION | QAC – | LHCBLM__0020 | SIZE 1 | IND.

IND.	DATE	NOM/NAME	ZONE	MODIFICATION

DESIGN, RUGOSITE, TOLERANCES SELON NORME ISO
DRAWING, RUGOSITY, TOLERANCES ACCORDING TO ISO STANDARD
PROJECTION

ORGANISATION EUROPEENNE POUR LA RECHERCHE NUCLEAIRE
EUROPEAN ORGANIZATION FOR NUCLEAR RESEARCH

Ce dessin ne peut être utilisé à des fins commerciales sans autorisation écrite.
This drawing may not be used for commercial purposes without written authorisation.

Bibliography

[1] H.H. Refsum, *Design, Simulation and Testing of a 2D Electron Source Based Calibrating System for a Proton Beam Ionisation Profile Monitor*, Thesis for NTNU, Norway (2004)

[2] *The European Physical Journal C*, Vol. 15, No. 1 - 4, (2000)

[3] CERN, *LHC Design Report*, Vol. 1, (2004) ISBN 92-9083-224-0

[4] J.B. Jeanneret, D. Leroy & L. Oberli, *Quench Levels and Transient Beam Losses in LHC Magnets*, LHC Project Report 44 (1996)

[5] H. Bichsel, D.E. Groom & S.R. Klein, *Passage of Particles Through Matter,* The European Physical Journal, Volume 15, No.1-4, 163, (2000)

[6] S.M. Seltzer & M.J. Berger,*Improved Procedure for Calculating the Collision Stopping Power of Elements and Compounds for Electrons and Positrons*, Int. J. Appl. Radiat. Isot. Vol 35, No.7, 665 (1984)

[7] D.H. Wilkinson, *Ionization Chambers and Counters,* (1950) The Syndics of the Cambridge University Press

[8] F. Sauli, *Principles of Operation of Multiwire Proportional and Drfit Chambers*, (1977) CERN 77-09

[9] C. Grupen,*Particle Detectors*, (1996) ISBN 0-521-55216-8

[10] D.Ritson, *Techniques of high-energy physics*, Interscience, New York, (1961) ISBN 0-521-55216-8

[11] E.A. Mason, *Estimated Ion Mobilities for some Air Constituents*, Planet. Space Sci. Vol. 18, 137 (1970) Pergamon Press

[12] W. Lindinger & D.L. Albritton, *Mobilities of various mass-identified positive ions in helium and argon*, Journal of Chem. Phys., Vol. 62, No. 9, (1975)

[13] T. Koizumi, N. Kobayashi & Yozaburo, *Mobilities of Li^+, NO^+, and O_2^+ in N_2 and CO_2 Gases*, J. Phys. Soc. Japan, Vol. 43, No. 4,1465 (1997)

[14] L.G.H. Huxley & R.W. Crompton, *The Diffusion and Drfit of Electrons in Gases*, (1974) ISBN 0-471-42590-7

[15] E.A. Mason & E.W. McDaniel, *Transport Properties of Ions in Gases*, (1988) ISBN 0-471-88385-9

[16] H.W. Ellis, E.A. Mason, R.Y. Pai, E.W. McDaniel & L.A. Viehland, *Transport Properties of Gaseous Ions over a wide Energy Range. Part I*, Atomic Data and Nuclear Data Tables 17, 177, (1976)

[17] H.W. Ellis, E.A. Mason, M.G. Thackston & E.W. McDaniel, *Transport Properties of Gaseous Ions over a wide Energy Range. Part III*, Atomic Data and Nuclear Data Tables 31, 113, (1984)

[18] E.A. Mason & L.A. Viehland, *Transport Properties of Gaseous Ions over a wide Energy Range. Part IV*, Atomic Data and Nuclear Data Tables 60, 37, (1995)

[19] J.W. Boag, *Space Charge Distortion of the Electric Field in a Plane Parallel Ionization Chamber*, Phys. Med. Biol. Vol. 8, No. 4, 461(1963)

[20] S.D. Senturia & B.D. Wedlock, *Electronic circuits and applications*, Wiley New York, (1975)

[21] C. Theis, S. Roesler & H. Vincke, CERN, *Comparison of the Simulation and Measurements of the Responce of Centronic High-Pressure Ionisation Chambers to the Mixed Radiation Field of the CERF facility*, (2004) CERN-SC-2004-24-RP-TN

[22] C. Theis, S. Roesler, M. Rettig & H. Vincke, CERN *Simulation and Experimental Verification of the Response Functions of Centronic High-Pressure Ionisation Chambers*, (2004) CERN-SC-2004-23-RP-TN

[23] R. Witkover & D. Gassner, Brookhaven National Laboratory, *Design of an Improved Ion Chamber for the SNS*,

[24] B. Dörschel, V. Schuricht & J. Steuer, *The Physics of Radiation Protection*, ISBN 1-870965-42-6

[25] M. Hodgson, *Zero Voltage, Time Dependant Signals of Ionisation Chambers*, CERN (2004)

[26] M. Hodgson, *Ionisation Chamber Beam Scan Simulations*, CERN (2004)

[27] B. Dehning & M. Hodgson, *Estimated Ionisation Chamber Doses for SPS Since, 1976 - 2003*, CERN (2004)

[28] S. Giani *et al.*, CERN, *Geant 4 - User's Guide*, `http://geant4.web.cern.ch/geant4/G4UsersDocuments/UsersGuides/ForApplicationDeveloper/html/`, last updated December 2004

[29] R. Veenhof, CERN, *Argon and Neon with varying CO_2 fraction*, `http://alice.web.cern.ch/Alice/AliceNew/`, last updated 30.06.99

[30] R. Veenhof, CERN, `http://rjd.home.cern.ch/rjd/`, last updated 22.11.04

[31] R. Veenhof, CERN, *Garfield - simulation of gaseous detectors*, `http://garfield.web.cern.ch/garfield`Last updated 13.03.2005

[32] R.K. Bock & A. Vasilescu, *The Particle Detector BriefBook*, `http://rkb.home.cern.ch/rkb/titleD.html`

[33] ChemGlobe, *Peirodic Table of Elements*, `http://www.vcs.ethz.ch/chemglobe/ptoe/index.html`

[34] National Institute of Standards and Technology, *Composition of Materials*, `http://physics.nist.gov/` , last updated 2000

[35] E.M. Gullikson, LBNL *X-ray Interactions with Matter*, `http://www.cxro.lbl.gov/optical_constants/` , last update 2004

[36] Private conversation with Dr. Bernd Dehning, CERN(2004)

[37] D.J. Griffiths, *Introduction to Electrodynamics*, 3^{rd} edition, ISBN 0-13-919960-8

[38] S.J. Doran, *Level 3: Relativity*, Lecture Notes, University of Surrey, UK, (2003-2004)